

CRANFIELD UNIVERSITY

Robert Scott

Elemental and Phase Composition of Breast Calcifications

Cranfield Defence and Security

PhD

Academic Year: 2016 - 2017

Supervisors: Professor Keith Rogers, Dr Catherine Kendall

Professor Nicholas Stone

April 2017



CRANFIELD UNIVERSITY

Cranfield Defence and Security

PhD

Academic Year 2016 - 2017

Robert Scott

Elemental and Phase Composition of Breast Calcifications

Supervisors: Professor Keith Rogers, Professor Nicholas Stone

Dr Catherine Kendall

May 2017

© Cranfield University 2017. All rights reserved. No part of this publication may be reproduced without the written permission of the copyright owner.

## ABSTRACT

Despite the importance of calcifications in early detection of breast cancer, and their proposed association with tumour growth, remarkably little detail is known about their chemical composition, or how this relates to pathology. One reason for this gap is the difficulty of systematically and precisely locating calcifications for analysis, particularly in sections taken from diagnostic archives. Two simple methods were developed which can achieve this in sections cut from wax embedded breast tissue. These are based on micro-CT and x-ray fluoroscopy mapping, and were used to locate calcifications for further study.

The elemental composition of calcifications in histological sections was measured using energy-dispersive x-ray spectroscopy in an environmental scanning electron microscope. Variations in Ca:P ratio could in principle be detected non-invasively by dual energy absorptiometry, as demonstrated in a proof of principle experiment. However, the Ca:P ratio was found to lie in a narrow range similar to bone, with no significant difference between benign and malignant. In contrast, a substantial and significant difference in Na:Ca ratio was found between benign and malignant specimens. This has potential for revealing malignant changes in the vicinity of a core needle biopsy.

The phase composition and crystallographic parameters within calcifications was measured using synchrotron x-ray diffraction. This is the first time crystallite size and lattice parameters have been measured in breast calcifications, and it was found that these both parallel closely the changes in these parameters with age observed in foetal bone. It was also discovered that these calcifications contain a small proportion of magnesium whitlockite, and that this proportion increases from benign, to carcinoma *in-situ*, to invasive cancer. When combined with other recent evidence on the effect of magnesium on hydroxyapatite precipitation, this suggests a mechanism explaining observations that carbonate levels within breast calcifications are lower in malignant specimens.

## **ACKNOWLEDGEMENTS**

I would like to thank my three supervisors, Keith Rogers, Nick Stone, and Catherine Kendall for their support and wise words of guidance. I would also like to thank Mark Anniss, Jo Motte, and Leanne Hughes of the Department of Pathology, Cheltenham General Hospital, for their assistance in identifying and preparing the tissue samples; Xianwei Liu and Christine Kimpton of Cranfield University for their technical assistance with the SEM-EDS; Tina Geraki of Diamond Light Source for all her help setting up and running the synchrotron experiments, including late evening troubleshooting of controller crashes. Finally I thank my wife Caroline for her unwavering support, from proof reading publications to morale boosting cups of tea during writing up, for her patience when I paid more attention to my computer than to her, and most of all for encouraging the idea of embarking on a PhD in the first place.

# TABLE OF CONTENTS

ABSTRACT.....	ii
ACKNOWLEDGEMENTS .....	iii
LIST OF FIGURES.....	vii
LIST OF TABLES.....	x
LIST OF ABBREVIATIONS.....	xi
1 Calcifications in Breast Cancer.....	1
1.1 Current role in diagnosis .....	1
1.2 Use as prognostic indicator.....	4
1.3 Calcification imaging.....	7
1.4 Deposition mechanism .....	8
1.5 Proposed role in tumour growth and metastasis .....	9
1.6 Composition.....	11
1.7 Potential new diagnostic methods.....	12
1.7.1 X-ray based.....	12
1.7.2 Vibrational spectroscopy .....	14
2 Locating Calcifications in Tissue Specimens .....	16
2.1 Aims .....	16
2.2 Introduction.....	16
2.2.1 Radiography.....	16
2.2.2 X-ray Fluorescence .....	17
2.2.3 Coordinate registration .....	17
2.3 Materials and Methods .....	18
2.3.1 Samples.....	18
2.3.2 CT scanning.....	19
2.3.3 X-ray fluorescence imaging.....	19
2.3.4 Visible imaging.....	19
2.4 Results .....	20
2.4.1 Qualitative results.....	20
2.4.2 Quantitative analysis .....	23
2.5 Discussion .....	24
2.6 Summary .....	26
3 Dual-Energy X-Ray Imaging.....	27
3.1 Aims .....	27
3.2 Introduction.....	27
3.2.1 Dual energy material decomposition .....	27
3.2.2 Dual energy mammography .....	28
3.2.3 Calcium/Phosphorus ratio .....	30
3.2.4 Polychromatic radiation .....	36
3.3 Proof of Principle Experiments.....	37
3.3.1 Introduction .....	37

3.3.2 Materials and Methods.....	37
3.3.3 Results.....	38
3.4 Summary.....	40
4 Elemental Analysis.....	44
4.1 Aims.....	44
4.2 Background.....	44
4.3 Materials and Methods.....	45
4.3.1 Archive blocks.....	45
4.3.2 Mounting.....	46
4.3.3 X-Ray microanalysis.....	48
4.3.4 Charging.....	48
4.3.5 Specimen thickness.....	49
4.3.6 Topography.....	51
4.4 Results.....	53
4.4.1 Calcification Morphology.....	53
4.4.2 Calcium Phosphorus Ratio.....	55
4.4.3 Magnesium Calcium Ratio.....	56
4.4.4 Sodium Calcium Ratio.....	57
4.5 Discussion.....	59
5 Crystallographic Parameters.....	62
5.1 Aims.....	62
5.2 Introduction.....	62
5.3 Materials and Methods.....	63
5.3.1 Archive blocks.....	63
5.3.2 Mounting.....	63
5.3.3 Beamline set-up.....	65
5.3.4 Analysis.....	66
5.4 Results.....	71
5.4.1 Phase composition.....	71
5.4.2 Hydroxyapatite analysis.....	74
5.4.3 Spatial variation.....	76
5.4.4 Correlation with elemental composition.....	77
5.5 Discussion.....	79
5.5.1 Major phases.....	79
5.5.2 Whitlockite.....	79
5.5.3 Precursor phases.....	81
5.5.4 Comparison with maturing bone.....	81
5.5.5 Ionic substitutions.....	83
5.5.6 Spatial variation.....	84
6 Conclusions and Future Work.....	85
6.1 Contributions to knowledge.....	85
6.2 Future work.....	87

REFERENCES .....	89
Appendix A Processed Data .....	A-1
A.1 XRD Summary aggregated by calcification.....	A-1
A.2 EDS summary aggregated by calcification .....	A-3
Appendix B Pathology summaries.....	B-1
Appendix C Hydroxyapatite X-ray diffraction lines .....	C-1
Appendix D XRD Fixture drawings .....	D-1
Appendix E ImageJ Programs.....	E-1
Appendix F Publications.....	F-1



## LIST OF FIGURES

Figure 2-1: Thresholded CT images and XRF overlay images of three typical FFPE core biopsy breast specimens. The registration holes are clearly visible on the CT slice images, but are less easy to locate on the XRF overlays.....	21
Figure 2-2: Standard H&E stained and unstained tissue sections illustrate the difficulty of identifying the location of calcifications without the aid of a CT image. ....	22
Figure 2-3 CT-derived coordinates of four calcifications overlaid on a white light image of an unstained section. ....	24
Figure 3-1 Mass attenuation coefficient of cortical bone and soft tissue vs. photon energy. ....	28
Figure 3-2 The attenuation ratio attributable to material components can be visualised directly from a log-log chart of mass attenuation coefficient vs. photon energy. ....	31
Figure 3-3 Gradient of log-MAC for calcium and phosphate with respect to log photon energy. ....	32
Figure 3-4 Total x-ray transmission and Weber contrast, as a function of photon energy, through 50mm of breast tissue and a 500 $\mu$ m thick calcification. ..	33
Figure 3-5 D-ratio of stoichiometric calcium phosphates, calcium deficient apatite, and carbonated hydroxyapatite. Abbreviations are given in Table 3-1.....	35
Figure 3-6 Image processing steps to derive attenuation ratio image from two transmittance images. ....	39
Figure 3-7 Dual energy imaging clearly distinguishes discs of hydroxyapatite (bottom row) from calcium hydrogen phosphate (top row). Labels refer to nominal thickness in mm. ....	39
Figure 3-8 Mean D-ratio as a function of material and disc thickness in mm. .	40
Figure 4-1 H&E stained images of typical calcifications: (a) Specimen X44 (B2), (b) Specimen X53 (B5a), (c) Specimen X46 (B5b). Histopathology summaries can be found in Appendix B. ....	47
Figure 4-2 WinCasino 2.48 was used to create a $\phi(\rho,z)$ curve for generation and emission of Ca $K\alpha$ x-rays vs. depth with 20keV electrons into a 5 $\mu$ m layer of cortical bone. It can be seen that there is negligible penetration of x-rays to the substrate. ....	50
Figure 4-3 Cross section view of absorbed energy density in a 5 $\mu$ m layer of cortical bone on an aluminium alloy substrate. ....	51

Figure 4-4 SEM image of a typical calcification overlaid with EDS elemental maps. The aluminium substrate can be seen through the cracks in the calcification resulting from sectioning. ....	54
Figure 4-5 SEM image of a highly fragmented calcification. Note the shadowing of the substrate in the Al image. ....	54
Figure 4-6 SEM image of a calcification with low phosphorus regions corresponding to a non-apatite phase. ....	55
Figure 4-7 A plot of median calcification Ca:P ratios vs. specimen diagnosis shows no significant variation of Ca:P ratio with specimen pathology. ....	56
Figure 4-8 A plot of median calcification Mg:Ca ratios vs. specimen diagnosis shows no significant variation of Mg:Ca ratio with specimen pathology. ...	57
Figure 4-9 The Na:Ca ratio of calcifications in specimens with a benign diagnosis is significantly lower than that in specimens categorised as malignant ( <i>In-situ</i> or <i>Invasive</i> ). ....	58
Figure 4-10 Scatter plot showing that low-P areas in specimen S66 also have a low Na:Ca ratio. ....	59
Figure 5-1 – Tissue section mounted on polyolefin film stretched across an aluminium alloy ring, and held in place with a Viton rubber O-ring. ....	64
Figure 5-2 Cake remapped diffraction image showing whitlockite spots. ....	67
Figure 5-3 Peak fitting using fixed component peak positions but unconstrained height and width gives a good fit to the major composite HA peak. ....	68
Figure 5-4 All-specimen average coherent domain thickness for each crystallographic reflection with Langford cylindrical model lines of best fit.	70
Figure 5-5 All-specimens sum diffractogram and digitally isolated large crystallite diffractogram vs. theoretical line positions and intensities. ....	72
Figure 5-6 Whitlockite weight percentage average per specimen, grouped by diagnosis. Malignant specimens contain significantly more whitlockite than those with a benign diagnosis. Individual specimen details are available in Appendix B. ....	73
Figure 5-7 The maximum intensity line shows no evidence of any of the four peaks corresponding to brushite or weddellite which lie between 29° and 30°. ....	74
Figure 5-8 Hydroxyapatite crystalline domain dimensions, averaged by specimen and categorised by diagnosis. Malignant specimens have significantly larger crystalline domain size in both axes than benign specimens. ....	75

- Figure 5-9 Hydroxyapatite lattice parameters, averaged by specimen and categorised by diagnosis. There is a significant negative correlation between 'a' and 'c' lattice parameters, and the 'c' lattice parameter is significantly smaller in benign than in malignant specimens. .... 76
- Figure 5-10 The spatial variation of (002) FWHM shows that the domain size is larger at the centre of the calcifications than at the surface. .... 77
- Figure 5-11 Mean values of calcification c/a lattice parameter ratio (unit cell shape) and crystallite domain size along the 'c' axis ( $\tau_c$ ) for benign and invasive specimens (green and red lines respectively), overlaid on corresponding measurements for foetal bone as a function of the average bone age. Foetal bone measurements reprinted from Dalconi *et al*<sup>192</sup>, with permission from Elsevier. .... 82

## **LIST OF TABLES**

Table 3-1 Abbreviations used in Figure 3-5.....	36
Table 5-1 Correlation of elemental ratios measured in this study, with X-ray diffraction measurements made on the same 39 calcifications. ....	78

## LIST OF ABBREVIATIONS

BI-RADS	Breast Imaging Reporting and Data System
BMP-2	Bone Morphogenic Protein 2
BSP	Bone Sialoprotein
CEDM	Contrast Enhanced Digital Mammography
CESM	Contrast Enhanced Spectral Mammography
CHAP	Carbonated Hydroxyapatite
CI	Confidence Interval
CT	Computed Tomography
DCIS	Ductal Carcinoma <i>In-Situ</i>
DCPD	Dicalcium Phosphate Dihydrate
DPA	Dual Photon Absorptiometry
EDS	Energy Dispersive Spectroscopy
ESEM	Environmental Scanning Electron Microscope
FFPE	Formalin Fixed Paraffin Embedded
FTIR	Fourier Transform InfraRed
FWHM	Full Width Half Maximum
H&E	Haematoxylin and Eosin
HA	Hydroxyapatite
HER2	Human Epidermal Growth Factor Receptor 2
IHC	ImmunoHistoChemical
IR	InfraRed

LCIS	Lobular Carcinoma <i>In-Situ</i>
MAC	Mass Attenuation Coefficient
MCPM	Monocalcium Phosphate Monohydrate
NHSBSP	NHS Breast Screening Programme
NIST	National Institute of Standards & Technology
OCP	Octacalcium Phosphate
PPV	Positive Predictive Value
PSF	Point Spread Function
RCRBG	Royal College of Radiologists Breast Group
SAXS	Small Angle X-ray Scattering
SEM	Scanning Electron Microscope
SORS	Spatially Offset Raman Spectroscopy
SPA	Single Photon Absorptiometry
TCP	Tricalcium Phosphate
TEM	Transmission Electron Microscope
TTCP	Tetracalcium Phosphate
WDS	Wavelength Dispersive Spectroscopy
XRD	X-Ray Diffraction
XRF	X-Ray Fluorescence

# 1 Calcifications in Breast Cancer

## 1.1 Current role in diagnosis

Calcifications\* have an important role in the early detection of breast cancer. It is widely accepted that early detection is important; in the words of the World Health Organisation “Early detection of cancer greatly increases the chances for successful treatment”<sup>1</sup>. A suspicious pattern of radiographically visible calcifications is frequently the earliest diagnostic sign of breast cancer. In a recent publication from a large scale study of ductal carcinoma *in-situ* (DCIS) 90.6% (1967 / 2169) of patients with a diagnosis of DCIS had screen detected calcifications<sup>2</sup>. In another study, 76% of DCIS and 35% of small invasive tumours (< 10 mm) were detected on the basis of calcifications alone<sup>3</sup>. However, the presence of calcifications is also common in normal breast tissue, particularly in older women<sup>4</sup>. The presence of calcifications *per-se* does not necessarily indicate the presence of breast cancer or precancerous changes in breast tissue. Nonetheless, the radiographic appearance of calcifications can provide clues as to whether they are benign or malignant in origin. The radiographic features of calcifications that are most diagnostically useful have evolved over decades through many radiology-pathology correlation studies. The characteristics which best distinguish suspicious from benign calcifications are based on observation of their radiographic size, shape, and distribution. There are well developed rules for incorporation of these observations within a standardised reporting and risk scoring system, such as the American College of Radiology Breast Imaging Reporting and Data System (BI-RADS)<sup>5</sup>, which is widely used in North America and much of Europe, or the Royal College of Radiologists Breast Group (RCRBG) classification<sup>6</sup>, which is widely used in the UK. The RCRBG system is used to classify mammography and ultrasound findings on a simple 1 - 5 scoring system for normal, benign, uncertain, suspicious, and malignant appearance. The BI-RADS system employs a similar

---

\* The term microcalcifications is frequently used to describe calcifications of less than about 0.5 – 1mm in diameter<sup>8,209</sup>, since this is the size range of most interest and concern in breast cancer. The umbrella term “calcifications” includes microcalcifications as well as calcifications of a larger size, and is generally used in this work.

1 – 5 scale from normal to malignant for reporting ultrasound and mammography results, but also includes categories of 0 and 6 for incomplete assessment and biopsy-proven malignancy respectively. In addition, BI-RADS 4 is often subcategorised into classes 4a, 4b, and 4c for low, intermediate, and moderate suspicion of malignancy<sup>7</sup>.

The BI-RADS standardised report for mammography includes assessment of breast composition, description of any masses, asymmetry, or architectural distortion, and classification of the morphology and distribution of calcifications. Morphological descriptions of calcifications are classified as “Typically Benign” or “Suspicious”, are described in detail, with examples, in the BI-RADS Atlas<sup>5</sup>. As well as morphology, the distribution of calcifications is an important factor in risk scoring. Diffuse distribution is indicative of low risk, and distributions categorised as regional, grouped (cluster), linear, and segmental represent increasing levels of risk. Another important factor in risk scoring is the stability of calcifications; a pattern of calcifications that stays stable over the course of three screening examinations can be considered to be less suspect<sup>8</sup>.

Despite the refinement of mammographic risk-scoring rules over decades of experience and hundreds of millions of mammograms\*, the value of mammography as a routine screening tool remains highly controversial, both in the medical literature and in the popular press. There are three interconnected reasons for this.

First, mammography screening has a low positive predictive value (PPV). The most recent published results from the NHS England screening programme show that only 21% women referred for further assessment following screening subsequently receive a diagnosis of cancer<sup>9</sup>. Quite apart from the cost, false-positive screening mammograms can lead to distress lasting for years, particularly for biopsy assessment<sup>10</sup>.

---

\* The screening mammography coverage for all OECD countries in women age 50 – 69 was 58.8% in 2013. With a corresponding subject population of 150 million and triennial screening, that equates to approximately 30 million mammograms per year.



Second, a significant proportion of patients participating in mammography screening are overdiagnosed, i.e. cancers are detected which would never have become symptomatic in the patients' lifetime. Estimates of overdiagnosis are notoriously difficult to make since patients who have received a diagnosis of breast cancer are generally treated. The only way to be certain that an individual has been overdiagnosed is if she receives a diagnosis of cancer, remains untreated, never develops symptoms, and dies of something else. Indirect evidence from trials, observational studies, and statistical modelling have yielded widely varying estimates varying from zero to 54%, though an overall figure region of 11% to 22% has been suggested<sup>11</sup>. It is generally accepted that overdiagnosis is a significant problem which needs to be addressed<sup>12</sup>, particularly with DCIS<sup>13,14</sup>.

Third, breast cancer death rates remain stubbornly high, even in populations with a high uptake of screening. Women who consistently attend screening still die of breast cancer. An independent evidence review commissioned by Cancer Research UK and the Department of Health (England) and published in 2002 concluded that the most reasonable estimate for reduction in breast cancer mortality as a result of screening is approximately 20%, with a 95% confidence interval of 11% to 27%<sup>15</sup>. The US Agency for Healthcare Research and Quality published a meta-analysis of evidence in 2016 and concluded: "Breast cancer mortality is reduced with mammography screening, although estimates are of borderline statistical significance, the magnitudes of effect are small for younger ages, and results vary depending on how cases were accrued in trials."<sup>11</sup>. However, it has been suggested that much of the positive evidence is based on old studies conducted at a time when treatment was less effective. The influential Cochrane group concluded that "More recent studies suggest that mammography screening may no longer be effective in reducing the risk of dying from breast cancer"<sup>16</sup>. Studies continue to be published casting doubt on the efficacy of screening for reducing mortality. For example, a recent study charting breast cancer mortality against screening uptake by county in the US found strong evidence that screening has no effect on breast cancer specific mortality, with a 10% increase in screening uptake giving a mortality risk ratio of

1.01 (95% CI, 0.96-1.06)<sup>17</sup>. A large randomised study in Canada with 25 years follow up similarly found no breast cancer mortality benefit from screening, with a hazard ratio for screened/unscreened of 1.05 (95% CI 0.85 to 1.30)<sup>18</sup>.

Combining uncertain estimates of overdiagnosis and mortality reduction inevitably yields widely varying results on the ratio of unnecessary interventions to lives saved. A typical analysis in a patient summary for the Journal of the American Medical Association estimated that for 50 year old women screened for 10 years, for every life saved by screening, 6 women receive unnecessary treatment (e.g. mastectomy, radiotherapy, chemotherapy), 9 have an unnecessary biopsy, and 613 receive at least one false-positive mammogram; in addition, 6 will die of breast cancer anyway, despite screening<sup>19</sup>. It is clear that greatly improved diagnostic tests are needed, not only to reduce unnecessary biopsies (resulting from poor PPV) and unnecessary mastectomies (resulting from overdiagnosis), but also to detect aggressive breast cancers at an early enough stage to prevent recurrence, metastasis, and death.

## **1.2 Use as prognostic indicator**

Once a diagnosis has been made, gauging the risk of progression and subsequent death is important in deciding appropriate treatment for an individual patient. This is particularly important in avoiding overtreatment of early stage cancer<sup>20</sup>. Appropriate adjuvant systemic therapy can eradicate silent micrometastases, but does carry substantial associated risks; it is therefore essential to be able to estimate metastatic risk before embarking on a course of potentially harmful treatment<sup>21</sup>. Prognostic factors form the basis of that assessment, and predictive factors indicate which adjuvant treatments are most likely to be effective in that individual case. Traditional prognostic factors are based on tumour stage and grade, and are frequently combined into a numerical score such as the Nottingham Prognostic Index<sup>22</sup> for invasive breast cancer. In addition, immunohistochemical (IHC) markers of oestrogen and progesterone receptor expression, HER2 status, and Ki67 proliferation index act both as prognostic indicators and predictors of particular adjuvant treatment

effectiveness. In addition to a single index, prognostic factors have been modelled using cancer registry data and built into publicly available prognosis calculators such as NHS PREDICT<sup>23,24</sup>. An important class of new predictive indicators is based on gene expression profiling. The seminal paper on the use of this technique to create “molecular portraits” of breast cancer was published in 2000 in *Nature*<sup>25</sup>. It has since been widely accepted that breast cancer develops in distinct subtypes with a similar pattern of gene expression in each group. These subtypes appear to be intrinsic to the tumour; not only does the subtype of the primary stay within the same grouping over time, but lymph node metastases exhibit the same gene expression pattern as the corresponding primary tumours. These different groups vary dramatically in prognosis. A wide range of multi-gene expression signatures have been commercialised as prognostic indicators, based on expression patterns of a selected panel of genes<sup>26</sup>.

Although extensively used, traditional prognostic indicators have their limitations. In particular, histological grade has been widely criticised for lack of reproducibility<sup>27</sup>. A large scale analysis of interobserver agreement in breast pathology reporting comes from an analysis of data gathered by the UK NHSBSP External Quality Assessment (EQA) scheme<sup>28</sup>. Agreement on histological grade of invasive carcinoma was only moderate ( $\kappa = 0.47$ ), and agreement on nuclear grade in DCIS was even lower ( $\kappa = 0.36$ ); this is particularly problematic, since DCIS is where the need is greatest for accurate prognostic and predictive information<sup>29</sup>. A review of 12 other studies from around the world on inter-observer and intra-observer agreement of breast cancer histological grade gave broadly similar results<sup>27</sup>. There is a clear clinical need for more reliable prognostic indicators. Molecular subtyping was initially heralded as a new dawn for assessing breast cancer prognosis<sup>30</sup>, and subsequently attracted a great deal of research. Although this has undoubtedly improved our understanding of breast cancer biology, agreement on risk categories between different commercially available gene signatures is only moderate<sup>31</sup>, and these have so far made limited headway in routine clinical practice<sup>26,32</sup>.

Calcifications have a role to play not only as a diagnostic sign, but as a prognostic indicator. There are numerous studies showing that calcifications are associated with other prognostic indicators<sup>33</sup>. However, there is evidence that calcification morphology has prognostic value, independent of histopathology classification. In a long term outcome study, Tabár *et al* found that patients with “casting” type calcifications (“fine linear / branching” in current BI-RADS terminology) have a substantially poorer long term survival compared to patients with either no calcifications or calcifications not classified as casting<sup>34</sup>. Moreover, the prognostic value was greatest in the smallest tumours (< 5 mm), where traditional prognostic factors perform poorly. This observation proved somewhat controversial at the time, with a surgeon involved with the development of the Nottingham Prognostic Index responding that “Calcification as a method of prognosis is not as accurate as other methods and has no practical clinical use”<sup>35</sup>. A further five studies have corroborated the poorer outcome associated with casting calcifications<sup>36–40</sup>, though two did not find a correlation<sup>41,42</sup>. A recent analysis of long term survival in younger women (mean age of 44.8 years at diagnosis) showed that radiological comedo calcification maintained independent prognostic significance in a multivariate analysis (in stepwise elimination of non-significant variables), whereas histological grade did not<sup>39</sup>. One possible factor is that these type of calcifications appear to be associated with multifocal, diffuse growth, and hence are difficult to excise completely, resulting in increased incidence of local recurrence<sup>43–45</sup>.

Given the lack of concordance within both traditional prognostic indicators and gene expression signatures, there is clear clinical need for better prognostic information to aid treatment decision making. This is particularly true for the increasing number of early stage cancers detected by mammography. Calcification morphology has shown to have some value. The potential role of calcification chemistry as a prognostic indicator remains unexplored.

### 1.3 Calcification imaging

Since the early days of mammography there have been advances in both x-ray source and detectors which have improved calcification visualisation.

The base technology for x-ray generation, consisting of a rotating anode x-ray tube with a molybdenum or rhodium-surface anode, has remained essentially unchanged since the earliest dedicated mammography units produced in 1966<sup>46</sup>. Improvements have been evolutionary rather than revolutionary. Tube design advances have allowed modest increases in power density without damaging the anode. This is desirable for two reasons. The spot size can be made smaller, improving the resolution, which is important for microcalcifications, or the power can be increased, shortening exposure and thus reducing the potential for motion blurring, or a combination of both. There is little prospect of significant further improvement in power density with conventional x-ray tube technology due to intrinsic thermal limitations<sup>47</sup>. One recent breakthrough technology for x-ray generation involves the use of a liquid metal jet anode. This could potentially increase power density by two orders of magnitude, and has been proposed for use in mammography<sup>47</sup>. Liquid metal-jet tubes have been supplied commercially since 2010 and a range of sources developed. These have been used for applications such as real-time SAXS<sup>48</sup>, and high resolution CT imaging of small animals using both absorption and phase contrast<sup>49,50</sup>. This technology has not yet been adopted for clinical use.

In contrast to the incremental changes in x-ray sources, improvements in mammography x-ray detection and imaging have been punctuated by major step changes in technology. In the early days of mammography, x-ray film was used directly to create an image. This required a long exposure, which not only was susceptible to motion blurring, but resulted in a high radiation dose. The introduction of rare-earth intensifying screens in the early 1970s greatly reduced the time and dose required to create an image. More recently, high resolution amorphous semiconductor digital detector panels have almost entirely superseded film. These provide a further reduction in x-ray dose, as well as offering improved dynamic range, ease of postprocessing for image

enhancement, easier storage and retrieval, and facilitating computer aided detection. Most recently, photon counting detectors are starting to be used clinically, most notably in the Philips Microdose system, offering further reduction in x-ray dose and enabling single-shot spectral mammography.

Improvements in mammography equipment technology, particularly the transition from screen-film to digital mammography, have undoubtedly improved the detectability of calcifications<sup>51</sup>, particularly those presenting as small clusters<sup>52</sup>. Several studies have suggested that the increase in detection does come at the expense of an increased number of false positives<sup>53,54</sup>, particularly during the transition period from screen-film to digital<sup>51,55</sup>. However, other studies have found that the increased number of referrals for biopsy is not accompanied by a decrease in the percentage that are malignant<sup>3,56,57</sup>, and that the proportion that are of low grade has also not increased<sup>56</sup>. Irrespective of the effect on predictive accuracy, it is generally agreed that digital mammography does overall result in increased early detection of potentially life threatening tumours.

Further improvements in x-ray imaging technology undoubtedly have a contribution to make towards accurate early detection of breast cancer. In part, this may simply be increased clarity and spatial resolution of conventional x-ray absorption images. However, new technology may enable more information to be extracted from mammographic images, using techniques such as spectral imaging and analysis of coherent scatter. In particular, the ability to distinguish between calcifications based on chemical composition rather than just size and morphology may add a new dimension to the information being assessed, resulting in both fewer false positives and an increased mortality reduction through earlier detection.

#### **1.4 Deposition mechanism**

Calcium deposits in soft tissue can occur in damaged or diseased tissue, and frequently occur in necrotic tissue<sup>58</sup>. In breast tissue, fat necrosis resulting from external trauma, or from previous biopsy or surgery, frequently leads to calcification formation<sup>59</sup>. In breast cancer, calcifications occur in conjunction

with comedo necrosis in DCIS, in which lack of vascular supply to proliferating tumour cells within a duct leads to cell death, particularly in the centre of the lumen<sup>60</sup>. Calcifications can also form following neoadjuvant therapy to shrink the tumour prior to surgery; It is thought that these occur as a result of tumour cell necrosis<sup>61</sup>. Although necrosis undoubtedly plays a role in the formation of some calcifications, there is increasing evidence that calcification formation in a breast tumour can be an active cell-mediated process, involving the expression by cancer cells of numerous proteins involved in bone formation and growth. For instance, Bone Morphogenic Protein 2 (BMP-2) promotes bone formation and plays an important role in osteoblast differentiation. It has also been found to enhance calcification in-vitro in a malignant mammary cell line<sup>62</sup>. BMP-2 is known to be expressed by breast cancer cells, and one study showed reduced levels in cancers without calcifications and increased levels where calcifications were present<sup>63</sup>. As another example, Bone Sialoprotein (BSP) is an abundant bone matrix protein, which is particularly strongly expressed by osteoblasts at the site of new bone formation<sup>64</sup>. Elevated expression of BSP is also found in malignant breast tissue, particularly where calcifications are present<sup>65</sup>. Elevated levels are also associated with increased risk of bone metastasis<sup>66</sup>. At least another eleven bone matrix proteins have been identified which may have an effect on calcification formation in the breast, though very limited research has been conducted on many of these<sup>64</sup>. Given the diversity in gene expression patterns forming the basis of tumour molecular subtypes, and the fact that some of these expressed genes are involved in bone metabolism, it is reasonable to expect tumour heterogeneity to be reflected by some variation in the nature of the calcifications formed in different types of breast tumour.

## **1.5 Proposed role in tumour growth and metastasis**

As well as being the product of cell mediated processes, there is increasing evidence that calcifications in breast cancer may play an active role in mitogenesis, upregulation of gene expression, and enhanced migration of tumour cells<sup>67-69</sup>. In particular, calcifications associated with breast cancer consist predominantly of hydroxyapatite, and there is evidence that nanoscale

properties of hydroxyapatite may play an important role in regulating breast cancer cell behaviour<sup>70</sup>. Understanding the nature of calcifications is important in developing a complete picture of the factors affecting tumour development and progression.

In addition, the presence and nature of calcifications may be relevant to metastasis. It was noted in the 19<sup>th</sup> century that cancer metastases are not randomly distributed through the body, but targeted at particular tissue types. Bone is the most common, and often the earliest, metastasis site for breast cancer. The hypothesis popularised by Paget in 1889 (though suggested by others earlier) suggests that particular tissues form congenial “soil” in which circulating tumour cell “seeds” can lodge and grow<sup>71</sup>. It is now widely recognised that circulating tumour cells cannot readily colonise a foreign microenvironment, and that “The differences in stromal components, tissue organization, matrix composition, and cytokine environment all impose immense threats on the just arrived cancer cells.”<sup>72</sup>. The term “osteomimicry” has been coined to describe the way in which tumour cells can enhance their ability to survive and multiply in bone tissue by acquiring a bone-cell-like phenotype<sup>62,73,74</sup>. In particular, prostate and breast cancer cells can adopt a resemblance to osteoblasts by expressing bone matrix proteins. As previously noted, these proteins can induce mineralisation of breast tissue. Breast calcifications may therefore be, at least in part, the product of tumour cells pre-primed to survive in the bone microenvironment. It used to be thought that metastatic spread was a late event following development and growth of a primary tumour. However, it is increasingly evident that systemic spread can occur as an early step in breast cancer<sup>75</sup>. This might in part explain why, despite the early detection and treatment of tumours as a result of screening, there has been a very limited reduction in breast cancer mortality. Early recognition of calcifications which are the products of osteoblast-like metastasis-ready tumour cells may help improve the mortality benefit of screening.



## 1.6 Composition

Most publications referring to the composition of breast calcifications regurgitate the assertion that calcifications can be categorised as two types: Type 1, composed of calcium oxalate in the crystalline form of weddellite, and Type 2, composed of calcium phosphate in the crystalline form of apatite. Estimates of the comparative frequency in breast tissue vary widely. The proportion of biopsy samples with at least some Type 1 calcifications has been variously reported as 0.4%<sup>76</sup>, 7.3%<sup>77</sup>, 12%<sup>78</sup>, 13%<sup>79</sup>, 17%<sup>80</sup>, 25%<sup>81</sup>, and 29%<sup>63</sup>. In large part the wide variation is likely to be due to patient selection for biopsy, and specimen selection within those biopsies. In addition, it is known that some calcifications are lost on sectioning<sup>82</sup>. Type 1 calcifications are typically larger and more crystalline than Type 2<sup>83</sup>, hence may be more prone to loss from histological sections.

It is also frequently repeated that Type 1 calcifications are typically associated with benign lesions whereas Type 2 are sometimes associated with cancer. Type 1 calcifications appear to be the result of benign secretory processes, particularly related to benign apocrine metaplasia<sup>79</sup> or lobular carcinoma *in-situ* (LCIS)<sup>84</sup>. However, this does not preclude Type 1 calcifications from being coincidentally present as bystanders within breast tumours, as has been observed clinically<sup>85,86</sup>. An interesting new perspective comes from a recent study showing that the total oxalate content is apparently almost 10 times higher in human breast tumour tissue than normal breast tissue, and that calcium oxalate microcrystals can generate tumours when injected into the mammary tissue of mice<sup>87</sup>. These data appear to conflict with the observation that calcium oxalate calcifications are more common in benign than malignant breast lesions, but may indicate that calcium oxalate calcifications are not as benign as was previously thought.

The elemental composition of breast calcifications has been measured using SEM/EDS, mostly in the 1970s and 1980s. These studies were all qualitative, simply identifying the elements found. In most cases only calcium and phosphorus were reported<sup>88-91</sup>, though small quantities of S, Si, Na, Mg, Cl, and

K have also reported<sup>84,92</sup>. One study reported particles containing a rather implausible array of elements including Cr, Pb, Ag, Au, and Mo<sup>93</sup>, and another reported a calcification containing a substantial proportion of Sn<sup>94</sup>. These are very likely to be misidentifications, which can easily happen with automated peak identification in EDS software, particularly for minor elements<sup>95</sup>. To date there has only been one semi-quantitative study of the composition of breast calcifications. The Ca:P ratio was measured in three benign and two malignant Type 1 calcifications<sup>96</sup>, but with no significant difference with pathology. Apart from that, quantitative elemental composition of the most cancer-relevant Type 2 calcifications remains entirely unexplored.

Fourier Transform InfraRed (FTIR) spectroscopy and Raman spectroscopy have been used to probe the relationships between calcification chemistry and pathology. This complements elemental analysis, since vibrational spectroscopy gives useful information on the nature, concentration, and environment of the anions (e.g. phosphate, carbonate, hydroxide), but gives almost no information on the cations present (principally calcium). Possible uses of vibrational spectroscopy of calcifications as an aid to diagnosis are outlined in section 1.7.2.

Given the great diversity in calcification morphology, it would be surprising if all calcifications were of uniform chemical composition. In addition, a wide range of chemical changes occur in tumour tissue, hence it is reasonable to expect that calcification chemistry may also vary with pathology.

## **1.7 Potential new diagnostic methods**

Suggested new diagnostic methods based on calcification composition can be divided into two categories: x-ray methods, and vibrational spectroscopy.

### **1.7.1 X-ray based**

Conventional x-ray diagnostic methods rely on simple absorption imaging. Absorption is only one of many ways in which x-rays interact with matter; there is potential for other interaction mechanisms to be exploited for improved breast cancer detection. One category that has been the subject of considerable

research over the last two decades comes under the umbrella term “phase contrast imaging”. These techniques make use of phase shifts resulting from differences in the refractive index of different materials. At clinically relevant x-ray energies, phase contrast can be much larger than absorption contrast<sup>97</sup>. A wide range of x-ray phase contrast techniques have been developed, with an even wider range of names. The main focus of research into phase contrast mammography has been improvement in visualisation of subtle soft tissue distortions and masses. One of the most promising techniques for practical clinical application is based on an adaptation of a Talbot-Lau grating interferometer<sup>98</sup>. The key adaptation allowing this to be used with a conventional x-ray tube is the interposition of a third grating in front of the source. This effectively creates an array of individually coherent sources. A spin off from this approach is that a dark field image can be simultaneously generated, based on the strong small-angle scattering produced by microscopic density fluctuations<sup>99</sup>. This dark field image has considerable potential for imaging calcifications. In one study, a dark field image of an excised specimen clearly showed a tumour that was invisible with mammography or specimen radiography, but was found to contain a cluster of very small calcifications of 1 - 40µm in size<sup>100</sup>. Simulations demonstrated that these calcifications could produce the observed dark field image. Other studies using this type of dark field imaging on excised tissue have successfully differentiated between Type 1 and Type 2 calcifications<sup>101</sup> and between Type 2 calcifications of varying morphologies / microtexture<sup>102</sup>. Micro-CT measurements have suggested that there may be a difference in internal structure between benign and malignant calcifications<sup>103</sup>. One current obstacle to the implementation of this technique for mammography is the high tissue absorbed dose in the experimental configurations used to date. However, dose was not a consideration in the proof of concept experiments, and it has been suggested that optimisation could reduce the dose to within acceptable limits<sup>102</sup>. Another challenge is that the phase grating and the absorption grating need to be very precisely spaced and aligned. An intriguing low-tech approach has been proposed which does not require gratings, but makes use of “the remarkable properties of speckles”

generated by scanning a sheet of abrasive paper between source and object<sup>104</sup>. As with the Talbot-Lau approach, this can also simultaneously create absorption, phase contrast, and dark field images using a microfocus x-ray tube source.

Another proposed technique for non-invasive differentiation of Type 1 and Type 2 calcifications is also based on scatter, but takes a very different approach. This involves energy dispersive x-ray diffraction, using a polychromatic pencil beam source and a photon counting detector at a fixed angle. The sample was rotated in the beam and a CT slice reconstructed. This successfully differentiated hydroxyapatite from calcium oxalate in a phantom study<sup>105</sup>. There are practical problems involved in translating a method based on a pencil beam into clinical use, though these may not be insuperable.

Another potential method for distinguishing between calcifications of differing composition is dual energy absorptiometry. This has been suggested as a method for differentiating between Type 1 and Type 2 calcifications<sup>106,107</sup>, and is extensively dealt with in Chapter 3.

Methods for extending x-ray screening beyond simple absorption imaging appear to have potential for widening the range of information available to a radiologist. In particular, information on composition, crystallography, and microtexture of calcifications could be diagnostically useful.

### **1.7.2 Vibrational spectroscopy**

Vibrational spectroscopy has been investigated as a method to probe the chemistry of calcifications and thus add a new dimension to the characteristics used in diagnosis. The level of carbonate substitution in hydroxyapatite has been shown to be significantly different between benign and malignant calcifications<sup>108</sup>. The carbonate level decreases sequentially from benign to ductal carcinoma *in-situ*, to invasive cancer, and in the carcinoma specimens, carbonate substitution is negatively correlated with histological grade<sup>109</sup>. Raman spectroscopy could in principle be used non-invasively to measure these variations in chemistry. Conventional backscattering Raman spectroscopy is

too surface sensitive to interrogate the composition of calcifications buried within breast tissue. Three approaches have been attempted to overcome this. Firstly, temporal gating of the Raman signal has been successfully used to probe the chemical composition of calcified materials buried up to 1mm in tissue.<sup>110</sup> However, this depth penetration is insufficient for transcutaneous probing in the breast, and the instrumentation required is complex and expensive. In addition, there are some safety concerns over the use of short, high power laser pulses. Interest has shifted therefore to spatially offset Raman spectroscopy (SORS), in which depth discrimination is achieved by laterally offsetting the laser source and the signal detector. This has been shown to be capable of measuring the level of carbonate substitution in hydroxyapatite buried in up to 8.7 mm of tissue<sup>111</sup>. In mammography, the average compressed breast thickness is in the region of 60 mm,<sup>112</sup> though it should be noted that a small probe applied to the skin could attain a greater local compression. Another approach that eliminates depth sensitivity is transmission Raman, since the overall tissue propagation distance of probe signal plus Raman signal is equal to the total tissue thickness, irrespective of the depth at which the Raman interaction occurs. This has been shown to be capable of discriminating between hydroxyapatite and calcium oxalate monohydrate embedded within a total tissue thickness of up to 27mm<sup>113</sup>. This is verging on a clinically relevant thickness range. Raman spectroscopy has also been proposed as a method for improving the targeting on microcalcifications during needle biopsy. Real-time feedback could help to ensure that tissue containing radiographically suspicious calcifications is accurately targeted, and would reduce the chance of false negative samples<sup>114</sup>.

For any of these potential adjunct methods to be clinically useful, it is necessary to determine and explain the relationships between calcification physico-chemical properties and the increasingly multi-dimensional ways in which breast cancer pathology is classified.

## **2 Locating Calcifications in Tissue Specimens**

### **2.1 Aims**

A significant obstacle to the in-vitro analysis of breast calcifications is the lack of a simple method for systematically and precisely locating calcifications within a specimen. It is often difficult to identify a calcification definitively from its visual appearance in the absence of staining, particularly from a macroscopic view. The first stage of this research was therefore to establish such a method. This chapter is largely based on a previous publication<sup>115</sup>.

### **2.2 Introduction**

#### **2.2.1 Radiography**

The most direct method for locating calcifications within a histological section is to take an X-ray image. Calcifications contained within a thin histological section would be difficult or impossible to locate in this way when mounted on a standard microscope slide or on a typical substrate used for infrared (IR) spectroscopy, such as a calcium fluoride or barium fluoride window. In principle, it is possible to take an X-ray image of an adjacent histological section mounted on a thin radiolucent substrate such as a polymer film. In order to obtain sufficient contrast in a typical histological section of 3 to 8  $\mu\text{m}$  thickness, it would be necessary to use soft X-rays for imaging, ideally just above the calcium k-edge at 4.0 keV. Generation, transmission, and detection of such soft X-rays is not straightforward in practice. In addition, some fragmentation and loss of calcifications can occur on sectioning,<sup>82</sup> which means that some calcifications may be present in the spectroscopic section, but not in the reference radiographic section, or vice versa.

Since taking X-ray images of the thin tissue section itself presents some difficulty, another option is to radiograph the whole specimen from which the section is to be cut. This is a useful method for identifying which specimens contain calcifications, prior to sectioning. Radiography of biopsy specimens is routine in clinical practice. However, a single radiograph cannot be relied upon to locate the positions of calcifications in cut sections, since it gives no

information on the depth of these within the specimen. Additional radiographic views can help, though overlaps can make correlation of views difficult. A logical extension from taking multiple views is to conduct a CT scan, which can give a complete 3D view of the positions of calcifications in the specimen. The reconstructed volume can be used to determine the expected position of calcifications in the cut sections. This was therefore chosen as one of the methods to explore.

### **2.2.2 X-ray Fluorescence**

An alternative approach is to create a spectroscopic map of entire sections. With many spectroscopic techniques, particularly infrared, mapping multiple samples at sufficient resolution to detect calcifications can be very time consuming. A more suitable technique is X-ray fluorescence (XRF), which can relatively simply create a calcium map. As with X-ray absorption imaging of thin sections, this cannot be conducted on cut sections mounted on a typical substrate used for IR spectroscopy. Calcium fluoride is obviously unsuitable as a substrate for calcium imaging, and barium fluoride gives an excessive background signal which makes detection of the calcium signal difficult. As with CT, a simpler method is to create a map of the block face from which sections are cut. XRF images were taken, not only to investigate this as an alternative method, but as corroboration of the presence and position of the CT- detected calcifications.

### **2.2.3 Coordinate registration**

XRF and CT can be used qualitatively to relate calcification position to tissue features. However, in order to relate the positions quantitatively to coordinates within a section, it is necessary to use fiducial markers. Various markers for aligning histological sections in 3 D reconstructions have been proposed since the early 20<sup>th</sup> century. One of simplest methods consists of small parallel holes drilled through the tissue at right angles to the surface<sup>116</sup>. Various improvements have been suggested such as use of a laser to drill the holes<sup>117</sup> or the use of markers made from such exotic materials as cactus spines<sup>118</sup> and cuttlefish ink<sup>119</sup>. In contrast to most studies on such marker systems, the aim in this case

is not to align serial sections, but to register the positions of features in a histological section to an image slice taken through a CT volume or a block face XRF image. Nonetheless, the general requirements identified in earlier work still hold; the markers must be easy to cut, adhere to the slide, and be visible in the required imaging mode.

The situation is simpler with many analyses of calcifications within formalin fixed paraffin embedded (FFPE) breast tissue, since cut sections are frequently not de-waxed. The reason is that calcifications are held in place on the substrate by the wax, and de waxing can result in their loss. In addition, acquisition of data from tissue embedded in paraffin can reduce the incidence of dispersive artefacts<sup>120</sup>. That means that simple holes in the wax surrounding the tissue can be used as markers, without disturbance to the tissue or the need to introduce foreign materials into the block. That is the approach taken in this study, though other marker systems proposed in the literature could readily be substituted.

## **2.3 Materials and Methods**

### **2.3.1 Samples**

Formalin Fixed Paraffin Embedded (FFPE) core biopsy breast specimens were selected from the Gloucestershire Hospitals NHS Foundation Trust diagnostic archive, based on the presence of calcifications in the histopathology report. These were screened by mounting the blocks in a Nikon Metrology XT H225 CT system and imaging at 20 kV both perpendicular and parallel to the face of the block. Following screening, 12 blocks were selected with significant levels of calcification at or near the cut surface.

A minimum of three marker holes of  $\text{Ø}0.4$  mm were drilled in the selected blocks in a pattern surrounding the tissue. Care was taken to ensure that the hole patterns did not have line or rotational symmetry, to ensure that it was possible to determine unambiguously the orientation of cut sections, and which way up they had been mounted on the slide or substrate.

Two sequential microtome slices of 3  $\mu\text{m}$  were cut from each block and mounted on  $\text{Ø}30$  mm x 1 mm barium fluoride discs (Crystran Ltd., Poole) and



standard microscope slides respectively. The latter underwent standard haematoxylin and eosin (H&E) processing, and were used for reference.

### **2.3.2 CT scanning**

The FFPE blocks were CT scanned in the Nikon XT H225 system at 30 kV\*, using 721 projections, and a geometric magnification of 6.0 x, giving a voxel size of 33  $\mu\text{m}$ . The volume was reconstructed using Nikon CT Pro 3D software.

The reconstructed volumes were then processed using an ImageJ<sup>121</sup> script (see Appendix E). This involved cropping and rotating the volume to define the z axis as perpendicular to the cut face and the y axis parallel to the cutting direction, and applying a scale using the calculated voxel size. The first complete image slice from the face of the block was selected and used to determine the position of the calcifications and the fiducial markers. Ellipses were fitted to a thresholded image to determine the marker positions, and the centroid used as the xy position of each hole. The image was then thresholded again to isolate the calcifications, and the centre of the mass of each output to a text file.

### **2.3.3 X-ray fluorescence imaging**

XRF imaging of block faces was conducted using a SII NanoTechnology (now Hitachi) SEA6000VX. Mapping was conducted at 15 kV, with a collimator size of 0.2 x 0.2 mm, collection time of 50 ms per pixel, and at pixel size of 30 - 50  $\mu\text{m}$ . Calcium K $\alpha$  maps were overlaid on a white light blockface image of the same area captured in the XRF scanner. The machine was freshly calibrated with a test target to ensure x-ray beam and visual image were accurately aligned.

### **2.3.4 Visible imaging**

The list of hole and calcification positions generated by the CT scans was used to determine the expected positions of calcifications on the stage of a Perkin

---

\* An accelerating voltage of 30kV was found to be an acceptable compromise between contrast and exposure time.

Elmer Spotlight 200 FTIR microscope. The positions of the holes were measured, and the coordinate system of the CT-derived positions transformed to give a least-squares best fit of the holes to their measured positions. This manipulation included scaling coefficients parallel and perpendicular to the cutting direction, as well as rotation and translation. The hole centre positions under the microscope were determined initially by eye, which enabled the calculated coordinates to be entered directly into the Perkin Elmer Spectrum Image software to drive the stage to the calculated position of the selected calcification. White light transmission maps of the specimens were also analysed to determine the accuracy of the calculated positions.

## **2.4 Results**

### **2.4.1 Qualitative results**

A comparison of thresholded CT images and XRF overlay images of typical specimens is shown in Figure 2-1. It can be seen that there is very good qualitative agreement in the position of calcifications relative to the tissue outlines. The benefits of CT and XRF localisation of calcifications are illustrated in Figure 2-2. It is not obvious from inspection of either the H&E slide (Figure 2-2a) or the unstained tissue (Figure 2-2b) whether there are any calcifications present. In contrast the CT image (Figure 2-2c) at the same magnification clearly shows the location of the calcifications. Comparison with a magnified view of the unstained tissue (Figure 2-2e) enables these to be located. Even in this view, it is doubtful that these features could have been definitively identified as calcifications without CT or XRF views. Examination of the same locations on the H&E slide (Figure 2-2d) shows that in both cases, the calcifications have largely been lost on processing.

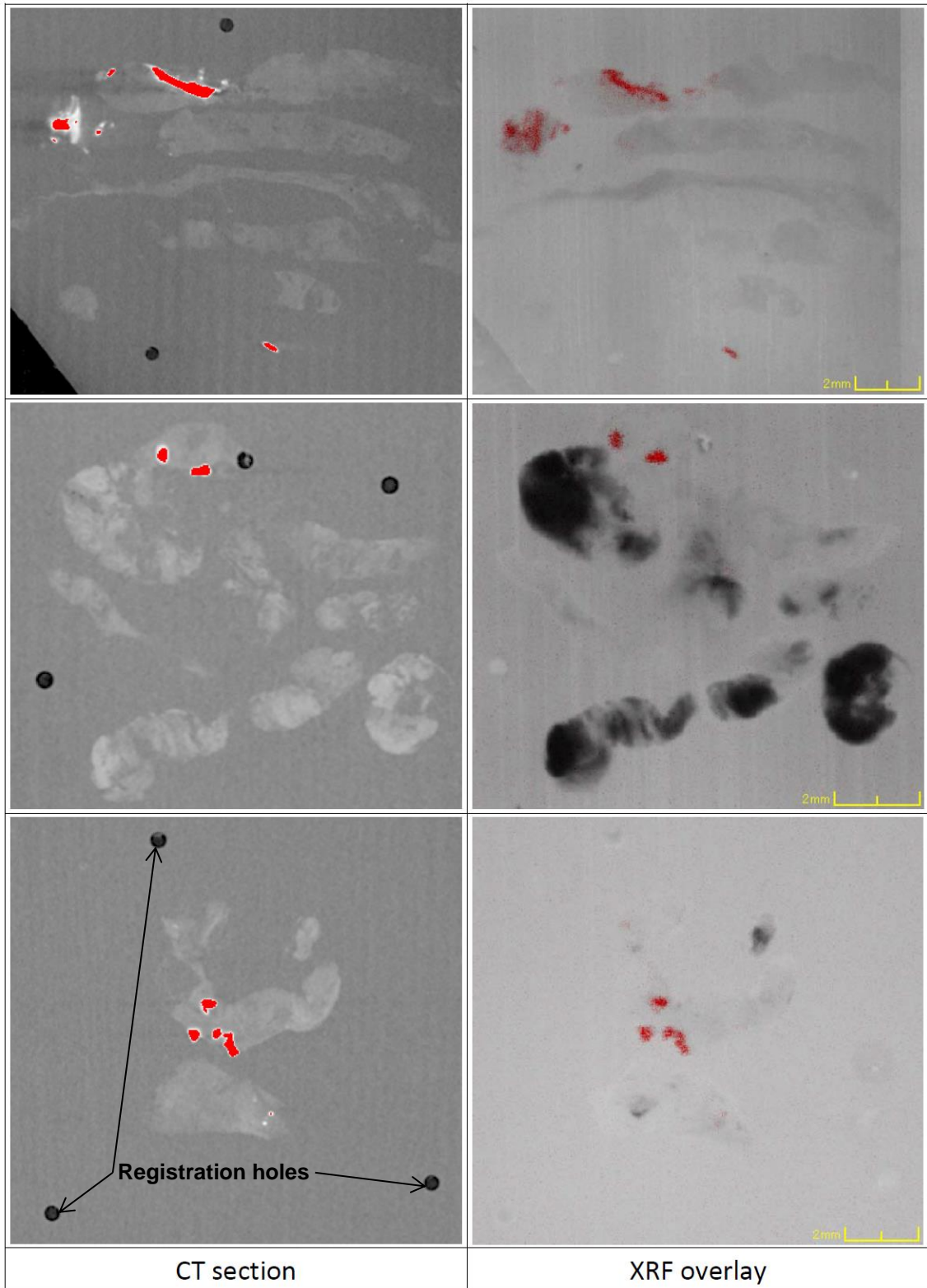
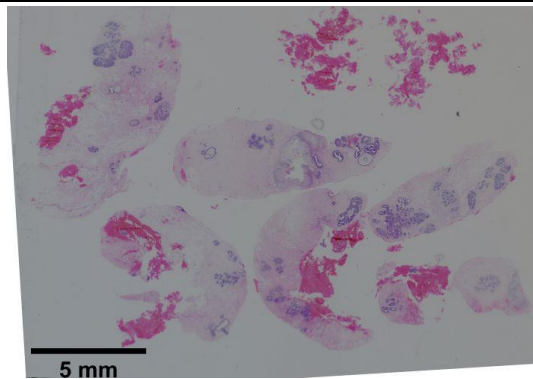
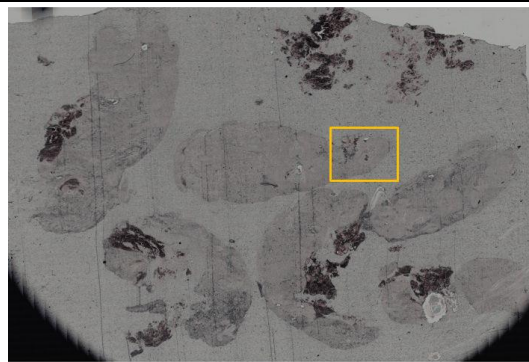


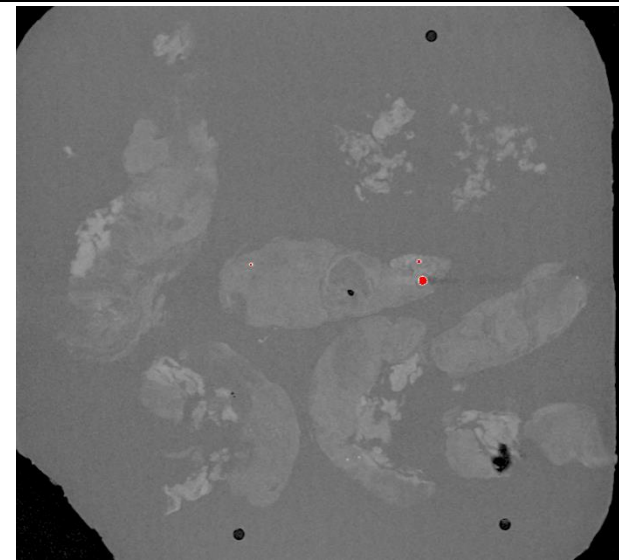
**Figure 2-1: Thresholded CT images and XRF overlay images of three typical FFPE core biopsy breast specimens. The registration holes are clearly visible on the CT slice images, but are less easy to locate on the XRF overlays.**



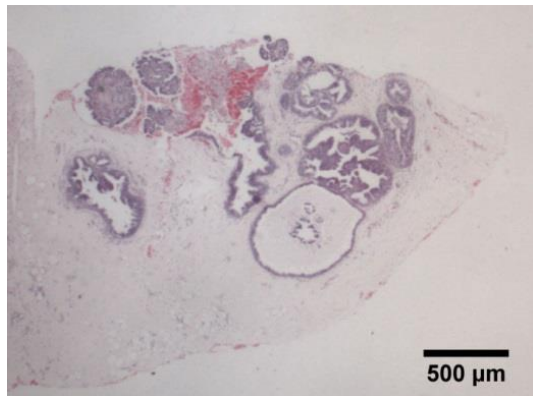
(a) H&E stained, whole section



(b) Unstained, whole section



(c) Thresholded CT image showing location of calcifications in red.



(d) Stained image of area outlined in b.  
Calcifications are not apparent



(e) Unstained image of area outlined in b.  
Calcification positions shown by arrows

Figure 2-2: Standard H&E stained and unstained tissue sections illustrate the difficulty of identifying the location of calcifications without the aid of a CT image.

### 2.4.2 Quantitative analysis

The calculated stretching coefficients from the fitting algorithm revealed that the cut sections were all slightly compressed in the cutting direction. The average length change in this direction was 6.7% (95% CI 8.3% to 5.2%). The average change perpendicular to the cutting direction was small and not significant (0.4%, CI 1.8% to 1.0%). The phenomenon of microtome induced section distortion has been sporadically investigated over many decades, and is reviewed by Jones et al.<sup>122</sup> As with the early studies on the subject, compression occurred in the cutting direction.

The transformed best fit hole positions were a median of 0.064 mm from the measured positions (max 0.22 mm). The predicted position of 31 calcifications within the sections was calculated and a comparison made to the centroid of the corresponding calcification as measured from white light transmission images using ImageJ. Calcification centroids were a median distance of 0.12 mm from the location calculated from the hole positions. Typical examples are shown in Figure 2-3. With five calcifications, this distance exceeded 0.25 mm (max 0.64mm). Four of those were in one specimen, which contained a large linear calcification of approximately 2mm long towards one side of the block, which was disrupted on cutting and may have caused shear distortion of the whole section.



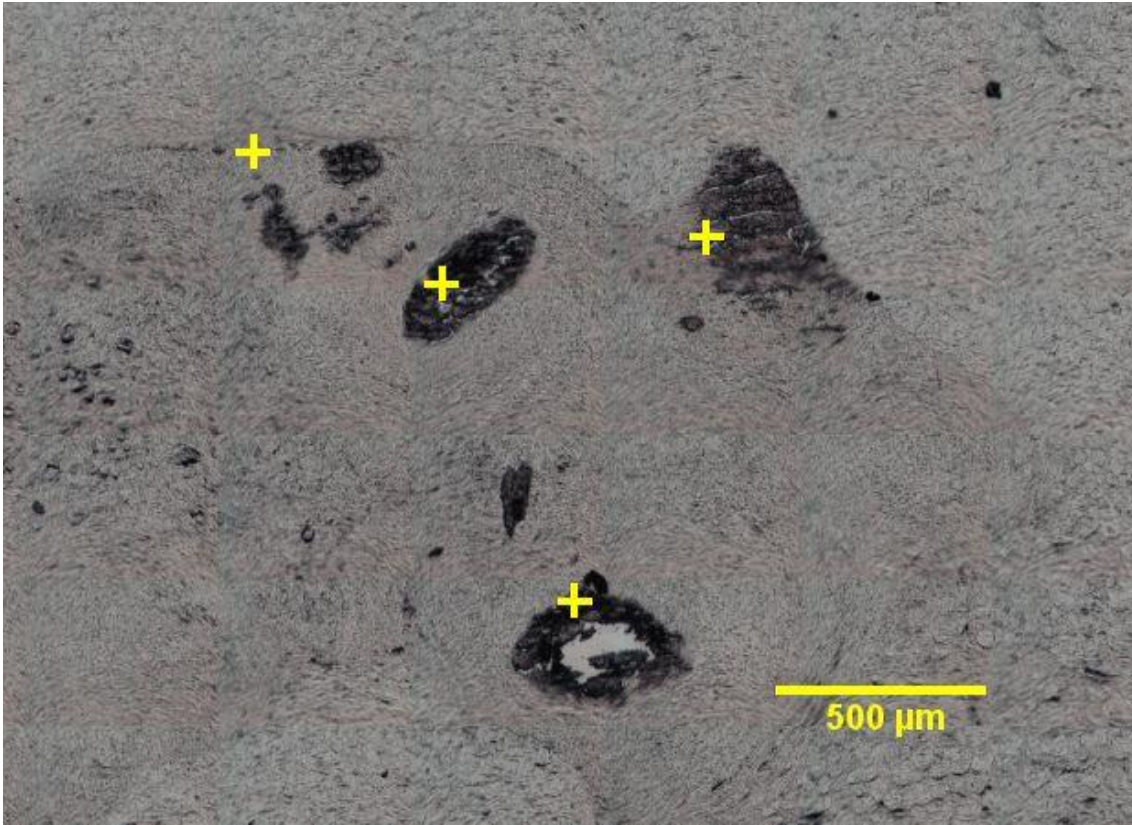


**Figure 2-3 CT-derived coordinates of four calcifications overlaid on a white light image of an unstained section.**

## **2.5 Discussion**

Both CT scanning of tissue blocks and XRF mapping of the block face proved invaluable for locating calcifications within archive FFPE breast tissue specimens and relating this location to a position on a cut section. In many cases, relating the position visually to the tissue outline is sufficient to locate the calcifications. However, use of fiducial markers has been shown to be capable of providing coordinate locations with sufficient accuracy to locate the calcifications visually, despite distortion of these thin tissue sections.

There are advantages and disadvantages to both methods. In CT images, both tissue outlines and fiducial markers are clearly visible, allowing the spatial relationships to be measured directly. This can be seen in Figure 2-1. On the other hand, the tissue outline is not directly visible in the XRF maps, requiring an additional step of registering a visible block face image accurately to the

XRF map and overlaying the images. However, fiducial markers could in principle be located directly by XRF if they contain sufficient concentration of an XRF detectable element (typically  $Z \geq 12$ ).

Ideally these techniques should measure a thin layer within the specimen which is representative of the microtomed section. With CT, it is possible to select an image slice at an appropriate depth beneath the block surface. Note that even though archive blocks have been trimmed to expose tissue and diagnostic sections previously taken, some facing is still necessary to clean up the surface before the first complete and cohesive sections can be taken. This is typically a few tens of micrometres beneath the surface. Although this CT image slice is thicker than the section thickness (33  $\mu\text{m}$  cf. 3 to 8  $\mu\text{m}$ ), it is still substantially smaller than typical dimensions of a microcalcification. XRF derives the calcium signal from a surface layer of the block, the thickness of which depends on the attenuation of the overlying material. The linear attenuation coefficients of calcium  $K\alpha$  radiation (3.7 keV) within breast tissue and cortical bone (a reasonable analogue for breast calcification) are  $92 \text{ cm}^{-1}$  and  $328 \text{ cm}^{-1}$  respectively.<sup>123</sup> About 90% of the XRF signal therefore comes from the top 70  $\mu\text{m}$  of a microcalcification, though a 90% attenuated calcium signal may be detected as much as 250  $\mu\text{m}$  below the surface of soft tissue. XRF is therefore in theory more prone than CT to detection of calcified tissue that over-lies or under-lies the cut section, though in practice this did not appear to be a significant problem.

Spatial resolution, sensitivity, and acquisition time for both CT and XRF are an equipment-specific trade-off. In this case, the resolution of the CT was limited by the specimen pixel size of 33  $\mu\text{m}$ . The resolution of the XRF scanner used was limited by the 200  $\mu\text{m}$  minimum collimator size. However, segmentation of closely spaced particles is not a priority in this application, and the resolution of both CT and XRF scanners was adequate for locating individual microcalcifications. Acquisition time for CT in this study was approximately 30 minutes per specimen, though further work has shown that this could be halved with little sacrifice in image quality. Acquisition time for XRF was longer, in the

range of 45 to 90 minutes, depending on specimen size; this is more difficult to reduce without an unacceptable reduction in either sensitivity or resolution. With this equipment, CT is a significantly quicker technique.

## **2.6 Summary**

A systematic and accurate method to identify the location of microcalcifications in breast biopsy histopathology specimens is of great assistance in studying the chemical composition of these clinically important entities. Both the CT and XRF methods described proved effective of locating calcifications in the surface of wax embedded tissue blocks. Locations could easily be related either to the tissue outline within the wax block or to a coordinate system defined by fiducial markers. These can be matched to locations in microtomed sections, enabling all calcifications present in the section to be studied. Both techniques proved effective, though CT offers some advantages in tissue and marker visibility, depth selectivity, spatial resolution, and speed.



## **3 Dual-Energy X-Ray Imaging**

### **3.1 Aims**

While experimenting with x-ray parameters for locating calcifications by CT scanning of tissue specimens, it became obvious that dual energy x-ray absorptiometry could theoretically be used to differentiate between calcifications of differing composition. There is substantial emerging evidence that the chemical composition of calcifications varies systematically with pathology<sup>63,108,109</sup>. If calcium/phosphorus ratio also differs between benign and malignant cases, then it may be possible to differentiate between them using dual energy mammography.

The aim of this stage of the research was therefore to explore the theoretical potential for using dual energy x-ray absorptiometry to differentiate between calcifications of differing elemental composition, and to conduct a proof of principle experiment to demonstrate that it is possible to differentiate between calcium phosphates with dissimilar calcium to phosphorus ratios.

### **3.2 Introduction**

#### **3.2.1 Dual energy material decomposition**

The concept of using two x-ray photon energies for clinical material discrimination was first proposed in 1963 by Cameron and Sorenson<sup>124</sup> in the second half of their seminal paper on what is now termed single photon absorptiometry (SPA), though the dual energy concept is almost invariably credited<sup>125-127</sup> to later authors. Since then, the comparison of x-ray attenuation of two or more photon energies has spawned a wide range of medical imaging techniques which can discriminate between materials of differing elemental composition. Dual energy techniques take advantage of the fact that the curve of attenuation coefficient vs. x-ray photon energy varies between elements. The mass attenuation coefficient of a mixture or compound is simply the weighted average of its elemental components, hence the attenuation curve for any material can be simply constructed if its elemental composition is known. An example is shown in Figure 3-1, plotted from NIST tables of x-ray mass

attenuation coefficients for standard human tissues<sup>123</sup>. At the lower end of the energy range plotted, photoelectric absorption dominates, which is strongly dependent on atomic number. At the upper end, Compton (inelastic) scatter is the major contributor to attenuation, and in this energy range the attenuation coefficient only varies to a small degree between elements, since the photon energy is much greater than the outer electron binding energy. It can readily be seen that linear combinations of high and low energy images can be used to separate out the contributions of bone and soft tissue. This forms the basis of bone subtraction radiography.

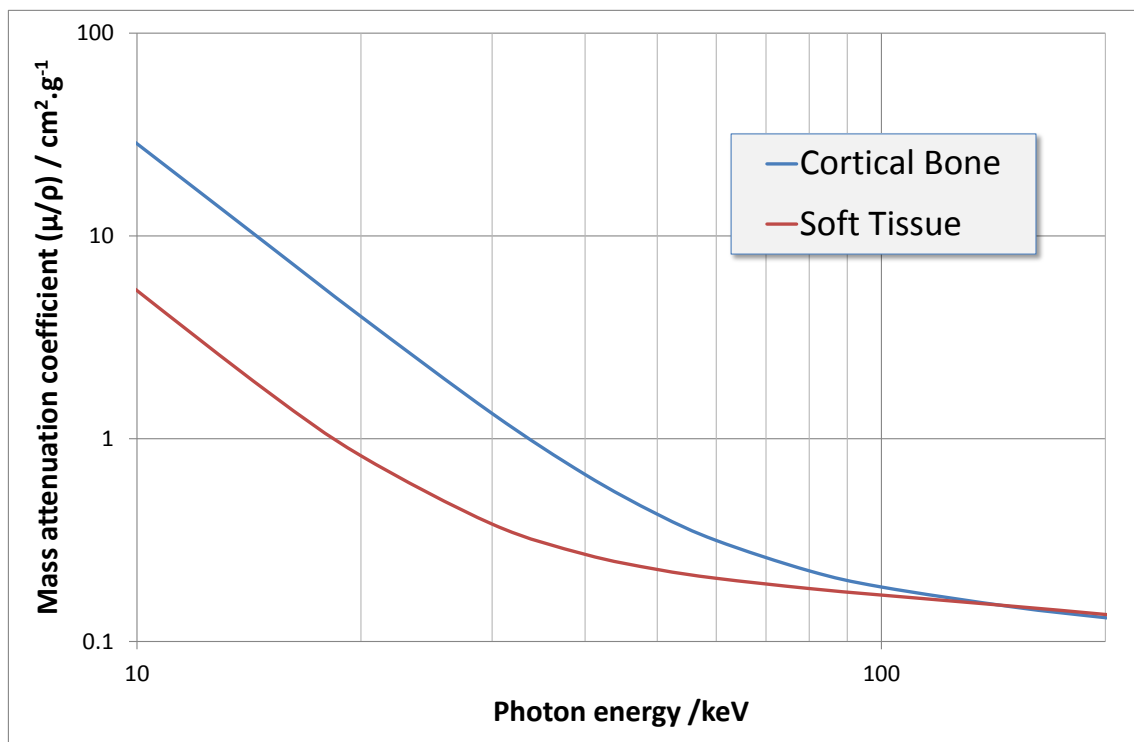


**Figure 3-1 Mass attenuation coefficient of cortical bone and soft tissue vs. photon energy.**

### 3.2.2 Dual energy mammography

In mammography, dual energy subtraction has been employed in two ways. The most common method is termed contrast enhanced digital mammography (CEDM), or sometimes contrast enhanced spectral mammography (CESM). This technique takes advantage of the fact that tumours typically display increased angiogenesis and tissue perfusion<sup>128</sup>. High-energy and low-energy

digital mammograms are taken using x-rays above and below the k-edge of iodine, after administration of an iodine-containing contrast agent. Weighted subtraction can give an image of the contrast agent without the need for a pre-injection image. The conventional application of this technique requires two sequential images at different energies, and careful avoidance of movement between them. However, photon counting detectors are just starting to be introduced into clinical practice,<sup>129</sup> most notably in the Philips Microdose mammography system. Layers within the same detector can discriminate between photons of different energy, hence a dual energy image can be obtained with a single exposure. This effectively removes the need for precise immobilisation between images. In addition, the need for only one exposure rather than two both reduces the radiation exposure to the patient.<sup>130</sup>

The second dual energy mammography technique is similar to bone subtraction radiography, and has been proposed as a method for improved visualisation of calcifications. Most commonly this involves combining a high and low energy image to reduce the contrast between fat and glandular tissue to zero, thus making the calcifications more easily visible against a uniform background. Most studies indicate that using current technology, the minimum detectable calcification size is in general no better than conventional single energy mammography, without increasing the radiation dose to an unacceptable level.<sup>131,132</sup> However, it could increase visibility of calcifications in regions with complex background tissue structure.<sup>131</sup> As with CEDM/CESM, single-shot spectral imaging using an energy discriminating detector has potential for increasing the practicality of this technique by eliminating the need for immobilisation between exposures.

A third use of dual energy mammography is for quantification of breast density<sup>133</sup>. Accurate quantitative measurement is of interest since increased breast density on mammography is associated with a substantially increased relative risk of breast cancer<sup>134</sup>.

### 3.2.3 Calcium/Phosphorus ratio

Interestingly the original paper on the dual energy technique by Cameron and Sorenson<sup>124</sup> explicitly mentions its use to determine the Ca/P ratio of bone:

“The primary mineral elements of bone are calcium and phosphorus, so, in principle, the Ca/P ratio for a particular bone could be determined by measuring  $I_o^*/I$  over the same point on the bone at two different photon energies.”

This appears to have been forgotten until almost precisely the same technique was re-invented by Fountos *et al*<sup>127</sup> 34 years later.

The algebra involved in making the calculation can obscure the simplicity of the underlying concept; for instance the following equation for the Ca:P ratio in Fountos *et al* is:

$$\frac{m_{Ca}}{m_P} = \frac{\ln \left[ \frac{I_w(E_1)}{I_b(E_1)} \right] \cdot (\mu_{PO_4}(E_2) \cdot \rho_{CaPO_4} - \mu_w(E_2) \cdot \rho_w) - \ln \left[ \frac{I_w(E_2)}{I_b(E_2)} \right] \cdot (\mu_{PO_4}(E_1) \cdot \rho_{CaPO_4} - \mu_w(E_1) \cdot \rho_w)}{-\ln \left[ \frac{I_w(E_1)}{I_b(E_1)} \right] \cdot (\mu_{Ca}(E_2) \cdot \rho_{CaPO_4} - \mu_w(E_2) \cdot \rho_w) + \ln \left[ \frac{I_w(E_2)}{I_b(E_2)} \right] \cdot (\mu_{Ca}(E_1) \cdot \rho_{CaPO_4} - \mu_w(E_1) \cdot \rho_w)} \times 3.0679$$

Where:

$m_{Ca}/m_P$	Is the mass ratio of Ca:P
$I_w(E_i), I_b(E_i)$	Are the transmitted intensities through soft tissue and calcified tissue at photon energy $E_i$
$\mu_{Ca}(E_i), \mu_{PO_4}(E_i), \mu_w(E_i)$	Are the mass attenuation coefficients of calcium, phosphate, and water at photon energy $E_i$
$\rho_{CaPO_4}, \rho_w$	Are the densities of hydroxyapatite and water

A simple graphical explanation makes the underlying principles rather easier to visualise.

If attenuation\* is defined as:  $D = -\log_{10} \left( \frac{I}{I_0} \right)$

And  $\frac{I}{I_0} = \exp(-\mu \cdot t)$  [Beer's law]

Then  $D = \frac{\mu \cdot t}{\ln(10)}$

Or alternatively in terms of mass attenuation coefficient (MAC):

$$D = \mu/\rho \cdot \frac{x}{\ln(10)}$$

---

\* 'The term absorbance' (symbol: A) is sometimes used for this quantity, though this is misleading in this context where there are losses in transmitted radiation due to scattering as well as absorption. In 1996 IUPAC endorsed the term 'attenuance' (symbol: D) in its glossary of terms, to replace the term extinction,

$D$  = Attenuance,  $I$  = Transmitted intensity,  $I_0$  = Incident intensity  
 $\mu$  = Linear attenuation coefficient,  $t$  = Thickness  
 $\mu/\rho$  = Mass attenuation coefficient,  $x$  = Mass thickness (mass per unit area)

For a given pixel in a registered pair of images, the mass thickness is a constant, hence the ratio in attenuance between high and low photon energies is equal to the ratio between the mass attenuation coefficients. This is intrinsic to the material, and independent of thickness. Moreover, in a two component mixture, the total high/low attenuance ratio ( $D$ -ratio) of the object will be a mass-weighted average of the component mass attenuance ratios.

Mass attenuation coefficient curves for calcium and phosphate\* are shown in Figure 3-2. Since this is plotted on a log-log scale, the magnitude of both the photon energy ratio and the attenuance ratio (equal to the mass attenuation coefficient ratio) can be visualised directly from the chart.

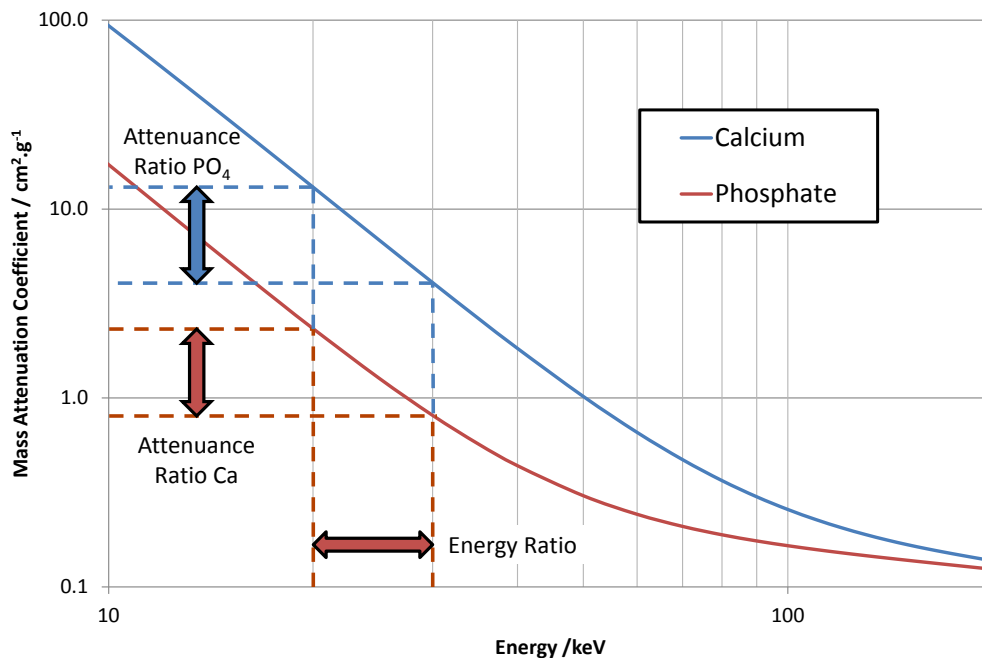


**Figure 3-2 The attenuance ratio attributable to material components can be visualised directly from a log-log chart of mass attenuation coefficient vs. photon energy.**

\* The justification for this simplification in the composition of nonstoichiometric calcium phosphates is that the balancing O and H make a trivial difference to the mass attenuation coefficients. This is explained by Fountos et al.<sup>127</sup>

Different material compositions can be distinguished most easily by choosing high and low photon energies that maximise the contrast in attenuation ratio for the two materials. The difference in D-ratios between two materials, as a function of high and low photon energy, can more easily be visualised by differentiating the log-attenuance curves with respect to energy. This is depicted in Figure 3-3. The area under the curve between the two selected photon energies corresponds to the log of the D-ratio of each component, and the area bounded by the two curves and the two photon energies is proportional to the log of the ratio of the two D-ratios. This visualisation could be useful in selecting appropriate high and low photon energies. From this it can be seen that a lower photon energy of less than  $\sim 10^{1.25} \approx 18$  keV is counterproductive for Ca:P measurement.

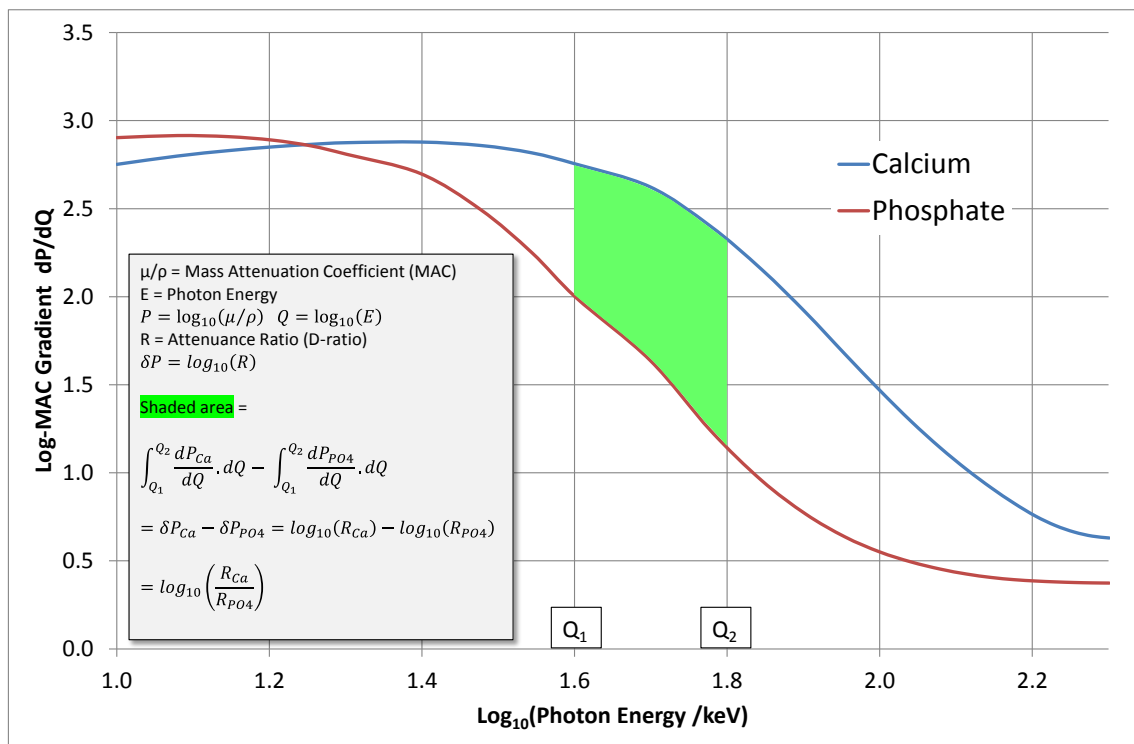


**Figure 3-3 Gradient of log-MAC for calcium and phosphate with respect to log photon energy.**

It might be concluded from that for optimal discrimination between components the photon energies should be chosen to maximise the area depicted in Figure 3-3. However, there are other practical constraints limiting the accuracy of

measurements at high or low energies. This is illustrated in Figure 3-4, which shows the transmission through a clinically realistic combination consisting of 50mm of breast tissue and a 500 $\mu$ m thick calcification. Calculations are based on NIST data for cortical bone<sup>123</sup> (as an analogue for the calcification) and for NIST breast tissue\*. It can be seen that at low energies the % transmission is low, rendering the calculations susceptible to counting-statistic errors and detector zero-errors. At high energies, the contrast between calcifications and background are low, which would amplify errors due to background subtraction. Calculation of an optimum range would require detailed knowledge of the characteristics of the detector used.

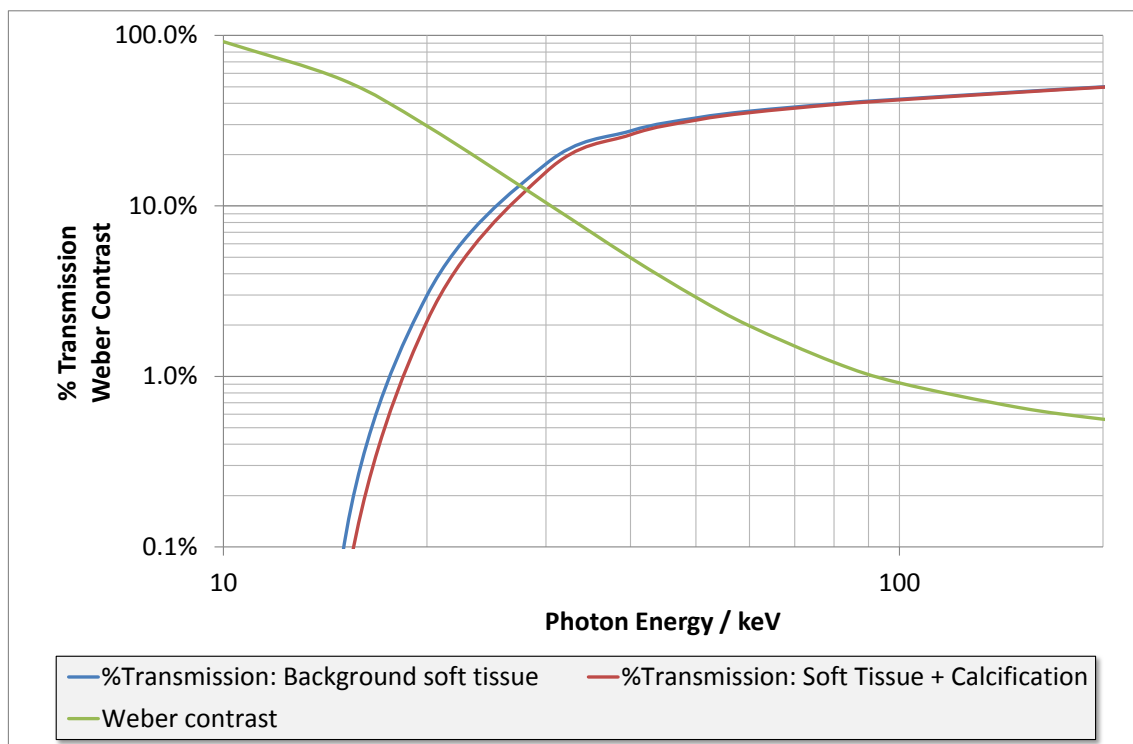


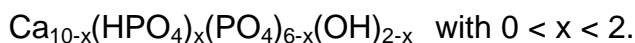
**Figure 3-4 Total x-ray transmission and Weber contrast<sup>†</sup>, as a function of photon energy, through 50mm of breast tissue and a 500 $\mu$ m thick calcification.**

\* The attenuation values in the NIST tables for breast tissue appear to represent rather dense breast tissue with only a small proportion of fat, when compared with other published attenuation coefficients for fat and fibroglandular tissue in the breast<sup>210</sup>.

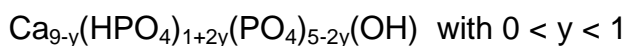
<sup>†</sup> Also known as Luminance Contrast. This is defined as  $(I_f - I_b)/I_b$ , where  $I_f$  is the intensity of the feature and  $I_b$  is the intensity of the background.

If the material of interest is not isolated but embedded in a matrix (as with a calcification in breast tissue), the attenuation attributable to the calcification needs to be separated from the attenuation due to the matrix. A uniform background around the feature of interest can simply be subtracted. Background subtraction is also straightforward where the background can be reliably interpolated over a small feature such as a calcification. Allowance also needs to be made for the fact that the calcification displaces matrix volumetrically rather than sitting on top of it. This adjustment can simply be made by subtracting the linear attenuation coefficient of the matrix from the calcification, effectively giving an incremental attenuation coefficient for the material of the calcification.

Theoretical D-ratios have been calculated for photon energies of 20keV and 40keV for a range of stoichiometric calcium phosphate materials and plotted against Ca:P ratio in Figure 3-5. Note that monocalcium phosphate and tetracalcium phosphate are not found *in-vivo*, but have been included to illustrate the extremes of Ca:P ratio of calcium phosphates. Tricalcium phosphate is only found *in-vivo* in its magnesium stabilised form in whitlockite. Non-stoichiometric apatites with varying Ca:P ratio can also form, in which a variable proportion of the trivalent phosphate ions have been protonated to become divalent hydrogen-phosphate ions, and charge balance maintained by a combination of calcium ion and hydroxide vacancies. A frequently used generic formula for this calcium deficient apatite is given as:



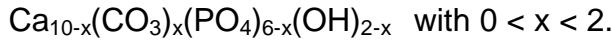
However, it has been suggested<sup>135</sup> and confirmed<sup>136</sup> that when Ca:P ratios of less than 1.5 (i.e.  $x > 1$ ) that a different formula fits experimental data better:



D-ratios have been therefore calculated for photon energies of 20keV and 40keV using the first formula for Ca:P ratio 5:3 to 3:2 (i.e.  $0 < x < 1$ ) and the second formula for Ca:P ratios 3:2 to 4:3 (i.e.  $0 < y < 1$ ). These have been added to the plot in Figure 3-5.



The effect of carbonate substitution on D-ratios has also been calculated and plotted in Figure 3-5. In Type-B substitution, which is generally believed to dominate in biological apatites, phosphate substitution occurs in the same way as hydrogen phosphate, i.e.:



In one study showing a variation in carbonate substitution with pathology, mean carbonate levels in calcifications were found to be 2.1 wt.% in benign tissue and 1.4 wt.% in invasive carcinoma. Points corresponding to these two levels of carbonate have therefore been plotted. It can be seen that according to this substitution model, increased carbonate levels increase the Ca:P ratio and decrease the D-ratio, though at the levels observed in breast calcifications, the effect is very small.

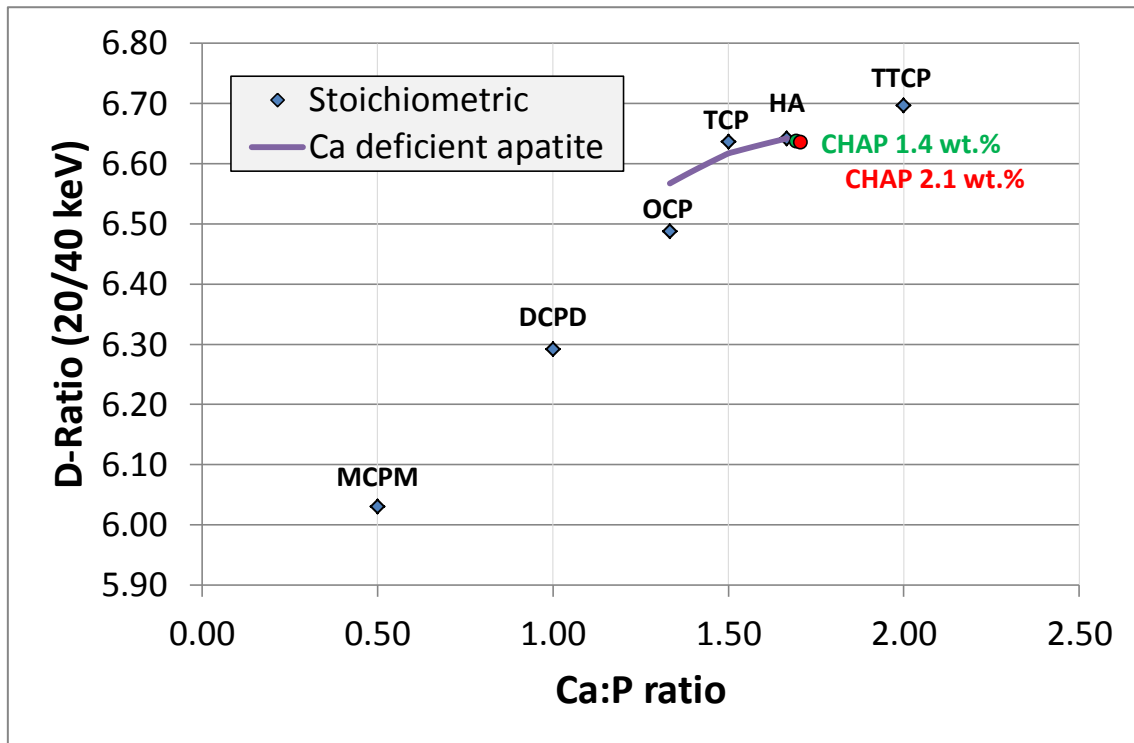


Figure 3-5 D-ratio of stoichiometric calcium phosphates, calcium deficient apatite, and carbonated hydroxyapatite. Abbreviations are given in Table 3-1.

Abbreviation	Common name	Formula
MCPM	Monocalcium phosphate monohydrate	$\text{Ca}(\text{H}_2\text{PO}_4)_2 \cdot \text{H}_2\text{O}$
DCPD	Dicalcium phosphate dihydrate (Brushite)	$\text{CaHPO}_4 \cdot 2\text{H}_2\text{O}$
OCP	Octacalcium phosphate	$\text{Ca}_8\text{H}_2(\text{PO}_4)_6 \cdot 5\text{H}_2\text{O}$
TCP	Tricalcium phosphate	$\text{Ca}_3(\text{PO}_4)_2$
HA	Hydroxyapatite	$\text{Ca}_{10}(\text{PO}_4)_6(\text{OH})_2$
TTCP	Tetracalcium phosphate	$\text{Ca}_4(\text{PO}_4)_2\text{O}$
CHAP	Carbonated hydroxyapatite	$\text{Ca}_{10-x}(\text{CO}_3)_x(\text{PO}_4)_{6-x}(\text{OH})_{2-x}$ Where $x = 0.23$ and $0.34$

**Table 3-1 Abbreviations used in Figure 3-5**

Type I calcifications comprised of Calcium oxalate dihydrate ( $\text{CaC}_2\text{O}_4 \cdot 2\text{H}_2\text{O}$ ), would have a D-Ratio of 5.92 for these photon energies, but is not depicted on this chart since the Ca:P ratio is infinite.

### 3.2.4 Polychromatic radiation

One simplification that has been made in this explanation is the assumption that the radiation used is monochromatic. In SPA and DPA, this is achieved with the use of radioisotopes which emit radiation of a specific photon energy. The isotopes used by Cameron and Sorenson<sup>124</sup> were  $^{125}\text{I}$  (27.3 keV) and  $^{241}\text{Am}$  (59.6 keV), whereas Fountos *et al*<sup>127</sup> chose  $^{153}\text{Gd}$  for high energy radiation, emitting at 97.5 and 103.2 keV (mean 99.9 keV). Radionuclide sources have substantial disadvantages, not least cost, limited life, and impracticality for high resolution wide area imaging. As a result, x-ray tubes superseded radionuclide sources for clinical densitometry by the early 1990s. One disadvantage of an x-ray tube as a source is that it generates polychromatic radiation, which is subject to beam hardening; this is a potential source of inaccuracy in

quantitative absorption measurements<sup>137</sup>. However, choice of suitable filters can reduce such inaccuracies to a negligible level<sup>138</sup>.

### 3.3 Proof of Principle Experiments

#### 3.3.1 Introduction

#### 3.3.2 Materials and Methods

Discs were prepared from CamCeram III hydroxyapatite (CAM Bioceramics) which has a certified atomic Ca:P ratio of 1.667, and from calcium hydrogen phosphate\* (Sigma Aldrich) which has a Ca:P of 1.0. Each powder was pressed into four Ø10mm discs with a nominal thickness of 0.3, 0.4, 0.7 and 1.0 mm, using a Specac pellet die. These were mounted on a 3mm thick PMMA sheet and mounted in a Nikon XT H225 CT scanner perpendicular to the beam. Tube voltages of 35kV and 60kV were found to give appropriate transmission/attenuation through specimens in the chosen thickness range. Three exposures were taken at each voltage: a dark frame (x-rays switched off), a white frame (x-rays on but sample out of view), and a sample frame. The X-ray flat panel detector (PerkinElmer XRD 1620) exhibits substantial ghosting and lag, typical of this type of amorphous silicon imaging panel<sup>139,140</sup>, hence care must be taken with quantitative measurements. To address this, the dark signal from the panel was allowed to stabilise prior to all images. The panel was deemed to have stabilised when the mean pixel dark signal reduced by less than 4 levels (in a 16 bit signal) in the previous 60 seconds. That could take up to 30 minutes depending on the previous exposure. White frame and sample exposures were started precisely 60 seconds after the x-rays were switched on. This delay allowed the x-ray tube to stabilise and ensured that the panel signal only ramped up slowly during the exposure. All stabilisation measurement and exposure timing was automated with a VBA program to ensure reproducibility.

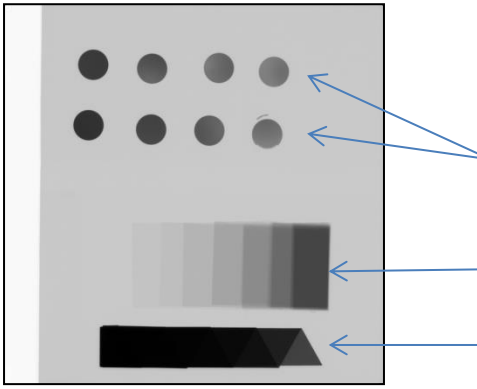
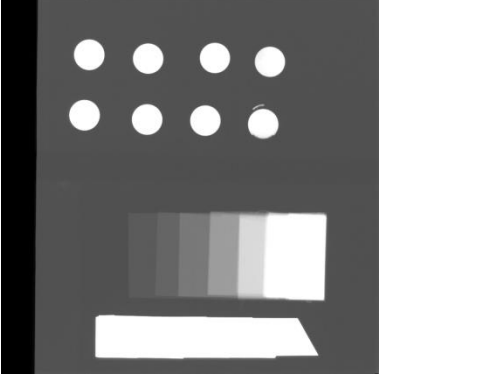
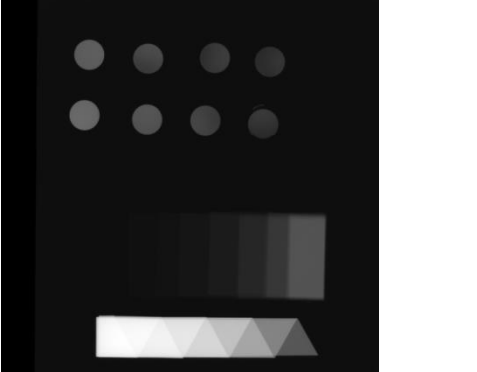
---

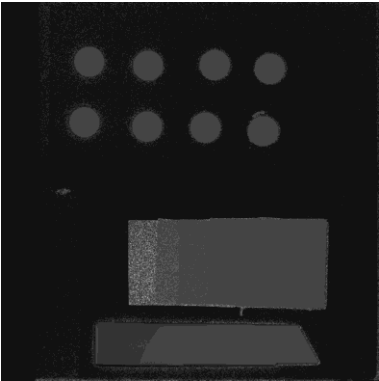
\* Also known as also known as dicalcium phosphate or calcium phosphate, dibasic. The IUPAC term is calcium hydrogen phosphate.

Images were processed in ImageJ. A transmittance image was created by subtracting the dark frame from the sample frame, then dividing by the pixel range given by the white frame minus the dark frame. Pixel values were thus in the range of 0 to 1. The other processing steps are shown in the results section.

### 3.3.3 Results

Images showing the processing steps are shown in Figure 3-6

<p>A</p>		<p>Transmittance image with pixel values in range 0 to 1</p> <p><i>Calcium hydrogen phosphate (top row)</i> <i>Hydroxyapatite (bottom row)</i></p> <p><i>Aluminium step wedge</i> } <i>Not used</i> <i>Copper step wedge</i> }</p>
<p>B</p>		<p>Apply <math>-\log_{10}</math> transform to obtain attenuance image.</p>
<p>C</p>		<p>Calculate median value of background from the region surrounding the discs and subtract from the image. Apply global minimum attenuance of <math>10^{-6}</math> to avoid a zero denominator in the next step.</p>

D		<p>Divide low energy attenuation image by high energy attenuation image to obtain an attenuation ratio image.</p>
---	---	---

**Figure 3-6 Image processing steps to derive attenuation ratio image from two transmittance images.**

If a colour scale is applied to the image, it can be seen from Figure 3-7 that the top row, consisting of calcium hydrogen phosphate can be clearly distinguished from the bottom row consisting of hydroxyapatite, and that the different thicknesses of discs do not affect the D-ratio. A histogram of mean D-ratio for the central 90% of each disc is given in Figure 3-8.

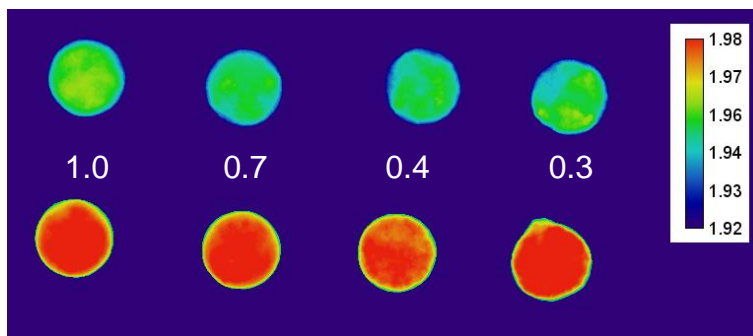


**Figure 3-7 Dual energy imaging clearly distinguishes discs of hydroxyapatite (bottom row) from calcium hydrogen phosphate (top row). Labels refer to nominal thickness in mm.**

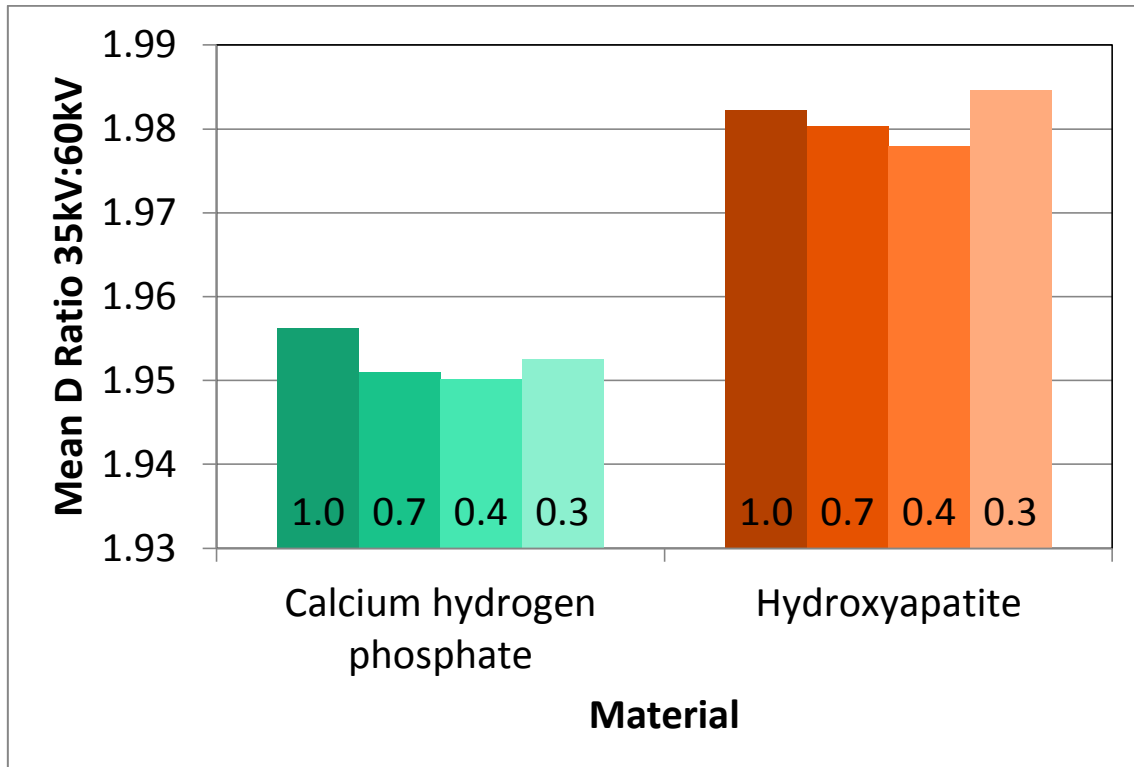


Figure 3-8 Mean D-ratio as a function of material and disc thickness in mm.

### 3.4 Summary

The principle of dual energy material discrimination is well established and has successfully been used to differentiate between calcified tissue with different Ca:P ratios. Spectral mammography is also increasingly used, though this is mostly used in conjunction with a contrast agent in CEDM/CESM, or less commonly, for improved visualisation of calcifications. Theoretically, therefore, it may be possible to use this technique to differentiate between calcifications with a different Ca:P ratio. The small size of the microcalcifications resulting from malignant processes in breast cancer does present some substantial technical challenges.

Scattering of x-ray photons by breast tissue is a significant source of image degradation in mammography, and is a major obstacle to accurate quantitative measurement of attenuation<sup>141</sup>. The scattered x-rays form a background which reduces the contrast of the image. In conventional mammography, moving antiscatter Bucky-Potter grids are used to reduce the effect of scatter. These

consist of high aspect-ratio lamellae that absorb scattered at angles greater than the acceptance angle of the grid. These can greatly improve the image contrast, though there is still substantial residual scatter, particularly in thicker breasts. Improved scatter rejection constructs have been developed, and multi-slit collimation (as used in the Philips Microdose system) have demonstrated substantial reduction in the scatter-to-primary ratio compared to conventional mammography<sup>142</sup>. Use of a pencil beam, as suggested by Ghamraoui *et al*<sup>107</sup>, would further reduce the effect of scatter, though has obvious practical drawbacks. The accuracy of quantitative attenuation measurements can be further improved by the use of postprocessing algorithms to correct for residual scatter in the image<sup>141</sup>.

The finite spot size of the source leads to loss of spatial resolution of the image. This is known as geometric unsharpness, and is likely to be a major challenge for quantitative measurement of attenuation in particles as small as breast calcifications. Quantitative measurement of attenuation can only be made in the umbra, which requires the spot size to be small relative to the calcification. New developments such as liquid metal jet anodes<sup>47,50</sup> may enable a sufficiently small spot to be used without an unacceptable increase in exposure time, which would itself run the risk of motion blurring.

As with scatter correction, it is theoretically possible to use computational de-blurring to compensate for a limited degree of geometric unsharpness. The captured image is a convolution of the true image and the point spread function (PSF) of the system. If the PSF can be measured, it is theoretically possible to reconstruct a de-blurred image by deconvolution. In the absence of noise, this can be achieved by dividing the Fourier transform of the image by the Fourier transform of the point spread function. However, in practice this simple approach is extremely sensitive to noise, and also requires the PSF to be very accurately known. To overcome this, numerous deconvolution algorithms have been developed such as Wiener filtering or the Richardson-Lucy method. These are widely used in image processing, particularly in microscopy and astronomy. However the main aim of these is to resolve closely spaced objects

rather than accurate reconstruction of grey levels, which is necessary for dual energy material decomposition.

A challenge in dual energy imaging consists of accurate registration of high and low energy images. This would be particularly critical for calcification imaging, since a very small shift in source, or breast, or detector would result in artefacts when combining the images. Rapid cycling of the x-ray source voltage (known as rapid kV switching) is frequently employed in dual energy CT. This has the advantage of minimising movement artefacts, but does have some limitations. It is difficult to cycle the tube current sufficiently quickly to balance the x-ray flux at high and low energies<sup>143</sup>. In addition, it is not feasible to vary the anode material or to optimise the filtration for the two energies to minimise beam hardening, which is source of inaccuracy in quantitative absorption measurements<sup>137</sup>. A very promising new technology for spectral imaging is the energy discriminating photon counting detector<sup>129</sup>. Rather than varying the source energy, the energy of transmitted photons is measured in the detector. This has even better immunity to motion and perfect image registration since high and low energy images are acquired in the same detector at the same time. These detectors are in clinical use for mammography<sup>144</sup>.

The challenges involved in using dual energy absorptiometry to differentiate between calcifications of differing elemental composition are substantial, but largely technological in nature. One possible enabling technology is the use of liquid jet x-ray sources. These have two theoretical advantages. Firstly, the high energy density possible would enable a reduced spot size to be used without the penalty of a long exposure time. The consequent reduction in geometric unsharpness would help to achieve sufficient spatial resolution for quantitative measurement of attenuation. In addition, the high intensity would enable more rigorous pre-collimation, such as in a slit or slot scanning configuration, or even a pencil beam, without excessive reduction in flux and the consequent unacceptable increase in exposure time. This would help reduce attenuation error due to scatter. Another enabling technology is the use of energy resolving x-ray detectors, allowing single-shot spectral imaging. This



overcomes many potential problems with immobilisation and alignment of sequential images.

For any of these there does need to be a diagnostically useful variation in elemental composition with pathology. This is explored in the next chapter.

## 4 Elemental Analysis

### 4.1 Aims

In order for dual energy x-ray absorptiometry, described in the previous chapter, to yield clinically useful information on calcification composition, there does need to be a detectable difference between calcifications in benign and malignant cases. The principal aim of this phase of the research was therefore to determine whether there is a sufficient variation in Ca:P ratio with pathology for this parameter to have diagnostic potential.

Secondly, despite the importance of calcifications in early detection of breast cancer, and the evidence that they may play an active role in breast cancer progression, our current understanding of the elemental composition of breast calcifications remains very sketchy. Measurement of elemental composition and its relationship to pathology may offer insights into the processes involved in genesis and growth of these clinically important entities.

Most of the content of this chapter has been previously published<sup>145</sup>.

### 4.2 Background

Qualitative elemental composition of breast calcifications has previously been studied using electron microscope x-ray spectroscopy<sup>63,84,88,90-92,146</sup>. The majority of these studied calcifications that had been microdissected or digested from bulk soft tissue, though the two TEM studies used thin sections<sup>63,88</sup>, and one SEM study<sup>146</sup> used frozen sections. These qualitative studies mostly identified just calcium and phosphorus, though one found a higher incidence of calcifications containing magnesium in malignant specimens<sup>63</sup>, and two noted the presence of other elements such as Na, Mg, Cl, K<sup>84,92</sup>, and S, Si<sup>84</sup>.

One small semi-quantitative SEM-WDS study reported the Ca/P ratio of three benign and two malignant specimens, with an average of 9 spectra per specimen. The authors reasoned that, although the specimens were porous and not polished, the effect of these drawbacks would be mitigated by calculating elemental ratios. However, as discussed in the methods section of

this chapter, this is not a safe assumption since it is well established that low atomic number elements will be much more susceptible to shadowing than elements of a higher atomic number<sup>147</sup>.

The level of magnesium in calcifications is of interest since studies have shown that magnesium levels both influence and are influenced by the process of carcinogenesis<sup>148,149</sup>. Magnesium in breast calcifications has been detected in a previous study<sup>63</sup>, with the proportion of specimens containing magnesium increasing from benign to *in-situ* to invasive. This observation may provide a clue as to why carbonate levels are lower in calcifications associated with cancer. It has recently been shown that magnesium ions can strongly inhibit the incorporation of carbonate in hydroxyapatite<sup>150</sup>. Increased concentration of magnesium within cancer cells could lead to higher magnesium levels within calcifications, leading in turn to lower carbonate levels in calcifications associated with breast cancer.

In contrast, significantly lowered serum magnesium levels have been found in breast cancer patients<sup>148</sup>, and it has been suggested that a low Mg:Ca ratio is risk factor in the development of postmenopausal breast cancer<sup>151</sup>. A possible resolution of this apparent contradiction is that a peculiarity of tumour cells is their avidity for Mg, which accumulates within the cells even when extracellular Mg concentrations are low<sup>151,152</sup>.

## **4.3 Materials and Methods**

### **4.3.1 Archive blocks**

Formalin Fixed Paraffin Embedded (FFPE) core biopsy breast specimens were selected from the Gloucestershire Hospitals NHS Foundation Trust diagnostic archive (under approval from Gloucestershire Local Research Ethics Committee). Blocks were randomly selected from the 2012 archive, subject to the presence of calcifications in the histopathology report, and an unambiguous classification of “B2 - Benign”, “B5a - Ductal Carcinoma *In-Situ*”, or “B5b - Invasive Carcinoma”<sup>22</sup>. For the purposes of analysis, specimens were also grouped as “Benign” (B2) vs. “Malignant” (B5a or B5b). A summary of the

histopathology report for each of the specimens analysed is given in Appendix B. These were screened by mounting the blocks in a Nikon Metrology XT H225 CT system and imaging at 20 kV both perpendicular and parallel to the face of the block. Following screening, blocks were selected with significant levels of calcification at or near the cut surface. The selected blocks were then CT-scanned, and the reconstructed volumes processed as described in Chapter 2 to identify the position of calcifications relative to the tissue outlines at the surface of the blocks.

### **4.3.2 Mounting**

Three sequential microtome slices of 5  $\mu\text{m}$  were cut from each block. The first slice underwent standard H&E (haematoxylin and eosin) processing, and was used for reference. Figure 4-1 shows typical H&E images of calcifications within specimens classified as B2, B5a, and B5b. The second slice from each block was mounted on a polished  $\text{\O}25\text{mm}$  aluminium alloy SEM stub, and was used for elemental analysis described in this chapter. The third slice was mounted on polyolefin heat shrink film for additional analysis by x-ray diffraction. Full experimental details are described in Chapter 5.

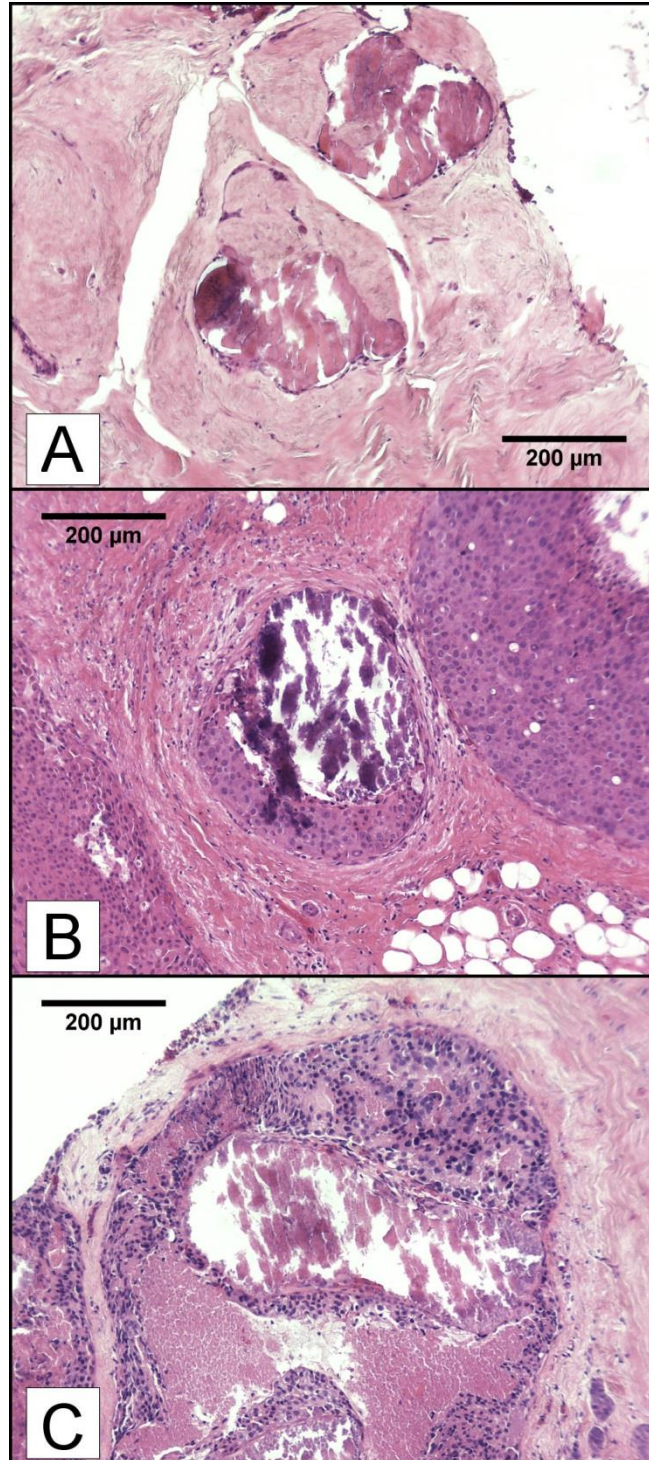


Figure 4-1 H&E stained images of typical calcifications: (a) Specimen X44 (B2), (b) Specimen X53 (B5a), (c) Specimen X46 (B5b). Histopathology summaries can be found in Appendix B.

### 4.3.3 X-Ray microanalysis

Elemental composition was measured using Energy-dispersive X-ray spectroscopy (EDS) in a Philips XL30 ESEM with an Oxford Instruments SiLi detector. The working distance was 12mm, and approximately 200,000 total counts were taken per point measurement. A total of 2,789 spectra were collected from 66 calcifications in 31 specimens. Composition was calculated in AZtec 2.1 (Oxford Instruments). Measurement of composition in this type of specimen presents several challenges, which must be addressed in order to obtain reproducible results.

### 4.3.4 Charging

It was initially hoped that a 5µm thick histological section in intimate contact with a polished aluminium SEM stub could be analysed under high vacuum without specimen charging, and indeed this proved to be the case with wax embedded soft tissue. However, the calcifications were fragmented by the microtome blade, frequently resulting in elevated flakes with only an edge in contact with the substrate. As a result, severe charging was observed with many calcifications. This could not be eliminated by carbon coating, due to the fragmented nature of the surface. Charging was eliminated by operating the SEM in environmental mode, with water vapour pressure 93 Pa (0.7 Torr). This also removed the need for carbon coating. Absence of charging was confirmed from observation of the Duane-Hunt bremsstrahlung limit. One potential bias introduced by operating in environmental mode is scattering of the beam, and consequently contamination of point measurements with signals from the 'skirt' of scattered electrons. With a working distance of 12mm and a 20kV accelerating voltage, only about 57% of the electron beam remains unscattered (scattering less than  $10^{-6}$  Rad)<sup>153</sup>. In principle, therefore, measurements of a calcification could include a substantial contribution from surrounding soft tissue. To assess the magnitude of this effect, the typical contribution from soft tissue in biopsy cores containing calcifications was measured. Under identical collection conditions, soft tissue counts for phosphorus and calcium were approximately 2 and 3 orders of magnitude (respectively) lower than the counts

from a calcification, and magnesium was below the level of detection. Theoretically, therefore, the Ca:P ratio could be underestimated by up to ~0.4% in a very small calcification as a result of the contribution from the skirt. In practice, this is substantially lower than other sources of variation for these measurements, hence can be disregarded. For verification, measurements on a small (~Ø10µm) unfragmented calcification showed no significant variation in the Ca:P and Mg:Ca ratios with pressure over a range of 40 – 130 Pa (0.3 – 1.0 Torr).

#### **4.3.5 Specimen thickness**

If the electron beam penetrates through the specimen to the substrate, this complicates the calculation of elemental concentrations, particularly if the local thickness varies within the skirt region of gas-scattered electrons. This difficulty can be eliminated if the combination of specimen thickness and beam energy ensures minimal beam penetration to the substrate. Using cortical bone as an analogue for the calcification matrix, the electron penetration depth of an unscattered 20kV beam into a 5µm thick slice was calculated using winCasino v2.48<sup>154</sup>. This program is based on Monte Carlo simulation of electron trajectories in solids. Elemental composition and density of cortical bone were taken from a NIST database<sup>123</sup>. The curves in Figure 4-2 show normalised x-ray intensity as a function of depth [commonly termed  $\phi(\rho z)$  curves]. This, and the corresponding energy density cross section in Figure 4-3, show that at 20kV and slice thickness of 5µm there is negligible penetration of electrons to the substrate. A straightforward bulk analysis calculation can therefore be performed.

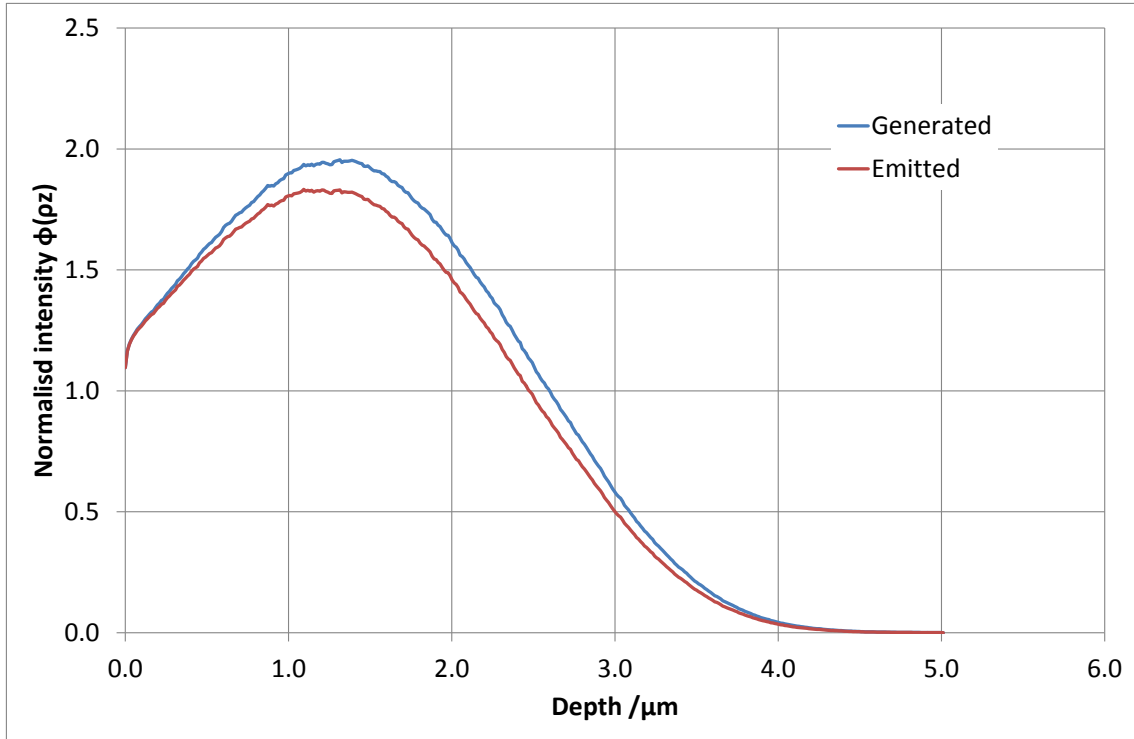


Figure 4-2 WinCasino 2.48 was used to create a  $\phi(\rho,z)$  curve for generation and emission of Ca  $K\alpha$  x-rays vs. depth with 20keV electrons into a 5 $\mu\text{m}$  layer of cortical bone. It can be seen that there is negligible penetration of x-rays to the substrate.



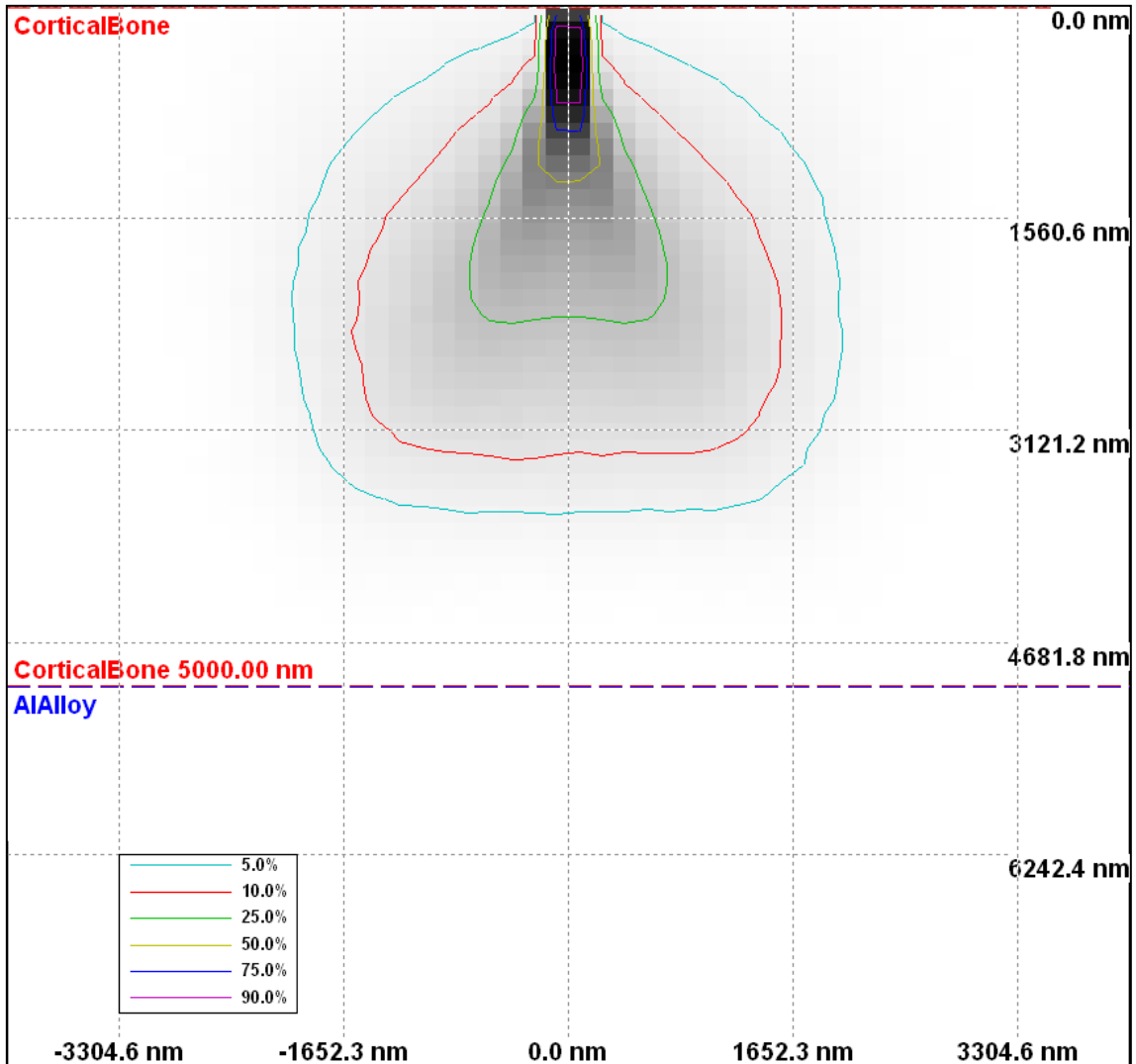


Figure 4-3 Cross section view of absorbed energy density in a 5µm layer of cortical bone on an aluminium alloy substrate.

#### 4.3.6 Topography

The chemical composition within breast calcifications has been found to be very inhomogenous<sup>155</sup>, hence an area measurement over the whole cut surface of a calcification is an attractive option for measuring the average composition. However, as a result of fragmentation by the microtome blade, the calcification surface is not smooth and perpendicular to the beam. The local orientation of the surface relative to the electron beam and the detector can have a very substantial effect on the measured elemental concentrations. Moreover, this effect is not symmetrical; the disproportionate reduction in low energy x-rays

from areas tilted away from the detector is not compensated by the areas oriented towards the detector, hence simple area averaging over the whole calcification will underestimate the concentration of low atomic number elements. The reduction in overall count rate from the areas tilted away from the detector mitigates this effect, but does not eliminate it. There are several strategies that can be adopted to correct for these topographic errors.

One option is to measure the peak to local background ratio. Since the background signal originates from the same electron interaction volume as the characteristic x-rays, it will be subject to the same absorption effects, and hence can be used to correct approximately for topographic errors. A practical problem with this approach is that the peak to background ratio in this measurement configuration is typically large (50:1 for calcium in this case) thus an excessively long collection time is needed to acquire sufficient background signal to calculate an adequately precise peak to background ratio.

Another approach is to take repeat point measurements in multiple specimen orientations, either by rotating the specimen around the beam axis, or with the use of multiple detectors. A simpler alternative to obtaining an average composition for the calcification involves measurement of multiple points over the calcification surface; if the orientation of measurement points in the beam-specimen-detector plane is symmetrically distributed relative the specimen normal, then the median measurement will approximate to the median composition with a surface orientation normal to the beam axis. This was verified with measurements distributed over the surface of a 70 $\mu$ m spherical particle of synthetic hydroxyapatite. In some cases there was evidence of systematic orientation of flakes comprising the calcification, due to the directional cutting action of the microtome blade. A hybrid approach was therefore adopted, consisting of measuring multiple points, rotating the specimen by 180°, and measuring another set of points. The median and confidence interval of the elemental ratios of interest was calculated for the combined set of points using Efron's nonparametric bias-corrected and accelerated (BCa) bootstrap method in R<sup>156,157</sup>. Based on the 95% confidence

interval, the mean precision of the median for a set of measurements on a calcification was  $\pm 3.4\%$  for Ca:P ratio, and  $\pm 16\%$  for both Mg:Ca and Na:Ca ratios.

## **4.4 Results**

### **4.4.1 Calcification Morphology**

An SEM-EDS image of a typical calcification is shown in Figure 4-4. The aluminium signal derives from the substrate revealed by cracks in the calcification. It can be seen that although the calcification has been fragmented by sectioning, it remains essentially complete. As discussed in the methods section, a few calcifications were extensively disrupted by the microtome blade. An example is shown in Figure 4-5. It can be seen that parts of the calcification have been lost. Angled flakes of calcified material can be seen casting shadows in the secondary electron (SE) image, and can be seen to obstruct the aluminium signal from the substrate. These calcifications with disrupted topography were generally characterised by a wider confidence interval for the median of measured composition.

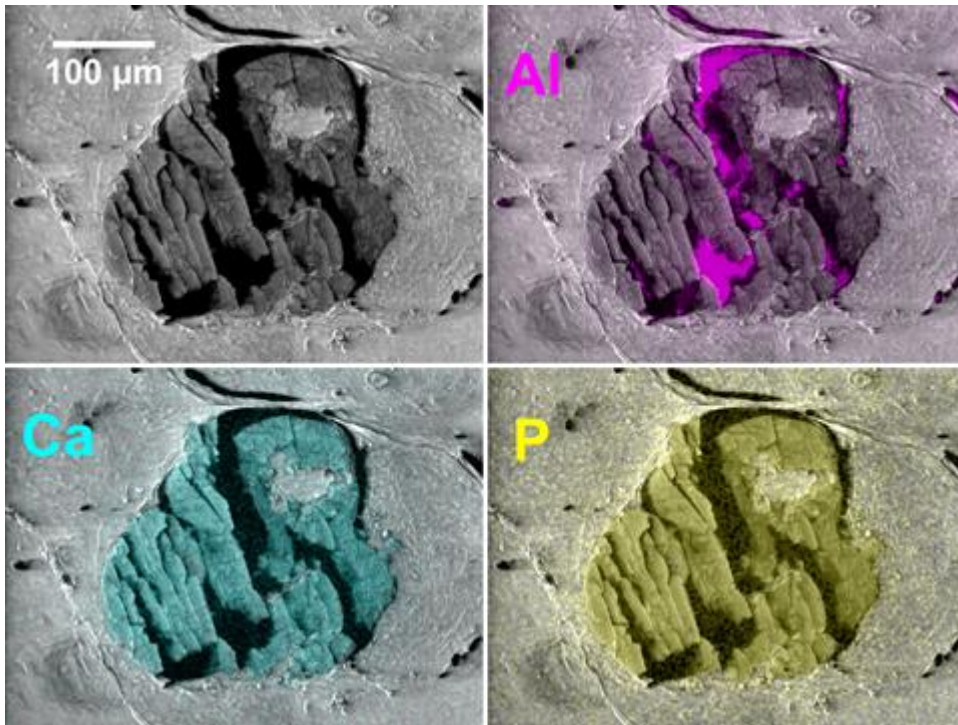


Figure 4-4 SEM image of a typical calcification overlaid with EDS elemental maps. The aluminium substrate can be seen through the cracks in the calcification resulting from sectioning.

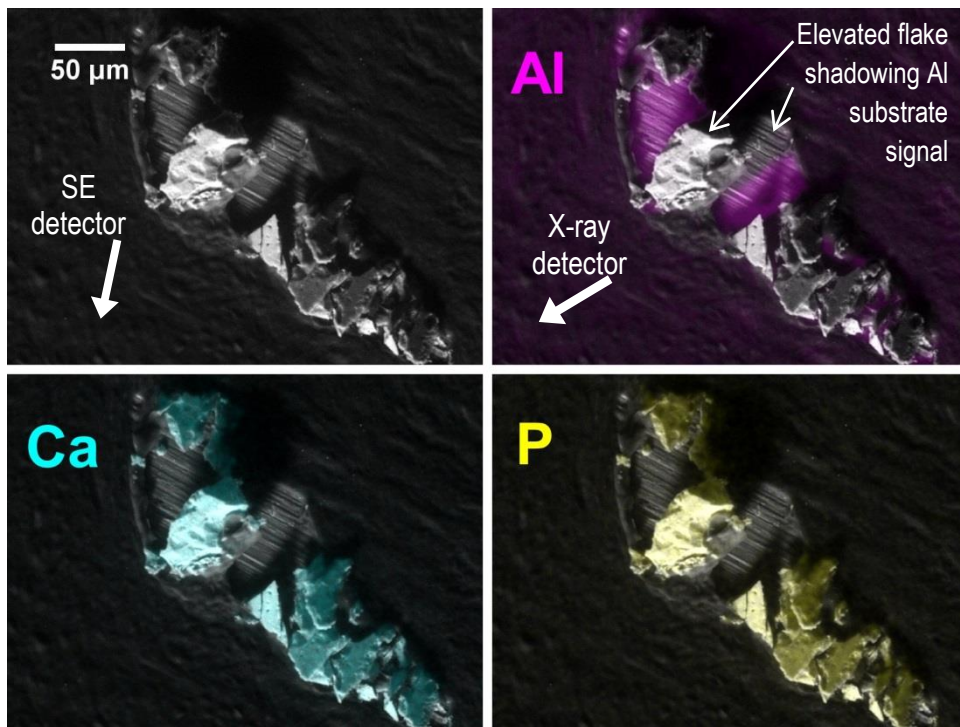
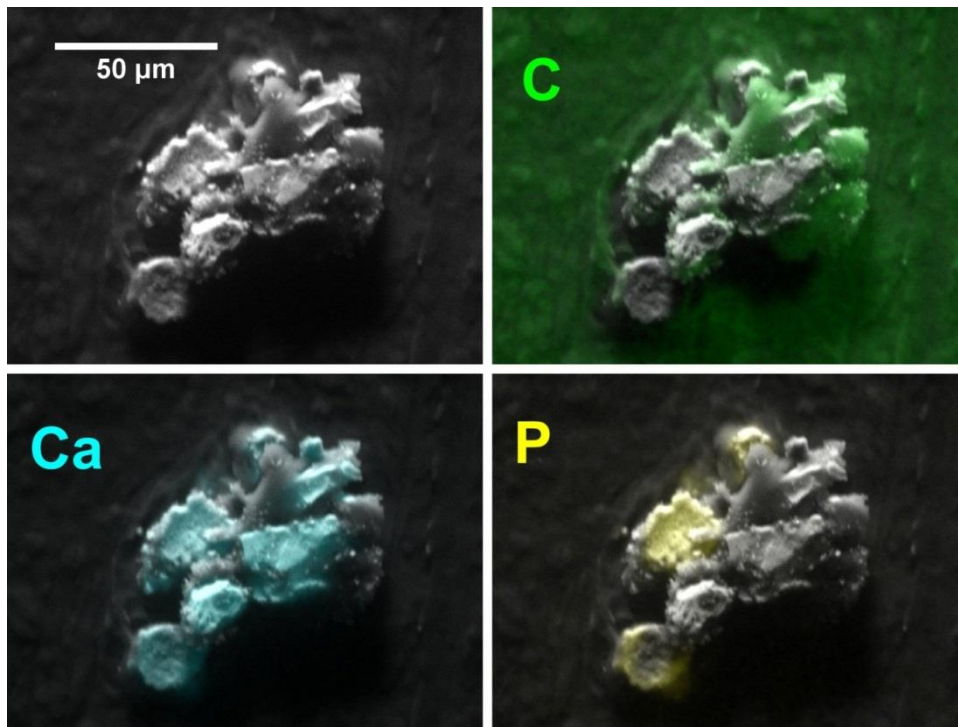


Figure 4-5 SEM image of a highly fragmented calcification. Note the shadowing of the substrate in the Al image.

#### 4.4.2 Calcium Phosphorus Ratio

All but one of the calcifications had a measured atomic Ca:P ratio in the range of 1.54 to 1.92, with a mean and median of 1.70. The one Ca:P outlier consisted of a small (~Ø70µm) calcification in an invasive specimen, in which the Ca:P measurements fell into two very distinct groups: 15 point measurements had a measured Ca:P ratio >100, and 12 measurements had a Ca:P ratio in the normal range (median 1.78). The normal and low-phosphorus measurements were in discrete areas, as shown by the calcium and phosphorus maps in Figure 4-6. Although an isolated occurrence, the measurements from this calcification proved important in interpreting the results with minor elements.



**Figure 4-6 SEM image of a calcification with low phosphorus regions corresponding to a non-apatite phase.**

The relationship between pathology and the Ca:P ratio, averaged by calcification, is shown in Figure 4-7. The mean Ca:P ratio was 1.70, 1.69 and 1.70 for benign, *in-situ*, and invasive respectively. In addition, the apparent

difference in variance between pathology groups was not found to be significant (Brown-Forsythe test).

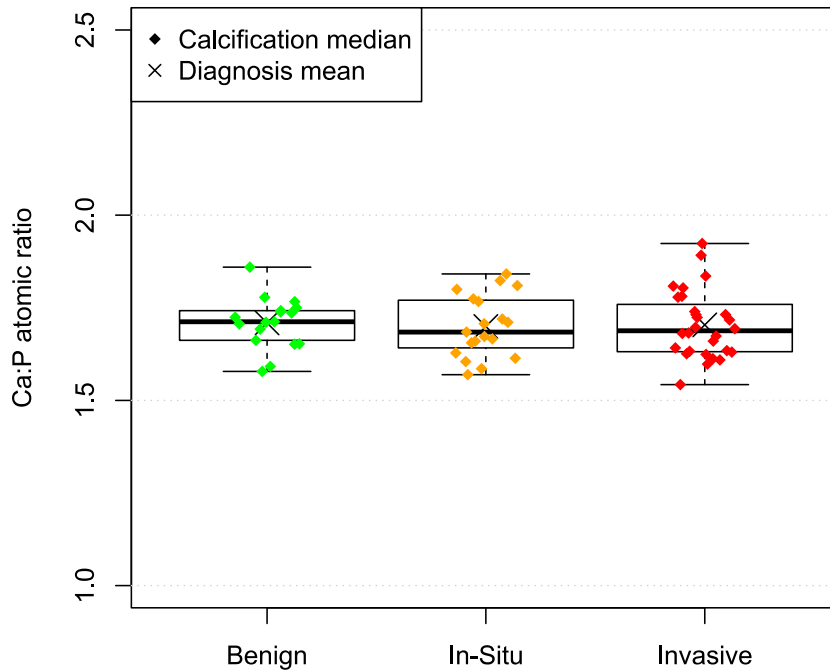


**Figure 4-7 A plot of median calcification Ca:P ratios vs. specimen diagnosis shows no significant variation of Ca:P ratio with specimen pathology.**

#### **4.4.3 Magnesium Calcium Ratio**

The mean Mg:Ca atomic ratio was calculated as 1.93% (95% confidence interval 1.70% - 2.11%). The relationship between pathology and the Mg:Ca ratio, averaged by calcification, is shown in Figure 4-8. Although 6 highest Mg:Ca levels out of 66 calcifications were all in specimens with an invasive diagnosis, there was no significant difference between the pathology groups.

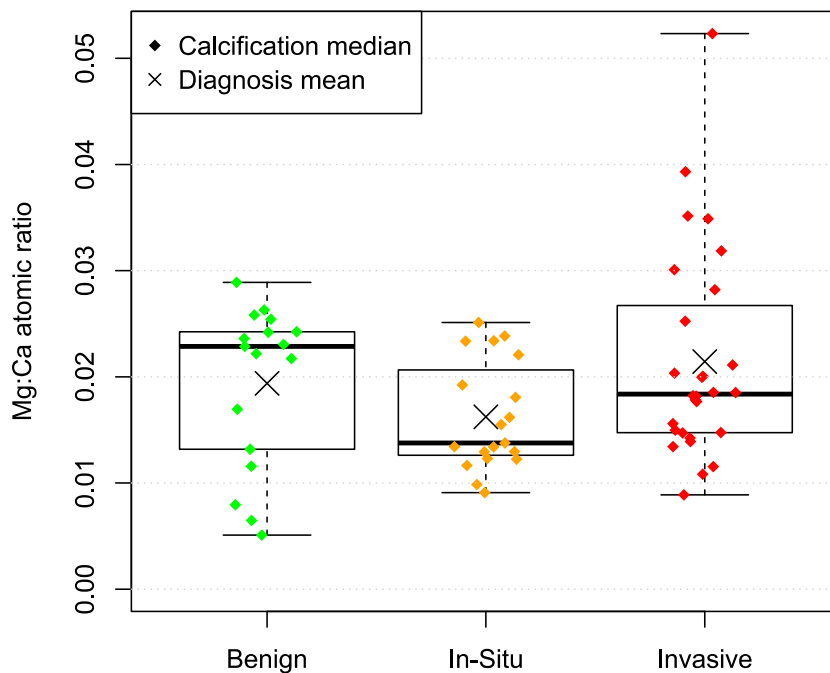


**Figure 4-8 A plot of median calcification Mg:Ca ratios vs. specimen diagnosis shows no significant variation of Mg:Ca ratio with specimen pathology.**

The single calcification with a very high Ca:P ratio showed a large difference in magnesium level between the low-P and high-P areas within the calcification. The 15 measurements from the low-P areas had a Mg:Ca ratio in the range 0.1% - 1.1% (mean 0.7%), whereas the 12 measurements from the high-P areas had a Mg:Ca ratio in the range 1.8% - 2.7% (mean 2.2%).

#### 4.4.4 Sodium Calcium Ratio

The relationship between pathology and the Na:Ca ratio, averaged by calcification, is shown in Figure 4-9. Unlike the other two elemental ratios, there is a highly significant difference between groups. Treating diagnosis as an ordinal variable, ranked benign < in-situ < invasive, the Na:Ca ratio is positively correlated with diagnosis ( $p < 0.001$  Kendall's tau-b ). With the measurements

aggregated to a mean specimen level, the significance of the correlation becomes  $p = 0.007$ . If diagnosis is treated as a binary variable, mean specimen sodium level is significantly lower in benign than malignant specimens ( $p = 0.007$  Mann-Whitney U).

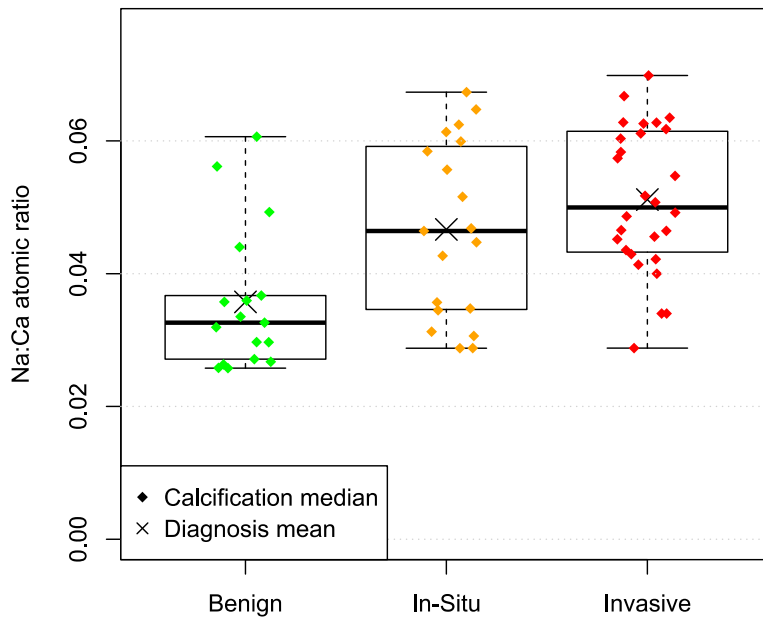


**Figure 4-9 The Na:Ca ratio of calcifications in specimens with a benign diagnosis is significantly lower than that in specimens categorised as malignant (*In-situ* or *Invasive*).**

Measurements of sodium levels need to be treated with caution. The specimens are immersed in saline solutions during fixation, hence at least some of the sodium present might not originate from the calcification. However, the single calcification with areas of low-phosphorus calcified material provides evidence that the sodium detected is intrinsic to the apatite phase. As with magnesium, the sodium measurements fell into two very distinct groups. The 15 measurements from the low-P areas had a low sodium content, with a Na:Ca ratio in the range 0.2% - 1.5% (mean 0.8%). In contrast, the 12 measurements



from the high-P areas had high Na:Ca ratio in the range 3.3% to 6.4% (mean 5.1%). This is shown in Figure 4-10.

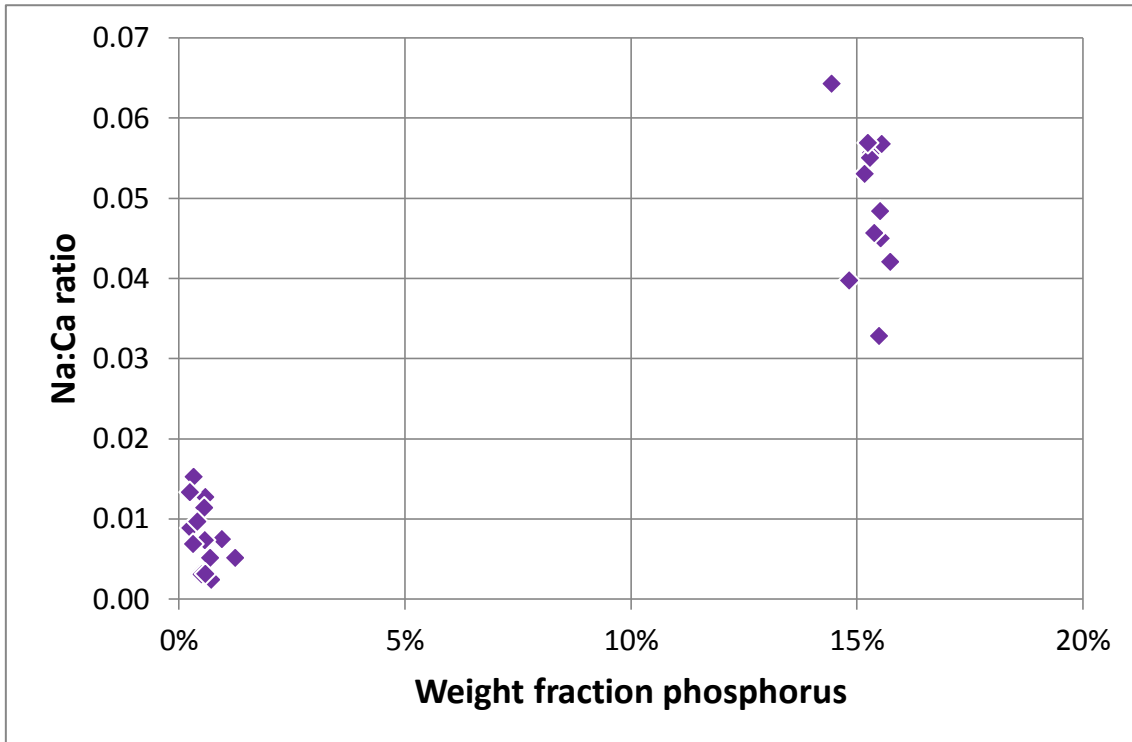


**Figure 4-10 Scatter plot showing that low-P areas in specimen S66 also have a low Na:Ca ratio**

As confirmation that this is not an artefact in which the signal from all low atomic number elements is suppressed in the low phosphorus areas, or that an inadequately corrected oxygen sum peak is masquerading as sodium, the mean weight percentage of oxygen was 49% and 48% in the low and high phosphorus regions respectively.

## 4.5 Discussion

The calcium to phosphorus ratio was of primary interest in this study, since if there were a substantial variation with pathology, it would open up the possibility of additional diagnostically useful information from mammography using energy discriminating detectors. However, the measured Ca:P ratio of calcifications found to lie in a narrow range (interquartile range 1.64 to 1.75), and no significant difference could be found between the pathology groups.

These results do not preclude the possibility that some diagnostically useful relationship may exist within a particular sub-type of calcifications, but the apparent lack of a general relationship limits the appeal of this approach.

In the one previous semi-quantitative study of Ca:P ratio in breast calcifications<sup>96</sup>, the overall mean molar Ca:P ratios for the three benign and two malignant specimens measured were 1.64 and 1.67 respectively (weight ratios 2.13 and 2.17), which is very similar to these results.

It has been suggested that the mechanisms involved in the formation of breast calcifications may be similar to those involved in the deposition of hydroxyapatite in bone; in particular, bone matrix proteins involved in osteoblast mineralisation are also expressed in mammary cells<sup>64</sup>. Measured values for Ca:P ratio in bone vary widely, and have recently been comprehensively reviewed.<sup>158</sup> The most relevant all-bone study cited is the ICRP-89 Reference Woman with a Ca:P atomic ratio of 1.63, and a compilation of studies on various bones gave a value of 1.68. These are very similar to the values found for breast calcifications in this study. Calcifications appear to be similar to bone in Ca:P ratio as well as in crystallographic parameters.

The low phosphorus areas in one calcification must consist of a non-apatite phase. The most likely contender is calcium oxalate, though without evidence from x-ray diffraction and/or vibrational spectroscopy, this cannot be confirmed. Although most calcium oxalate crystals have been reported in association with benign lesions, they have also been observed in malignant cases, where they are presumed to be bystanders<sup>86</sup>. It is also notable that this instance occurs within a calcification which also contains regions of hydroxyapatite, whereas there are no previous reports of a mixed Type I/II calcification.

The apparent absence of a relationship between magnesium content and pathology in these specimens is surprising in the light of the previous study showing increased magnesium in malignant specimens<sup>63</sup>, and the known avidity of tumour cells for Mg<sup>151,152</sup>. One possible reason for the lack of a relationship in these specimens is the leaching of crystal-surface or hydration-layer

magnesium, either *in-vivo* or during histological processing. This is discussed in detail in Chapter 5.

One of the most interesting and potentially useful observations in this study is the presence significantly higher sodium levels in calcifications within malignant specimens. This is consistent with the observation that total tissue sodium levels are elevated within breast tumours<sup>159,160</sup>. Sodium readily substitutes for calcium in hydroxyapatite, and the level of substitution is likely to reflect the tissue sodium concentration at the time of apatite precipitation. It appears that this difference survives histological processing, due to the fact that the sodium is substituted within the apatite lattice. If it can be confirmed that all calcifications arising from malignant changes display elevated sodium levels, this has potential to indicate malignancy in the vicinity of a needle biopsy specimen, even if malignant cells are not contained within the core.

## 5 Crystallographic Parameters

### 5.1 Aims

Measurement of the elemental constituents of breast calcifications in the previous chapter only provides a limited insight into their composition. Biological calcified materials can present in a wide range of crystallographic phases. Moreover, the crystallite dimensions and lattice parameters of any the phases may also vary with pathology. The aim of this stage of the research was therefore to measure the phase composition and crystallographic properties of the calcifications using x-ray diffraction, and relate this to both diagnosis and elemental composition, in order to obtain a more rounded understanding of calcification composition.

Most of the content of this chapter has previously been published<sup>161</sup>.

### 5.2 Introduction

To date, X-ray diffraction of breast calcifications has been limited to a qualitative identification of major phases present in small numbers of samples. There have been no quantitative investigations of crystal lattice parameters and peak broadening, which provide information concerning ionic substitutions and crystallographic disorder respectively. Moreover, investigations to date have relied on dissection of calcifications from bulk tissue specimens. Any analysis relying on fresh tissue is hampered by the difficulty of accessing a wide range of specimens. In contrast, diagnostic archives represent a rich source of material with varying pathology, and histological sections cut from archive blocks are readily available.

It is technically challenging to acquire spatially-resolved X-ray diffraction data of sufficient quality for quantitative analysis from the very small volumes of poorly crystalline material present in these histological sections. To the best of our knowledge, *in-situ* X-ray diffraction analysis on histological sections of any sort has only been reported twice before<sup>162,163</sup>, in studies of vascular calcifications; this is the first time such a technique has been used to study breast calcifications. The techniques developed could readily be used for investigation

of other pathological calcifications; similarities and differences may shed light on the mechanisms by which these are formed.

## **5.3 Materials and Methods**

### **5.3.1 Archive blocks**

Formalin Fixed Paraffin Embedded (FFPE) core biopsy breast specimens were selected from the Gloucestershire Hospitals NHS Foundation Trust diagnostic archive (under approval from Gloucestershire Local Research Ethics Committee). Blocks were randomly selected from the 2012 archive, subject to the presence of calcifications in the histopathology report, and an unambiguous classification of “B2 - Benign”, “B5a - Ductal Carcinoma *In-Situ*”, or “B5b - Invasive Carcinoma”<sup>22</sup>. For the purposes of analysis, specimens were also grouped as “Benign” (B2) vs. “Malignant” (B5a or B5b). A summary of the histopathology report for each of the specimens analysed is given in Appendix B. These were screened by mounting the blocks in a Nikon Metrology XT H225 CT system and imaging at 20 kV both perpendicular and parallel to the face of the block. Following screening, blocks were selected with significant levels of calcification at or near the cut surface. The selected blocks were then CT-scanned, and the reconstructed volumes processed as previously described<sup>115</sup> to identify the position of calcifications relative to the tissue outlines at the surface of the blocks.

### **5.3.2 Mounting**

As described in the previous chapter, three sequential microtome slices of 5 µm were cut from each block. The slice used in this analysis was mounted on 12.5µm thick polyolefin heat shrink film which was stretched taut over a 38mm diameter aluminium alloy ring, and held in place with an ‘O’ ring in a groove. The mounting method is depicted in Figure 5-1, and drawings of the fixture are in Appendix D.

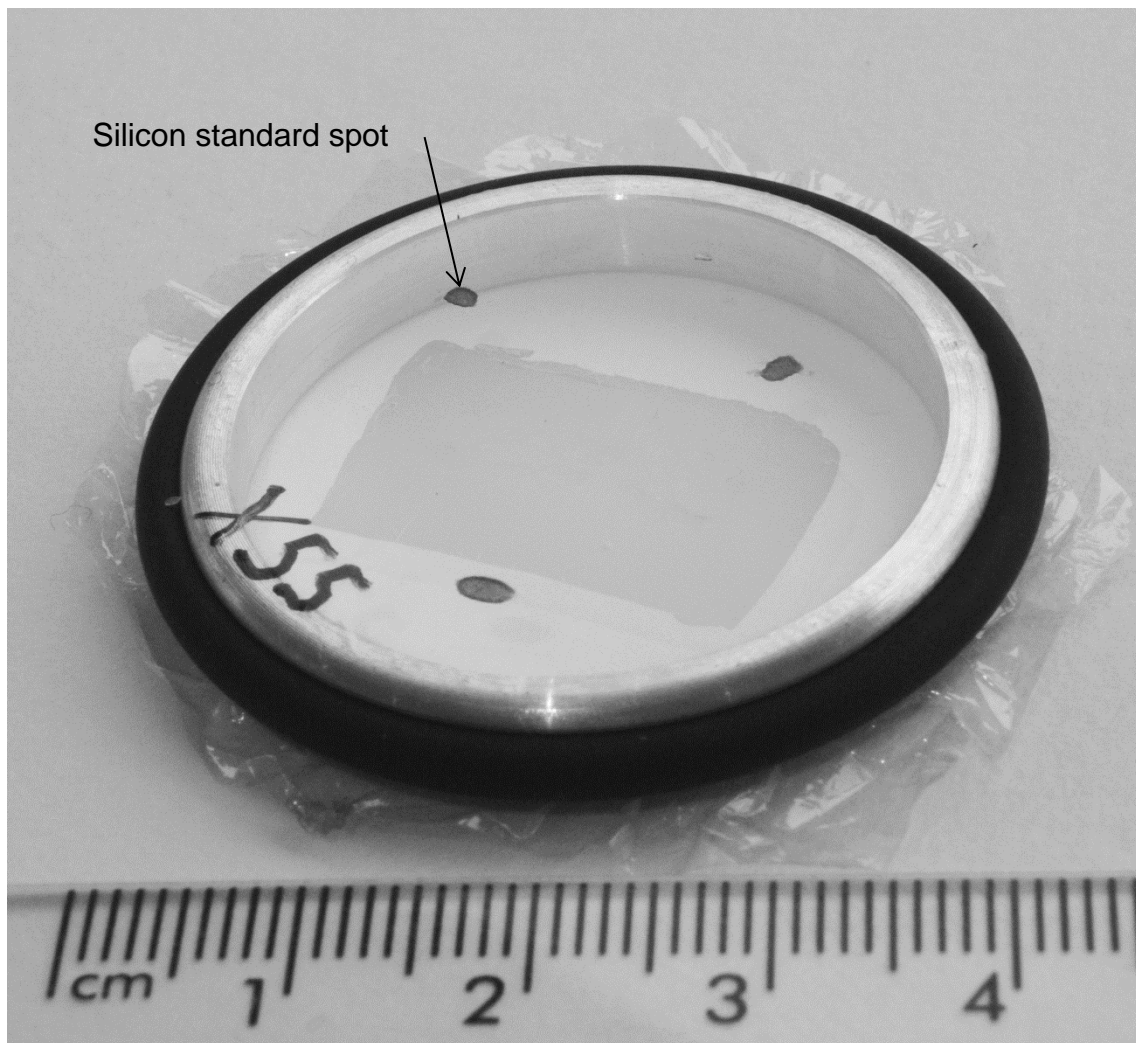


**Figure 5-1 – Tissue section mounted on polyolefin film stretched across an aluminium alloy ring, and held in place with a Viton rubber O-ring.**

Polyolefin heat-shrink film was chosen since it only exhibits weak diffraction lines, which are away from peaks of interest in candidate calcification phases. In addition, these lines are the same position as those from the paraffin embedding material.

NIST (National Institute of Standards & Technology) Standard Reference Material 640c Silicon Powder was used for calibration of sample-detector distance. A slurry was made with the standard powder in a dilute solution of PVA adhesive in distilled water, and three spots painted on the mounting film around and in the plane of the tissue section.

### 5.3.3 Beamline set-up

X-Ray diffraction experiments were conducted on beamline I18 at Diamond Light Source, Didcot, UK. Whilst in principle x-ray diffraction measurements could have been conducted using a laboratory source, synchrotron radiation offers substantial advantages for this type of research. Firstly, the high brilliance possible with synchrotron radiation enables measurements to be made on particles such as breast calcifications, substantially quicker than even a high brightness laboratory source. Secondly, instrumental broadening is typically insignificant relative to sample broadening in this type of specimen when using synchrotron diffraction, which minimises a potential confounder when performing peak broadening analysis. Thirdly, we wished to investigate the variation in characteristics within individual calcifications, which requires a spatial resolution which is only realistically achievable with a microfocus synchrotron source.

The aluminium sample rings were clamped perpendicular to the beam on a motorised stage. Measurements were made in transmission using a Photonic Science X-ray sCMOS camera. A video microscope was mounted at 45° to the beam and used to position the desired point on the tissue section in the beam. A beam spot size of 10x10 µm was used, with an energy of 10.0 keV. The specimen to detector distance was kept constant by ensuring the centre of the microscope field of view was in focus at maximum magnification. This was confirmed by measurements on each of the three silicon standard dots on every specimen. Calcifications were located using the video microscope, by reference to the visible tissue outlines and the maps created from the CT measurements. Measurements were made on typically 11 equally spaced positions in a vertical line from the bottom to the top of each calcification. Exposure was for 30 seconds per measurement. Data acquisition was performed using the Diamond Generic Data Acquisition (GDA) software, with images and ancillary data saved in NeXus data file format. A total of 548 diffractograms were collected from 56 discrete calcifications in 15 specimens, consisting of 5 benign, 4 *in-situ*, and 6 invasive. In addition diffractograms were collected for the silicon standards surrounding the specimens. These sample

sizes are sufficient to achieve significant group differences using non-parametric testing.

#### **5.3.4 Analysis**

Azimuthal integration of the 2D diffraction images to 1D patterns was conducted using DAWN (Data Analysis WorkbeNch) software <sup>164</sup>. The silicon standard images were used for calibration of beam centre, detector tilt, and sample-detector distance.

Diffraction patterns exhibited a large background to signal ratio, and it was found beneficial to subtract the background as a separate step prior to pattern fitting. The background was subtracted in R <sup>165</sup> using the Peak Filling method <sup>166</sup>, with the background centred in the noise band. Following background subtraction, pattern fitting was conducted using TOPAS 4.2 software (BRUKER AXS, Inc.).

The whitlockite diffraction spots were separated from the continuous hydroxyapatite rings by cake-remapping in DAWN, followed by azimuthal background subtraction and azimuthal integration at each  $2\theta$  value in R. This is similar to a method recently proposed for detection of abnormal grain growth in metals <sup>167</sup>. The whitlockite spots can be seen on a cake remapped diffraction image in Figure 5-2.



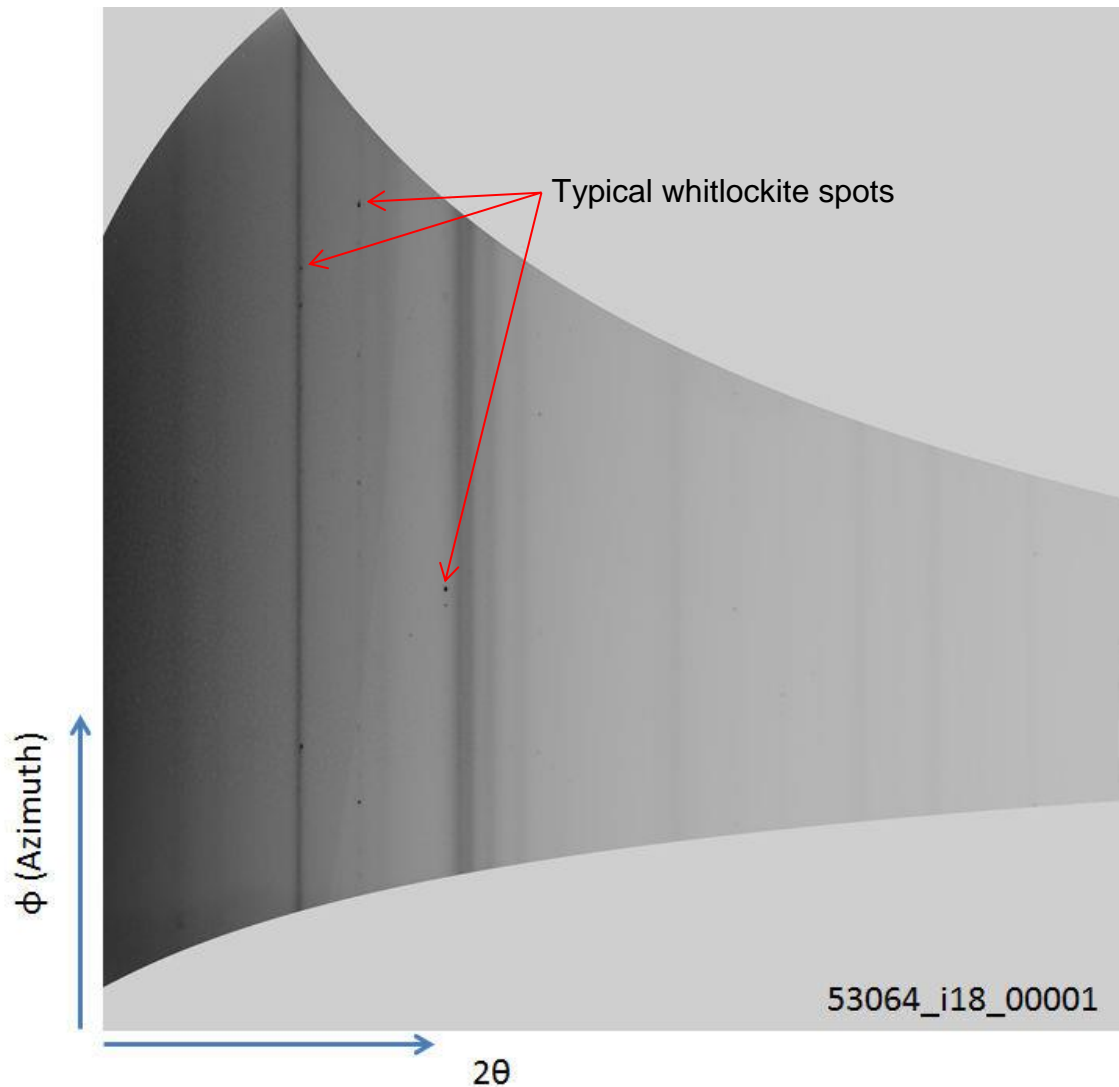


**Figure 5-2 Cake remapped diffraction image showing whitlockite spots.**

The average percentage of whitlockite was calculated for each specimen from the total area of the two strongest whitlockite peaks, (0 2 10) and (2 2 0) at  $2\theta \approx 25.05^\circ$  and  $27.8^\circ$  respectively, and from the total area of the overlapping (2 1 1), (1 1 2), (3 0 0), and (2 0 2) hydroxyapatite peaks which lie in between. Those areas were converted to weight percent using Reference Intensity Ratios of Hydroxyapatite and whitlockite from the ICDD PDF-2 database<sup>168</sup>. However, it should be noted that the small number of whitlockite crystallites in a favourable orientation in each diffractogram will lead to inaccuracies in the relative area of each peak in the pattern.

The hydroxyapatite crystalline domain size was calculated from the fitted FWHM of the (002), (102), (210), (211), (112), (300), (202), (310), (222), (312), (213) peaks. Decomposition of the heavily overlapped (211), (112), (300), (202) peaks was conducted in R. This involved a least squares fit using fixed peak positions which were calculated for each diffractogram from the 'a' and 'c' lattice parameters from the whole pattern fit. This gave a good fit for both broad and narrow peaks, as shown for illustrative purposes in Figure 5-3.

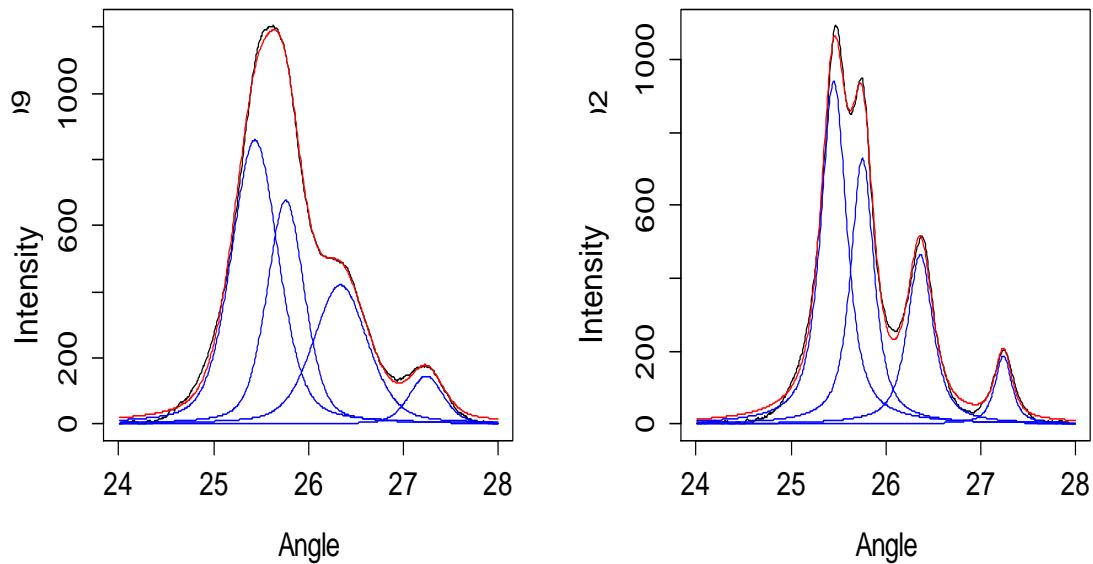


**Figure 5-3 Peak fitting using fixed component peak positions but unconstrained height and width gives a good fit to the major composite HA peak for both broad and narrow peaks.**

As is typical of synchrotron measurements on this type of material, instrumental broadening was negligible relative to the broad diffraction peaks, and was neglected. All FWHM measurements were converted to Integral Breadth using the Lorentzian mixing factor of the fitted pseudo-Voigt peaks, using the formula<sup>169</sup>:

$$\beta = \frac{\pi \cdot H / 2}{\eta + (1 - \eta) \sqrt{\pi \cdot \ln 2}}$$

Where  $\beta$  = Integral Breadth,  $H$  = FWHM,  $\eta$  = Lorentzian mixing factor

Integral breadth measurements were aggregated at specimen level as a weighted mean, using total area of the overlapped (211), (112), (300), (202) peaks as a weight.

The apparent coherent domain thickness can be approximated using the Scherrer formula:

$$\tau = \frac{K \cdot \lambda}{\beta \cdot \cos \theta}$$

$\tau$  = apparent coherent domain thickness,  $\lambda$  = x-ray wavelength,  $K$  = shape factor

$K$  depends on the shape of the crystallite, and is frequently given the value 0.9 based on an approximation of a spherical crystallite shape. In the case of anisotropic crystallites, as in these specimens,  $K$  varies with the direction of the diffraction vector. To address this, the Scherrer formula can also be written as<sup>170,171</sup>:

$$\varepsilon = \frac{\lambda}{\beta \cdot \cos \theta}$$

Where  $\varepsilon$  = volume-weighted domain size in the direction parallel to the diffraction vector. The value of  $\varepsilon$  can be calculated as a function of crystallite dimensions and diffraction vector angle for a range of crystallite shapes. For a cylindrical shape<sup>172</sup>:

Where  $0 \leq \varphi_z \leq \Phi$  :

$$\varepsilon = \frac{D}{\pi} \csc(\varphi_z) \left[ \frac{8}{3} + 2q \cdot \cos^{-1}(q) - \frac{1}{2q} \sin^{-1}(q) - \frac{5}{2}(1 - q^2)^{1/2} + \frac{1}{3}(1 - q^2)^{3/2} \right]$$

Or where  $\leq \varphi_z \leq \frac{\pi}{2}$  :

$$\varepsilon = D \csc(\varphi_z) \left[ \frac{8}{3\pi} - \frac{1}{4q} \right]$$

$D$  = diameter,  $H$  = height,  $q = H \cdot \tan(\varphi_z) / D$  and  $\Phi = \tan^{-1}(D/H)$

$\varphi_z$  = angle between reflection normal and cylinder axis

The apparent coherent domain size  $\epsilon$  was plotted as the radial dimension in a polar plot against the angle of the reflecting plane normal to the crystallographic 'c' axis. A least squares fit line from the cylindrical model was fitted to the data points by adjusting D and H, and the best-fit cylinder length and diameter from the model used as the dimensions of the coherently diffracting crystallite domains. Values of length and diameter were calculated from the weighted average integral breadth measurements aggregated by specimen. For illustration of the method, best fit lines for the average for all specimens, broken down by diagnosis, are shown in Figure 5-4

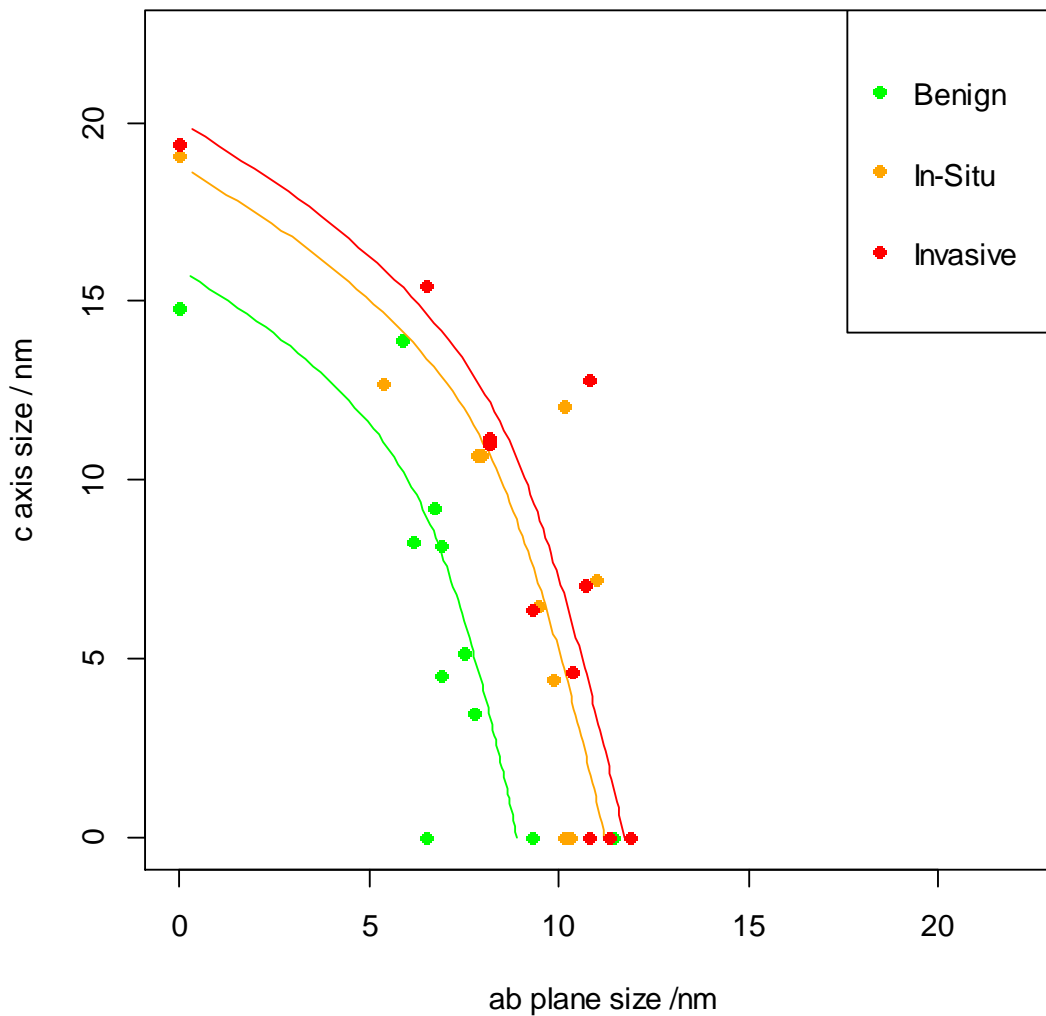


**Figure 5-4 All-specimen average coherent domain thickness for each crystallographic reflection with Langford cylindrical model lines of best fit.**

Inhomogeneous lattice strain from ionic substitution undoubtedly also contributes to peak broadening, and in theory it is possible to separate this from physical size effects by Williamson-Hall or Warren-Averbach methods. However, this is complicated by the fact that peak broadening in this case is markedly anisotropic, and the separation of anisotropic strain from anisotropic size effects requires data quality that is difficult to achieve with biological apatite. As a result of this, and other unaccounted sources of peak broadening, the calculated size of the coherently diffracting crystallite domains is bound to be smaller than the physical size of the crystallites. Indeed, it has been suggested that bone mineral is better described as paracrystalline, with a continuum of overlapping domains rather than crystallites with definite crystal boundaries<sup>173</sup>. Using coherently diffracting domain size, uncorrected for inhomogeneous strain, ensures comparability with the majority of studies on bone.

## **5.4 Results**

### **5.4.1 Phase composition**

The predominant phase in these calcifications is nanocrystalline hydroxyapatite. This is clear from Figure 5-5, which shows a normalised sum of all background subtracted diffractograms, overlaid with the theoretical peak positions for hydroxyapatite<sup>174</sup>. These peak positions and intensities are tabulated in Appendix C.

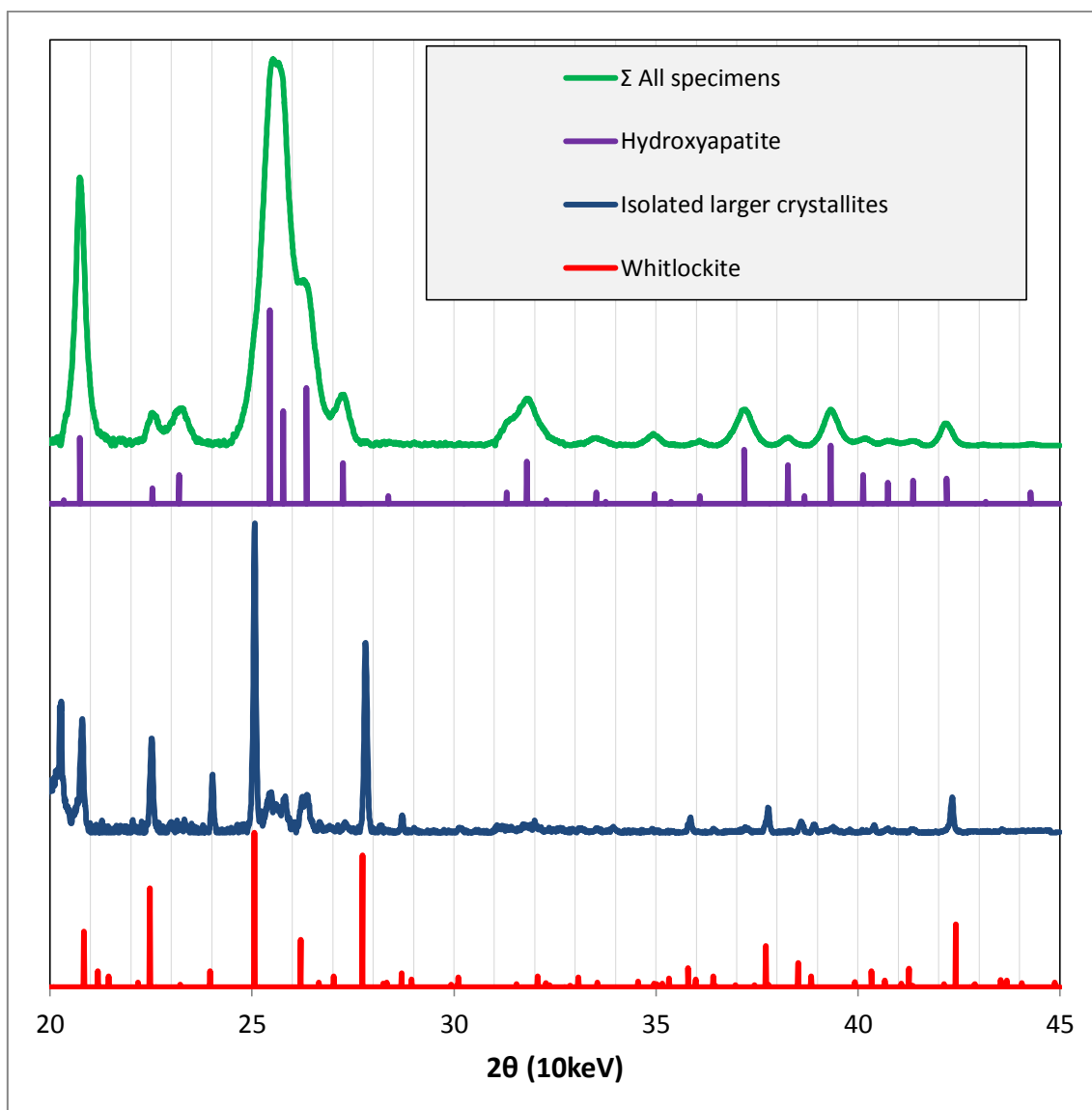


**Figure 5-5 All-specimens sum diffractogram and digitally isolated large crystallite diffractogram vs. theoretical line positions and intensities.**

In addition to the continuous Debye-Scherrer rings corresponding to hydroxyapatite, discrete diffraction spots were also observed in the 2-D scattering patterns, indicating the presence of a minor phase with substantially larger crystallites than the nanocrystalline hydroxyapatite major phase. These diffraction spots were separated from the continuous hydroxyapatite diffraction rings, as described in the methods section, and the integrated diffractograms (Figure 5-5) confirm that this crystalline phase is whitlockite (a magnesium substituted calcium orthophosphate with a beta-tricalcium phosphate structure).

The relationship between pathology and the percentage of whitlockite within the calcifications, averaged by specimen, is shown in Figure 5-6. With diagnosis treated as an ordinal variable ranked “benign” < “*in-situ*” < “invasive”, the percentage of whitlockite per specimen is positively correlated with diagnosis ( $p= 0.008$  Kendall’s tau-b), i.e. the benign specimens contain the least whitlockite and the invasive specimens contain the most.

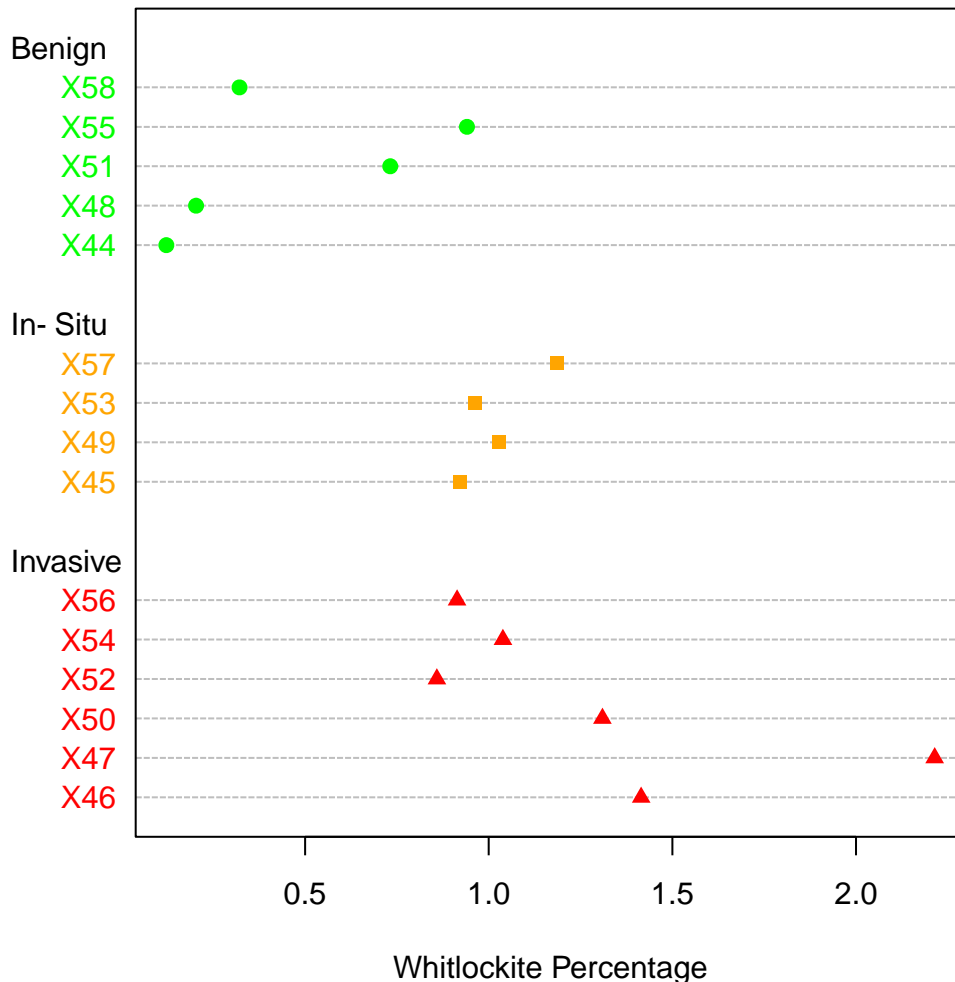


**Figure 5-6 Whitlockite weight percentage average per specimen, grouped by diagnosis. Malignant specimens contain significantly more whitlockite than those with a benign diagnosis. Individual specimen details are available in Appendix B.**

No evidence could be found of other crystalline phases. In particular, the scatter angle region from 29° to 30° was examined for evidence of weddellite (calcium oxalate dihydrate) and brushite (calcium hydrogen phosphate

dihydrate), since this region is well separated from hydroxyapatite and whitlockite peaks and contains two major (> 10%) peaks each for weddellite and brushite. Figure 5-7 shows the maximum intensity over all 548 diffractograms, no peaks could be observed corresponding to these two phases.

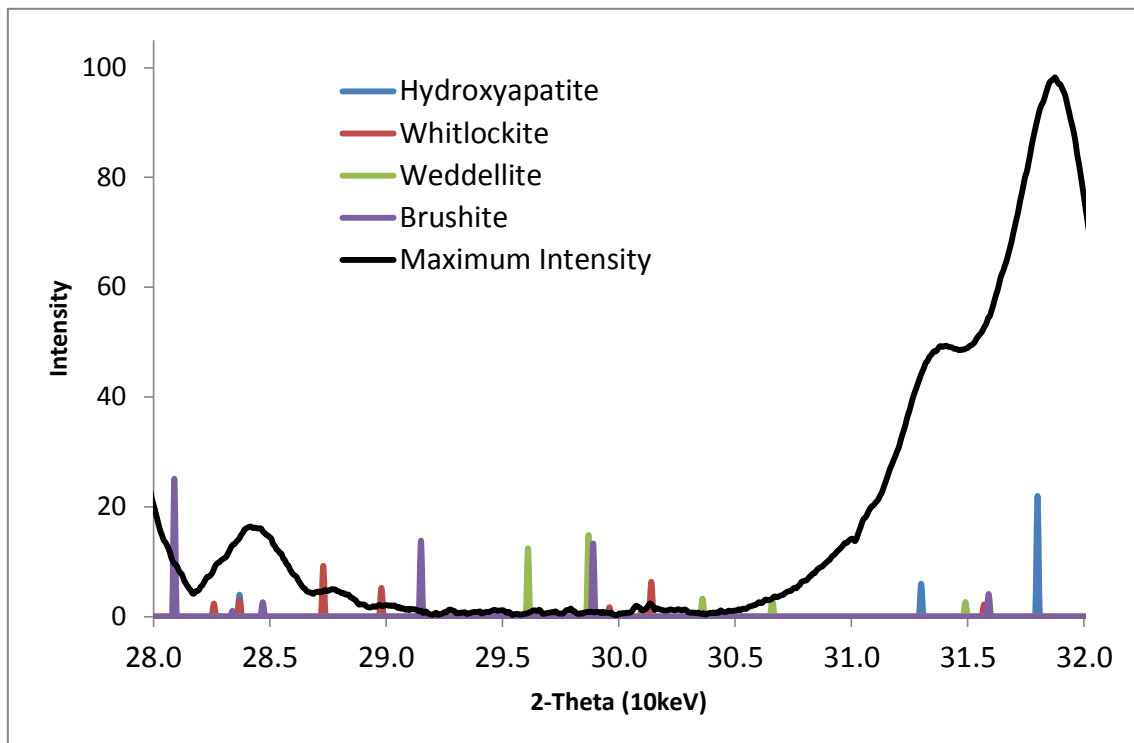


**Figure 5-7** The maximum intensity line shows no evidence of any of the four peaks corresponding to brushite or weddellite which lie between 29° and 30°.

#### 5.4.2 Hydroxyapatite analysis

Analysis of positions and widths of the intensity maxima in the diffraction pattern gives some insight into both the ionic substitutions in the crystal lattice and the size of the crystallites.

The hydroxyapatite crystalline domain dimensions were calculated from the fitted peak widths as described in the methods section, and are plotted in Figure 5-8. With the diagnosis treated as an ordinal variable ranked “benign” < “*in-situ*” < “invasive”, the specimen mean crystallite domain ‘c’ axis length and ‘ab’ plane domain size both showed a positive correlation with diagnosis ( $p=0.034$  and



p=0.011 respectively, Kendall's tau-b). With diagnosis treated as a binary variable, malignant specimens had larger 'c' axis length and 'ab' plane domain size than benign specimens (p=0.040 and p=0.005 respectively, Mann Whitney U).

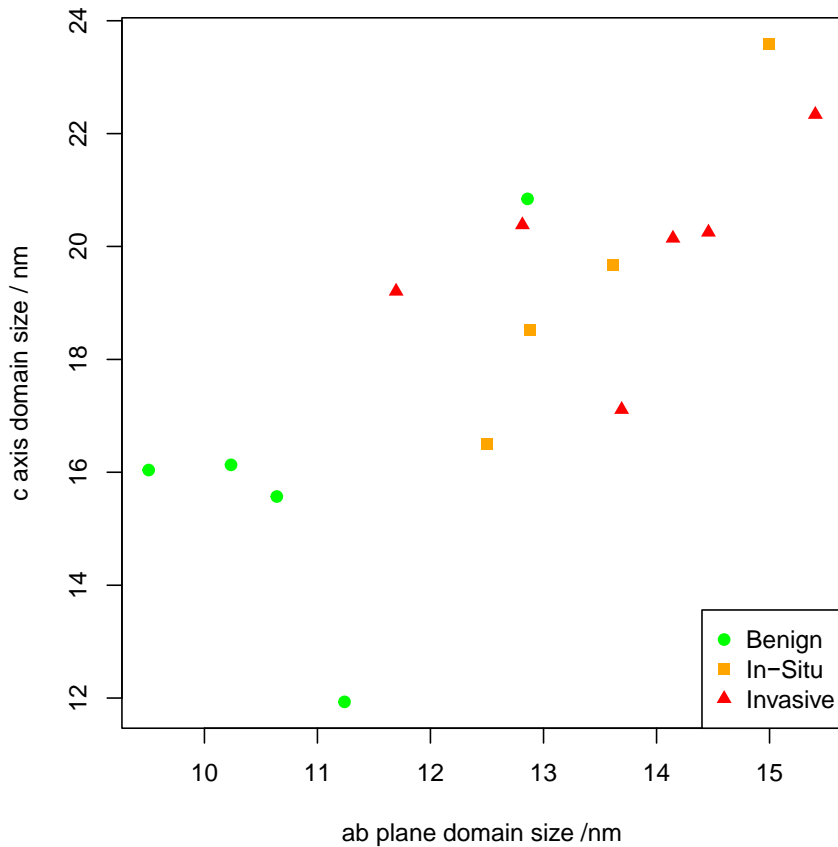


**Figure 5-8 Hydroxyapatite crystalline domain dimensions, averaged by specimen and categorised by diagnosis. Malignant specimens have significantly larger crystalline domain size in both axes than benign specimens.**

The calculated 'a' and 'c' lattice parameters of the hydroxyapatite phase, averaged by specimen, are plotted in Figure 5-9. There is a negative correlation, with a slope of 'a' vs. 'c' of -1.46 (95% confidence interval -1.87 to -1.05). With the diagnosis treated as an ordinal variable, as in the domain size analysis, the mean specimen 'c' lattice parameter showed a positive correlation with diagnosis (p=0.025, Kendall's tau-b). Using a binary analysis, the 'c' lattice

parameter is larger in malignant specimens than in benign ( $p= 0.019$ , Mann Whitney U). The correlation between 'a' lattice parameter and diagnosis was not significant.

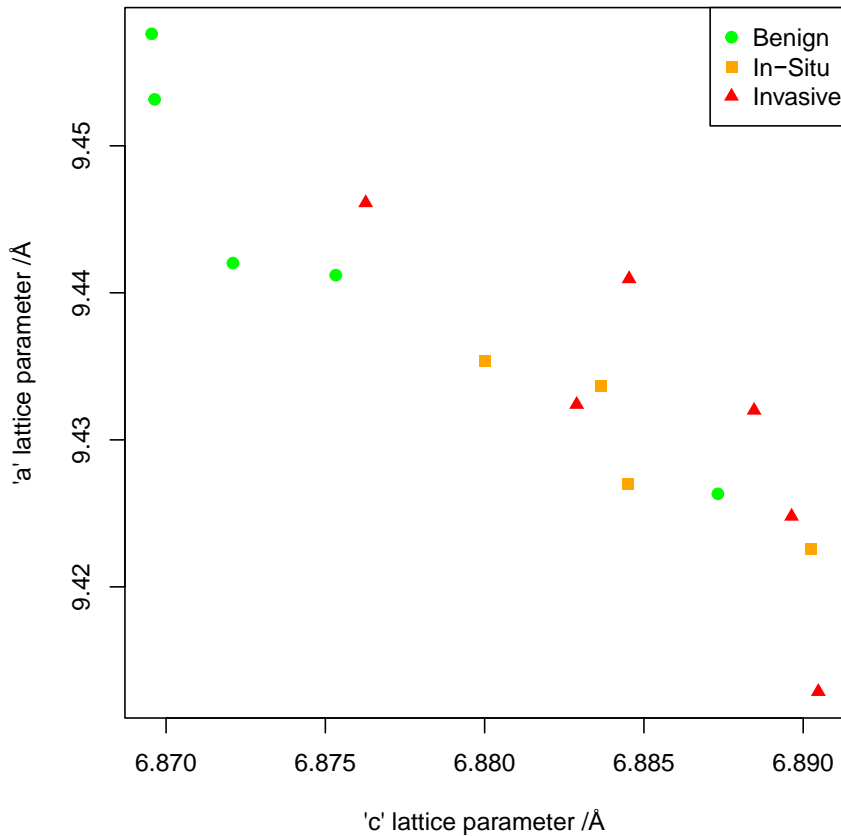


**Figure 5-9 Hydroxyapatite lattice parameters, averaged by specimen and categorised by diagnosis. There is a significant negative correlation between 'a' and 'c' lattice parameters, and the 'c' lattice parameter is significantly smaller in benign than in malignant specimens.**

### 5.4.3 Spatial variation

Since the measurements were taken in uniformly spaced lines across each calcification, the position of each measurement in the sequence can be used to calculate an approximate proportion of the distance from the centre to the edge. The 002 FWHM (Full Width Half Maximum) of each measurement was normalised to the mean FWHM for that calcification, and plotted against position

in Figure 5-10. The variation from the centre to the periphery was calculated by linear regression, and the regression line for each diagnosis plotted. On average the 002 FWHM is 5.4% (2.6% - 8.2%) greater at the edge than the centre ( $p < 0.001$ ). This trend is very similar for benign, *in-situ*, and invasive specimens. This indicates that the coherent domain size in the 'c' axis direction is larger at the centre of the calcifications than at the surface.

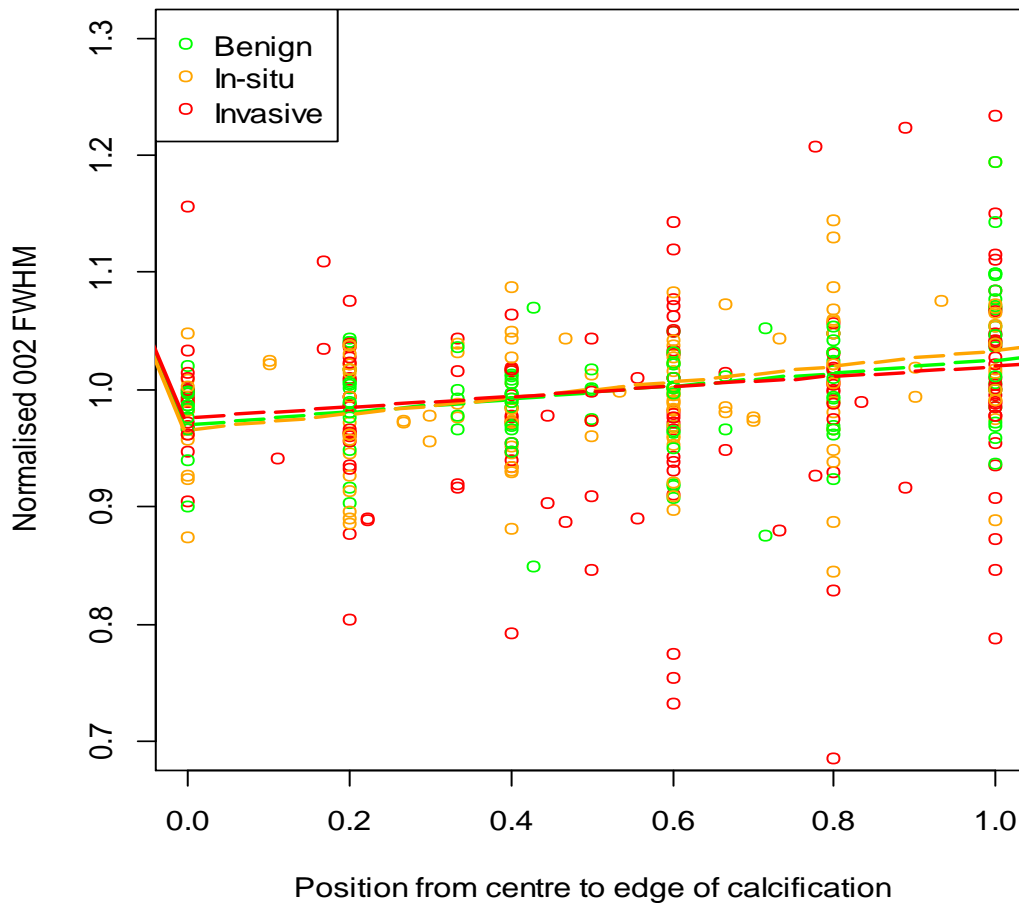


**Figure 5-10** The spatial variation of (002) FWHM shows that the domain size is larger at the centre of the calcifications than at the surface.

#### 5.4.4 Correlation with elemental composition

The crystallographic parameters measured were compared to the three elemental ratios reported in Chapter 4, in the 39 calcifications for which both sets of measurements were available. These are shown in Table 5-1.

EDS Measurement	XRD measurement	Coefficient	Adjusted R <sup>2</sup>	p-value	Adjusted p-value
Mg:Ca ratio	Whitlockite %	-35.6	0.183	0.004	<b>0.034</b>
	Domain Diameter	-125	0.165	0.007	<b>0.046</b>
	'c' / 'a' lattice parameter ratio	-0.105	0.279	< 0.001	<b>0.003</b>
Ca:P Ratio	Whitlockite %	2.73	0.098	0.032	0.158
	Domain Diameter	-0.0555	-0.028	0.991	1.000
	'c' / 'a' lattice parameter ratio	0.00231	-0.012	0.459	1.000
Na:Ca Ratio	Whitlockite %	-1.29	-0.027	0.871	1.000
	Domain Diameter	63.1	0.107	0.026	0.154
	'c' / 'a' lattice parameter ratio	0.0366	0.071	0.056	0.222

**Table 5-1 Correlation of elemental ratios measured in this study, with X-ray diffraction measurements made on the same 39 calcifications.**

The lattice parameter 'c' / 'a' ratio was used since the 'a' and 'c' parameters are strongly negatively correlated in these specimens. Linear regression was conducted with XRD measurements as a function of EDS measurements. The p-value for a correlation was adjusted to control the familywise error rate for multiple comparisons using the Holm–Bonferroni method. After adjustment, the only significant correlations between crystallographic parameters and composition relate to the magnesium calcium ratio. Although the correlations are all weak, domain size, c/a lattice parameter ratio and whitlockite percentage were all significantly negatively correlated with magnesium concentration.

## **5.5 Discussion**

### **5.5.1 Major phases**

The presence of calcifications consisting predominantly of nanocrystalline hydroxyapatite is unsurprising and concurs with previous X-ray diffraction characterisations. Perhaps more surprisingly, no “Type I” calcium oxalate weddellite calcifications were observed in any of 56 calcifications analysed. In addition, no calcium oxalate was found in 236 calcifications from 110 patients in an FTIR study of samples taken from the same archive <sup>109</sup>. Other studies have reported a widely varying proportion of calcium oxalate calcifications in biopsy tissue (e.g. 0.4%<sup>76</sup>, 7.3%<sup>77</sup>, 17.3%<sup>80</sup>, 28.8%<sup>63</sup>). Although the specimen numbers in this pilot study were small, the absence of calcium oxalate in these results suggests a proportion towards the lower end of this range.

### **5.5.2 Whitlockite**

The presence of whitlockite in these specimens is a novel finding. It has occasionally been reported in other pathological calcifications, including prostate <sup>175</sup>, aorta <sup>176</sup>, cartilage <sup>177</sup>, and salivary glands <sup>178</sup>. A cursory mention of a single FTIR observation in a breast calcification with an absorption band at 990 cm<sup>-1</sup> consistent with the presence of whitlockite was reported previously <sup>179</sup>. Our study is therefore the first to make a positive confirmation of whitlockite in breast calcifications.

The occurrence of whitlockite implies the presence of magnesium, with the least whitlockite in benign specimens, and the most in invasive carcinoma. The negative correlation between whitlockite fraction and Mg:Ca ratio shown in Table 5-1 is therefore initially rather surprising. This can be explained from the nature of magnesium within calcified tissue. Magnesium in bone resides largely on the crystal surface<sup>180,181</sup> or hydration layer<sup>182,183</sup> rather than within the apatite lattice. Apatite has been shown to be capable of only very limited magnesium substitution under physiological conditions<sup>184</sup>. Much of the magnesium in calcified tissue can therefore exchange rapidly, and forms the main reservoir for buffering extracellular magnesium in the body<sup>185,186</sup>. Extracellular levels of magnesium have been observed to be, on average, lower than normal in breast cancer<sup>148</sup>. Even if a calcification initially forms with high levels of magnesium, due to high intracellular levels, magnesium associated with hydroxyapatite could rapidly decrease towards the lower levels present in the extracellular environment. This is particularly likely given the high surface area to volume ratio of a particle the size of a breast calcification. It is also conceivable that at least some labile magnesium could leach from calcifications within the specimen through immersion during fixation and histological processing.

In contrast to the apatite phase, the magnesium in whitlockite forms an essential stabilising element of the crystal lattice<sup>187,188</sup>. The presence of whitlockite is therefore an indicator of the local magnesium concentration at the time of mineralisation, rather than the time of sampling<sup>162</sup>. In precipitation experiments where there are both carbonate and magnesium ions in solution, it has also been observed that lower pH leads to less magnesium incorporation into the apatite lattice for a given magnesium concentration in the solution<sup>189</sup>. Furthermore, at lower pH, the appearance of whitlockite occurs at lower magnesium concentrations<sup>189</sup>. The pH is, on average, likely to be lower in malignant specimens than benign, thus inhibiting incorporation of magnesium into the apatite lattice, and instead favouring whitlockite formation. This offers an explanation for the increased whitlockite fraction in malignant specimens. The reported high intracellular<sup>151</sup> vs. low extracellular<sup>148</sup> levels of magnesium in

breast cancer would resolve the apparent contradiction that whitlockite percentage appears to be negatively correlated with magnesium content.

Note that high intracellular levels of magnesium could still explain the low levels of carbonate observed in calcifications associated with tumours, as previously suggested<sup>161</sup>, since the carbonate level within the apatite lattice is influenced by the magnesium concentration at the time of crystallisation.

### 5.5.3 Precursor phases

Both brushite and octacalcium phosphate (OCP) have been identified as precursors to the formation of hydroxyapatite in mineralised tissue, particularly in an acidic environment<sup>190</sup>, which is typical of the microenvironment of solid tumours<sup>191</sup>. No brushite was observed in these specimens. OCP could not be distinguished from hydroxyapatite by X-ray diffraction in this study, since the patterns are nearly identical over the diffraction angular range captured. The most prominent differentiating sign is the strong low angle OCP (1 0 0) peak with a d-spacing of 19.7 Å, which does not occur in hydroxyapatite. However, this diffraction peak occurs considerably below the lowest angle collected in this study, and would require a different experimental setup to detect. The presence of OCP cannot therefore be confirmed or ruled out in these specimens.

### 5.5.4 Comparison with maturing bone

It has been suggested that the mechanisms involved in the formation of breast calcifications may be similar to those involved in the deposition of hydroxyapatite in bone; in particular, bone matrix proteins involved in osteoblast mineralisation are also expressed in mammary cells<sup>64</sup>. It is therefore interesting to compare the observed characteristics of breast calcifications with those of bone in varying stages of maturity. Calcifications in specimens with a benign diagnosis have smaller crystalline domains, a smaller 'c' lattice parameter, and a larger 'a' lattice parameter than specimens with *in-situ* or invasive carcinoma. Hydroxyapatite crystallite domain size along the 'c' axis in human foetal bone has been shown to increase with increasing gestational age, accompanied by an increase in c/a lattice parameter ratio<sup>192</sup>. This is shown in

Figure 5-11. This increase in crystallite domain size dimensions continues up to the age of about 20 years, also accompanied by an increase in 'c' lattice parameter and decrease in 'a' lattice parameter<sup>193</sup>.

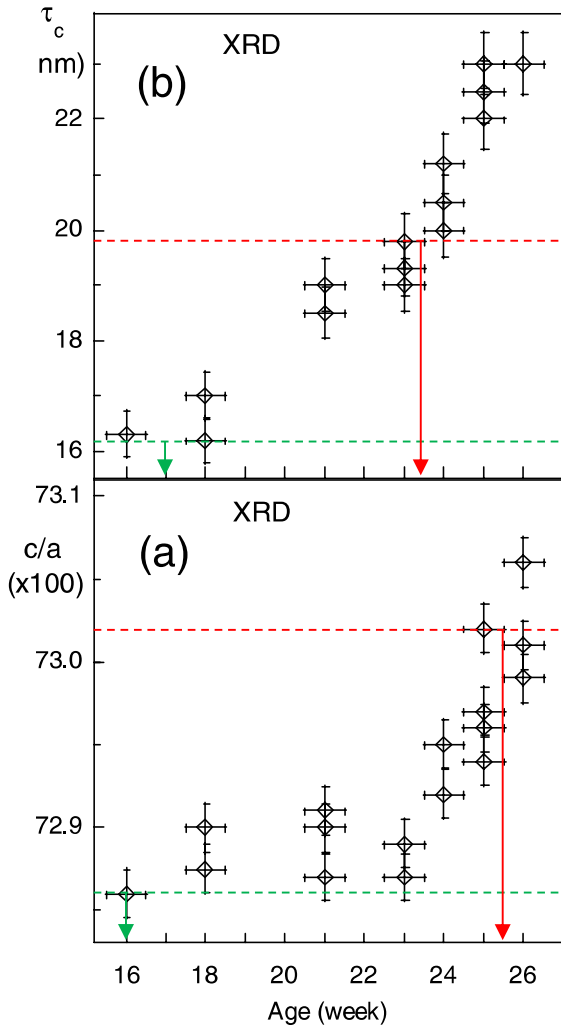


**Figure 5-11 Mean values of calcification c/a lattice parameter ratio (unit cell shape) and crystallite domain size along the 'c' axis ( $\tau_c$ ) for benign and invasive specimens (green and red lines respectively), overlaid on corresponding measurements for foetal bone as a function of the average bone age. Foetal bone measurements reprinted from Dalconi *et al*<sup>192</sup>, with permission from Elsevier.**

This combination of changes in lattice parameters and crystalline domain size with age in both foetal and child bone parallels our observations in breast calcifications from benign to *in-situ* to invasive. The mean 'c' axis domain size in benign breast calcifications of 16.1nm is approximately equivalent to 17 week gestation foetal bone, whereas in invasive specimens the mean 'c' axis domain size of 19.9nm is approximately equivalent to bone at 23 weeks gestation. In addition, the mean c/a ratio of 0.7286 in benign specimens is similar to that of foetal bone at gestational age of 16 weeks, whereas in invasive specimens the



ratio of 0.7302 is similar to that of bone at 25 weeks gestation. Of course these similarities do not imply a temporal progression in the breast calcifications, but may reflect comparable differences in chemistry.

### 5.5.5 Ionic substitutions

Lattice parameters can also give some insight into ionic substitutions within the crystal lattice. Ionic substitutions within the crystal lattice invariably broaden peaks through inhomogeneous strain and restriction of crystallite growth. The observation of broader peaks in benign specimens is therefore consistent with the increased carbonate substitution in benign cases as measured by vibrational spectroscopy<sup>108,109</sup>. However, the lower *c/a* lattice parameter ratio observed in benign specimens is contrary to what would be expected with increased Type B phosphate-site carbonate substitution<sup>194,195</sup>. Divalent carbonate ions can substitute either for monovalent hydroxide ions (Type A substitution) or for trivalent phosphate ions (Type B), or a combination of the two, and in conjunction with a range of charge balancing mechanisms such as  $\text{Ca}^{2+}$  or  $\text{OH}^-$  ion vacancies and substitution of  $\text{PO}_4^{3-}$  by  $\text{HPO}_4^{2-}$  or  $\text{Ca}^{2+}$  by  $\text{Na}^+$ . The nature of carbonate substitution in biological apatites is a complex and controversial topic, and has been the subject of a considerable research over many decades. Early studies suggested that carbonate substitution in biological apatite is of Type B<sup>196</sup>, but recent studies have suggested that mixed A/B carbonate substitution is more consistent with FTIR evidence<sup>197-199</sup>, and that some of the apparent experimental disagreements arise from the shift of FTIR type A band frequencies into the spectral region of type B<sup>200</sup>. Although carbonate is the most common substituent ion in calcified tissue, other ions such as magnesium are also present, and FTIR reveals an unexpected dearth of hydroxide ions<sup>201</sup>. Lattice parameters are therefore difficult to interpret in isolation, and nature and location of substitutions would require further investigation using complementary analytical techniques in the same specimens, such as vibrational spectroscopy and elemental analysis.

### **5.5.6 Spatial variation**

The 'c' axis domain size is slightly larger in the centre of calcifications than at the edge. If maturation processes are similar to bone, with crystalline domain size increasing with time, this indicates that the material at the centre of a calcification is more mature than the material on the outside surface. This observation does not appear to fit with the conjecture that ductal calcifications progressively occlude the lumen from the duct wall inwards. As with the ionic substitutions, interpretation in terms of compositional difference would require a more in-depth investigation using additional analytical techniques.

## **6 Conclusions and Future Work**

### **6.1 Contributions to knowledge**

Research into the relationships between breast pathology and the physico-chemical properties of breast calcifications requires access to a broad range of specimens, covering the growing array of breast cancer classifications and subtypes. Studies using fresh specimens have been hampered by slow recruitment, and limited scope for sampling to avoid compromising pathology assessment. In contrast, diagnostic archives offer a rich source of material for research. In order to make use of this material, it is necessary locate the calcifications within the specimens.

The first contribution of this research is a simple technique for systematically and precisely locating the position of calcifications within a histological section, described in Chapter 2. Although apparently mundane, this proved to be a cornerstone for the rest of the research. Without such a technique, much of the subsequent characterisation would have been difficult and haphazard. This particularly applies to synchrotron experiments, in which beam time is very limited, and it is essential that as little time as possible is wasted hunting for calcifications.

The synchrotron x-ray diffraction experiments reported here are the first ever XRD analysis of breast tissue histological sections, and apparently only the second report of x-ray diffraction experiments on histological sections of any type of tissue.

A small proportion of magnesium whitlockite was discovered in the calcifications, with a substantially larger domain size than the apatite phase. Whitlockite has been reported in other types of pathological calcification but this is the first time that the presence of this phase has been confirmed in breast tissue. The mean whitlockite proportion was found to be significantly higher in malignant specimens than in benign. This may have potential as a marker of malignancy.

This was also the first diffraction study on breast calcifications to go beyond simple phase identification, and make quantitative measurements of crystallographic parameters. These included coherently diffracting domain size (a proxy for crystallite size) and lattice parameters. The analysis showed striking similarities in both these parameters between calcifications and newly formed foetal bone. There was also a significant difference in both domain size and lattice parameter ratio between calcifications in benign and malignant specimens, with malignant specimens akin to a later stage of bone development. This may be important since some breast cancer cells can develop osteoblast-like behaviour (osteomimicry), which is widely acknowledged to be a critical factor in the formation of metastases in bone. The properties of calcifications in the vicinity of a tumour may provide an insight into the phenotype of the cells involved in calcification formation, which may be an indicator of propensity to metastasise.

Previous elemental analyses of breast calcifications have been exclusively qualitative, with the exception of one semi-quantitative study on five specimens. Part of the reason for this is that there are many potential confounding factors affecting SEM/EDS measurement, particularly the fragmented calcifications found in histological sections. A contribution of this work is the development of methods (albeit slow) for addressing these confounding factors.

Elemental composition is of interest not only to help interpret the crystallographic parameters measured in the diffraction study, but also as a potential diagnostic or prognostic indicator in its own right. Differences in calcium to phosphorus ratio could in principle be detected non-invasively by dual energy x-ray material decomposition, as discussed and demonstrated in Chapter 3. However, the SEM/EDS experiments revealed that the Ca:P ratio is very similar in benign and malignant specimens. Minor elements measured included magnesium and sodium. The presence of these has previously been qualitatively reported in breast calcifications, but this is the first time these elements have been quantified. Surprisingly, the Mg:Ca ratio did not differ significantly between benign and malignant specimens, though may be

explained by the labile nature of magnesium in apatite. In contrast, the Na:Ca ratio was found to be substantially and significantly different between benign and malignant specimens. This is consistent with other evidence that the sodium content of malignant cells is elevated. The sodium level within calcifications may provide a useful marker of the intracellular sodium level at the time of calcification formation. This marker appears to survive histological processing, opening up the possibility of studying this in a wide range of archive tissue.

## **6.2 Future work**

The methods developed could be applied to investigate correlations between physico-chemical properties of calcifications and a wide range of breast cancer classifications and subtypes. These include radiological classification of calcification morphology and distribution, and conventional pathology classifications such as nuclear grade and immunohistochemical grade. In addition, linkage with cancer registries could in principle enable a direct correlation to be made with disease-free survival and mortality.

Improvements have been identified that could increase the speed of measurement of both synchrotron XRD and SEM/EDS analysis, to expedite measurement of larger number of specimens. The XRD experimental setup could be improved to eliminate shadowing artefacts and to collect both the small angle OCP (100) peak (OCP is a potential precursor of HA) and the HA (004) peak (to facilitate Williamson-Hall size-strain analysis).

Complementary techniques applied to the same specimens would be useful to corroborate and expand on results from XRD and EDS. Vibrational spectroscopy (Raman and/or FTIR) would enable a direct correlation between crystallographic parameters and anion substitutions, particularly carbonate. Laser Induced Breakdown Spectroscopy (LIBS) is a promising alternative technique for measuring elemental composition. This has been used to measure the composition of bones, teeth, nails and calcified biomaterials<sup>202-204</sup>, and has also been used to discriminate between malignant and non-neoplastic soft tissue in the breast<sup>205,206</sup>. This has the advantage of being very much faster

than SEM/EDS, and is substantially more sensitive for quantifying trace elements.

The discovery of elevated sodium levels in malignant breast calcifications raises the possibility of measurement of soft tissue ion concentrations using micro ion electrodes<sup>207,208</sup>. Potential applications include intraoperative margin analysis and biopsy needle guidance. Measurement of sodium in calcifications could lay the groundwork for this, since this appears to act as a marker of soft tissue sodium content which survives histological processing. Measurements could thus be conducted archival specimens representing a wide range of breast tumour characteristics such as size, type, grade, and IHC scores. This could uncover the relationships between tissue sodium and pathology more quickly and easily than collecting a similar range of fresh soft tissue.

## REFERENCES

1. World Health Organisation. Early detection of cancer. Available at: <http://www.who.int/cancer/detection/en/>. (Accessed: 14th January 2017)
2. Pilewskie, M., Olcese, C., Patil, S. & Van Zee, K. J. Women with Low-Risk DCIS Eligible for the LORIS Trial After Complete Surgical Excision: How Low Is Their Risk After Standard Therapy? *Ann. Surg. Oncol.* **23**, 4253–4261 (2016).
3. Weigel, S. *et al.* Calcifications in digital mammographic screening: improvement of early detection of invasive breast cancers? *Radiology* **255**, 738–45 (2010).
4. Stomper, P. C., D'Souza, D. J., DiNitto, P. A. & Arredondo, M. A. Analysis of parenchymal density on mammograms in 1353 women 25-79 years old. *AJR. Am. J. Roentgenol.* **167**, 1261–5 (1996).
5. Sickles, E. A., D'Orsi, C. J. & Bassett, L. W. in *ACR BI-RADS® Atlas, Breast Imaging Reporting and Data System* (American College of Radiology, 2013).
6. Maxwell, A. J. *et al.* The Royal College of Radiologists Breast Group breast imaging classification. *Clin. Radiol.* **64**, 624–627 (2009).
7. Sanders, M. A., Roland, L. & Sahoo, S. Clinical implications of subcategorizing BI-RADS 4 breast lesions associated with microcalcification: A radiology-pathology correlation study. *Breast J.* **16**, 28–31 (2010).
8. Henrot, P., Leroux, A., Barlier, C. & Génin, P. Breast microcalcifications: the lesions in anatomical pathology. *Diagn. Interv. Imaging* **95**, 141–52 (2014).
9. Health and Social Care Information Centre. Breast Screening Programme, England 2014-15. 1–60 (2016). Available at: <http://www.hscic.gov.uk/catalogue/PUB20018/bres-scre-prog-eng-2014-15-rep.pdf>. (Accessed: 26th September 2016)
10. Bond, M. *et al.* Psychological consequences of false-positive screening mammograms in the UK. *Evid. Based. Med.* **18**, 54–61 (2013).
11. Nelson, H. D. *et al.* *Screening for Breast Cancer: A Systematic Review to Update the 2009 U.S. Preventive Services Task Force Recommendation.* *AHRQ Publication No. 14-05201-EF-1* (2016).
12. Brawley, O. W. Accepting the Existence of Breast Cancer Overdiagnosis. *Ann. Intern. Med.* **166**, 364–365 (2017).
13. Benson, J. R., Jatoi, I. & Toi, M. Treatment of low-risk ductal carcinoma in situ: is nothing better than something? *Lancet Oncol.* **17**, e442–e451 (2016).
14. Groen, E. J. *et al.* Finding the balance between over- and under-treatment of ductal carcinoma in situ (DCIS). *The Breast* **31**, 274–283 (2017).
15. Independent UK Panel on Breast Cancer Screening. The benefits and harms of

- breast cancer screening: an independent review. *Lancet* **380**, 1778–86 (2012).
16. Gøtzsche, P. C. P. & Jørgensen, K. J. K. Screening for breast cancer with mammography. *Cochrane Database Syst Rev* **6**, CD001877 (2013).
  17. Harding, C. *et al.* Breast Cancer Screening, Incidence, and Mortality Across US Counties. *JAMA Intern. Med.* **175**, 1483–9 (2015).
  18. Miller, A. B. B. *et al.* Twenty five year follow-up for breast cancer incidence and mortality of the Canadian National Breast Screening Study: randomised screening trial. *BMJ* **348**, g366 (2014).
  19. Jin, J. Breast Cancer Screening: Benefits and Harms. *JAMA* **312**, 2585 (2014).
  20. Cianfrocca, M. & Goldstein, L. J. Prognostic and predictive factors in early-stage breast cancer. *Oncologist* **9**, 606–16 (2004).
  21. Weigelt, B., Peterse, J. L. & van 't Veer, L. J. Breast cancer metastasis: markers and models. *Nat. Rev. Cancer* **5**, 591–602 (2005).
  22. NHS Cancer Screening Programmes and The Royal College of Pathologists. *Pathology Reporting of Breast Tissue. NHSBSP Publication No 58.* (2005).
  23. Public Health England and Cambridge University. predict. Available at: <http://www.predict.nhs.uk/>. (Accessed: 3rd February 2017)
  24. Wishart, G. C. *et al.* PREDICT: a new UK prognostic model that predicts survival following surgery for invasive breast cancer. *Breast Cancer Res.* **12**, R1 (2010).
  25. Perou, C. M. *et al.* Molecular portraits of human breast tumours. *Nature* **406**, 747–52 (2000).
  26. Dai, X. *et al.* Breast cancer intrinsic subtype classification, clinical use and future trends. *Am. J. Cancer Res.* **5**, 2929–43 (2015).
  27. Rakha, E. A. *et al.* Breast cancer prognostic classification in the molecular era: the role of histological grade. *Breast Cancer Res.* **12**, 207 (2010).
  28. Ellis, I. O. *et al.* Impact of a national external quality assessment scheme for breast pathology in the UK. *J. Clin. Pathol.* **59**, 138–45 (2006).
  29. Benson, J. R. & Wishart, G. C. Predictors of recurrence for ductal carcinoma in situ after breast-conserving surgery. *Lancet Oncol.* **14**, e348-57 (2013).
  30. Weigelt, B., Baehner, F. L. & Reis-filho, J. S. The contribution of gene expression profiling to breast cancer classification, prognostication and prediction: A retrospective of the last decade. *J. Pathol.* **220**, 263–280 (2010).
  31. Michiels, S., Ternès, N. & Rotolo, F. Statistical controversies in clinical research: prognostic gene signatures are not (yet) useful in clinical practice. *Ann. Oncol.* mdw307 (2016). doi:10.1093/annonc/mdw307
  32. Rakha, E. A. & Green, A. R. Molecular classification of breast cancer: what the



- pathologist needs to know. *Pathology* **49**, 111–119 (2017).
33. Nyante, S. J., Lee, S. S., Benefield, T. S., Hoots, T. N. & Henderson, L. M. The association between mammographic calcifications and breast cancer prognostic factors in a population-based registry cohort. *Cancer* **123**, 219–227 (2017).
  34. Tabár, L. *et al.* A novel method for prediction of long-term outcome of women with T1a, T1b, and 10-14 mm invasive breast cancers: a prospective study. *Lancet* **355**, 429–33 (2000).
  35. Blamey, R. W. Long-term outcome of invasive breast cancer. *Lancet (London, England)* **355**, 1552; author reply 1552-3 (2000).
  36. Peacock, C., Given-Wilson, R. & Duffy, S. Mammographic casting-type calcification associated with small screen-detected invasive breast cancers: is this a reliable prognostic indicator? *Clin. Radiol.* **59**, 855 (2004).
  37. Thurfjell, E., Thurfjell, M. G. & Lindgren, A. Mammographic finding as predictor of survival in 1–9mm invasive breast cancers. Worse prognosis for cases presenting as calcifications alone. *Breast Cancer Res. Treat.* **67**, 177–180 (2001).
  38. Pálka, I., Ormándi, K., Gaál, S., Boda, K. & Kahán, Z. Casting-type calcifications on the mammogram suggest a higher probability of early relapse and death among high-risk breast cancer patients. *Acta Oncol.* **46**, 1178–1183 (2007).
  39. Bennett, R. L. *et al.* Pathological and mammographic prognostic factors for screen detected cancers in a multi-centre randomised, controlled trial of mammographic screening in women from age 40 to 48 years. *Breast* **20**, 525–528 (2011).
  40. Tabár, L. *et al.* The use of mammographic tumour feature significantly improves outcome prediction of breast cancers smaller than 15 mm: A reproducibility study from two comprehensive breast centres. *Memo - Mag. Eur. Med. Oncol.* **4**, 149–157 (2011).
  41. Månsson, E., Bergkvist, L., Christenson, G., Persson, C. & Wärnberg, F. Mammographic casting-type calcifications is not a prognostic factor in unifocal small invasive breast cancer: A population-based retrospective cohort study. *J. Surg. Oncol.* **100**, 670–674 (2009).
  42. James, J. J. *et al.* Is the presence of mammographic comedo calcification really a prognostic factor for small screen-detected invasive breast cancers? *Clin. Radiol.* **58**, 54–62 (2003).
  43. Holmberg, L. *et al.* Mammography casting-type calcification and risk of local recurrence in DCIS: analyses from a randomised study. *Br. J. Cancer* **108**, 812–9 (2013).
  44. Kelemen, G. *et al.* The relationship of multifocality and tumor burden with various tumor characteristics and survival in early breast cancer. *Neoplasma* **59**,

- 566–73 (2012).
45. Malik, H. Z., Wilkinson, L., George, W. D. & Purushotham, A. D. Preoperative mammographic features predict clinicopathological risk factors for the development of local recurrence in breast cancer. *Breast* **9**, 329–333 (2000).
  46. Gold, R. H., Bassett, L. W. & Widoff, B. E. Highlights from the history of mammography. *Radiographics* **10**, 1111–31 (1990).
  47. Hemberg, O., Otendal, M. & Hertz, H. M. Liquid-metal-jet anode electron-impact x-ray source. *Appl. Phys. Lett.* **83**, 1483–1485 (2003).
  48. Vegso, K. *et al.* Real-time SAXS study of a strain gauge based on a self-assembled gold nanoparticle monolayer. *Sensors Actuators, A Phys.* **241**, 87–95 (2016).
  49. Krenkel, M., Töpperwien, M., Dullin, C., Alves, F. & Salditt, T. Propagation-based phase-contrast tomography for high-resolution lung imaging with laboratory sources. *AIP Adv.* **6**, (2016).
  50. Larsson, D. H. *et al.* First application of liquid-metal-jet sources for small-animal imaging: high-resolution CT and phase-contrast tumor demarcation. *Med. Phys.* **40**, 21909 (2013).
  51. Glynn, C. G. *et al.* Effect of transition to digital mammography on clinical outcomes. *Radiology* **260**, 664–70 (2011).
  52. Perry, N. M. *et al.* The impact of digital mammography on screening a young cohort of women for breast cancer in an urban specialist breast unit. *Eur. Radiol.* **21**, 676–682 (2011).
  53. de Munck, L. *et al.* Digital vs screen-film mammography in population-based breast cancer screening: performance indicators and tumour characteristics of screen-detected and interval cancers. *Br J Cancer* **115**, 517–524 (2016).
  54. van Luijt, P. A. *et al.* Nation-wide data on screening performance during the transition to digital mammography: observations in 6 million screens. *Eur. J. Cancer* **49**, 3517–25 (2013).
  55. Bluekens, A. M. J. *et al.* Consequences of digital mammography in population-based breast cancer screening: Initial changes and long-term impact on referral rates. *Eur. Radiol.* **20**, 2067–2073 (2010).
  56. Porter, A. J., Evans, E. B. & Erzetich, L. M. Full-field digital mammography: Is the apparent increased detection of microcalcification leading to over-investigation and over-diagnosis? *J. Med. Imaging Radiat. Oncol.* 1–6 (2017). doi:10.1111/1754-9485.12581
  57. Hambly, N. M. *et al.* Comparison of digital mammography and screen-film mammography in breast cancer screening: a review in the Irish breast screening program. *AJR. Am. J. Roentgenol.* **193**, 1010–8 (2009).
  58. Giachelli, C. M. Ectopic Calcification. *Am. J. Pathol.* **154**, 671–675 (1999).

59. Bilgen, I. G., Ustun, E. E. & Memis, A. Fat necrosis of the breast: clinical, mammographic and sonographic features. *Eur. J. Radiol.* **39**, 92–9 (2001).
60. Tse, G. M., Tan, P.-H., Cheung, H. S., Chu, W. C. W. & Lam, W. W. M. Intermediate to highly suspicious calcification in breast lesions: A radio-pathologic correlation. *Breast Cancer Res. Treat.* **110**, 1–7 (2008).
61. Feliciano, Y. *et al.* Do Calcifications Seen on Mammography After Neoadjuvant Chemotherapy for Breast Cancer Always Need to Be Excised? *Ann. Surg. Oncol.* (2017). doi:10.1245/s10434-016-5741-y
62. Cox, R. F., Jenkinson, A., Pohl, K., O'Brien, F. J. & Morgan, M. P. Osteomimicry of Mammary Adenocarcinoma Cells In Vitro; Increased Expression of Bone Matrix Proteins and Proliferation within a 3D Collagen Environment. *PLoS One* **7**, e41679 (2012).
63. Scimeca, M. *et al.* Microcalcifications in breast cancer: an active phenomenon mediated by epithelial cells with mesenchymal characteristics. *BMC Cancer* **14**, 286 (2014).
64. Cox, R. F. & Morgan, M. P. Microcalcifications in breast cancer: Lessons from physiological mineralization. *Bone* **53**, 437–450 (2013).
65. Bellahcène, A., Merville, M. P. & Castronovo, V. Expression of bone sialoprotein, a bone matrix protein, in human breast cancer. *Cancer Res.* **54**, 2823–6 (1994).
66. Pulido, C. *et al.* Bone metastasis risk factors in breast cancer. *Ecancermedicalscience* **11**, 1–17 (2017).
67. Morgan, M. P., Cooke, M. M. & McCarthy, G. M. Microcalcifications associated with breast cancer: an epiphenomenon or biologically significant feature of selected tumors? *J. Mammary Gland Biol. Neoplasia* **10**, 181–7 (2005).
68. Choi, S., Coonrod, S., Estroff, L. & Fischbach, C. Chemical and physical properties of carbonated hydroxyapatite affect breast cancer cell behavior. *Acta Biomater.* **24**, 333–342 (2015).
69. Cox, R. F. *et al.* Microcalcifications in breast cancer: novel insights into the molecular mechanism and functional consequence of mammary mineralisation. *Br. J. Cancer* **106**, 525–37 (2012).
70. Siddharth, P., Lin, D., Dorvee, J., Estroff, L. A. & Fischbach, C. Hydroxyapatite nanoparticle-containing scaffolds for the study of breast cancer bone metastasis. *Biomaterials* **32**, 5112–5122 (2011).
71. Paget, S. THE DISTRIBUTION OF SECONDARY GROWTHS IN CANCER OF THE BREAST. *Lancet* **133**, 571–573 (1889).
72. Jin, X. & Mu, P. Targeting Breast Cancer Metastasis. *Lib. Acad.* **9**, 23–34 (2015).
73. Knerr, K., Ackermann, K., Neidhart, T. & Pyerin, W. Bone metastasis: Osteoblasts affect growth and adhesion regulons in prostate tumor cells and

- provoke osteomimicry. *Int. J. Cancer* **111**, 152–159 (2004).
74. Awolaran, O., Brooks, S. A. & Lavender, V. Breast cancer osteomimicry and its role in bone specific metastasis; an integrative, systematic review of preclinical evidence. *Breast* **30**, 156–171 (2016).
  75. Hüseemann, Y. *et al.* Systemic spread is an early step in breast cancer. *Cancer Cell* **13**, 58–68 (2008).
  76. D’Orsi, C. J., Reale, F. R., Davis, M. A. & Brown, V. J. Is calcium oxalate an adequate explanation for nonvisualization of breast specimen calcifications? *Radiology* **182**, 801–3 (1992).
  77. Going, J. J., Anderson, T. J., Crocker, P. R. & Levison, D. A. Weddellite calcification in the breast: eighteen cases with implications for breast cancer screening. *Histopathology* **16**, 119–24 (1990).
  78. Tornos, C., Silva, E., el-Naggar, A. & Pritzker, K. P. Calcium oxalate crystals in breast biopsies. The missing microcalcifications. *Am. J. Surg. Pathol.* **14**, 961–8 (1990).
  79. Gonzalez, J. E., Caldwell, R. G. & Valaitis, J. Calcium oxalate crystals in the breast. Pathology and significance. *Am. J. Surg. Pathol.* **15**, 586–91 (1991).
  80. Radi, M. J. Calcium oxalate crystals in breast biopsies. An overlooked form of microcalcification associated with benign breast disease. *Arch. Pathol. Lab. Med.* **113**, 1367–9 (1989).
  81. Winston, J. S., Yeh, I. T., Evers, K. & Friedman, A. K. Calcium oxalate is associated with benign breast tissue. Can we avoid biopsy? *Am. J. Clin. Pathol.* **100**, 488–92 (1993).
  82. Winston, J. S., Geradts, J., Liu, D. F. & Stomper, P. C. Microtome shaving radiography: demonstration of loss of mammographic microcalcifications during histologic sectioning. *Breast J.* **10**, 200–3 (2004).
  83. Frappart, L. *et al.* Structure and composition of microcalcifications in benign and malignant lesions of the breast: study by light microscopy, transmission and scanning electron microscopy, microprobe analysis, and X-ray diffraction. *Hum. Pathol.* **15**, 880–9 (1984).
  84. Frappart, L. *et al.* Different types of microcalcifications observed in breast pathology. Correlations with histopathological diagnosis and radiological examination of operative specimens. *Virchows Arch. A. Pathol. Anat. Histopathol.* **410**, 179–87 (1986).
  85. Singh, N. & Theaker, J. M. Calcium oxalate crystals (Weddellite) within the secretions of ductal carcinoma in situ—a rare phenomenon. *J. Clin. Pathol.* **52**, 145–6 (1999).
  86. Martin, H. M., Bateman, A. C. & Theaker, J. M. Calcium oxalate (Weddellite) crystals within ductal carcinoma in situ. *J. Clin. Pathol.* **52**, 932 (1999).

87. Castellaro, A. M. *et al.* Oxalate induces breast cancer. *BMC Cancer* 1–13 (2015). doi:10.1186/s12885-015-1747-2
88. Ahmed, A. Calcification in human breast carcinomas: ultrastructural observations. *J. Pathol.* **117**, 247–51 (1975).
89. Galkin, B. M. *et al.* Ultrastructure and microanalysis of ‘benign’ and ‘malignant’ breast calcifications. *Radiology* **124**, 245–9 (1977).
90. Büsing, C., Keppler, U. & Menges, V. Differences in microcalcification in breast tumors. *Virchows Arch.* **393**, 307–313 (1981).
91. Fandos-Morera, A., Prats-Esteve, M., Tura-Soteras, J. M. & Traveria-Cros, A. Breast tumors: composition of microcalcifications. *Radiology* **169**, 325–7 (1988).
92. Ng, K. H., Looi, L. M. & Bradley, D. A. The elemental composition of breast tissue: Can this be related to breast particle deposition? *J. Radioanal. Nucl. Chem.* **217**, 193–199 (1997).
93. Galkin, B. M., Frasca, P., Feig, S. A. & Holderness, K. E. Non-calcified breast particles: a possible new marker of breast cancer. *Invest. Radiol.* **17**, 119–28 (1982).
94. Galkin, B. M., Feig, S. A., Patchefsky, A. S. & Muir, H. D. Elemental analysis of breast calcifications. *Recent Results Cancer Res.* **105**, 89–94 (1987).
95. Newbury, D. E. Mistakes encountered during automatic peak identification of minor and trace constituents in electron-excited energy dispersive X-ray microanalysis. *Scanning* **31**, 91–101 (2009).
96. Poggi, S. H., Skinner, H. C. W., Ague, J. J. & Carter, D. Using scanning electron microscopy to study mineral deposits in breast tissues. *Am. Mineral.* **83**, 1122–1126 (1998).
97. Lewis, R. A. Medical phase contrast x-ray imaging: current status and future prospects. *Phys. Med. Biol.* **49**, 3573–3583 (2004).
98. Pfeiffer, F., Weitkamp, T., Bunk, O. & David, C. Phase retrieval and differential phase-contrast imaging with low-brilliance X-ray sources. *Nat. Phys.* **2**, 258–261 (2006).
99. Pfeiffer, F. *et al.* Hard-X-ray dark-field imaging using a grating interferometer. *Nat. Mater.* **7**, 134–7 (2008).
100. Michel, T. *et al.* On a dark-field signal generated by micrometer-sized calcifications in phase-contrast mammography. *Phys. Med. Biol.* **58**, 2713–32 (2013).
101. Wang, Z. *et al.* Non-invasive classification of microcalcifications with phase-contrast X-ray mammography. *Nat. Commun.* **5**, 3797 (2014).
102. Scherer, K. *et al.* Improved Diagnostics by Assessing the Micromorphology of Breast Calcifications via X-Ray Dark-Field Radiography. *Sci. Rep.* **6**, 36991

- (2016).
103. Gufler, H., Wagner, S. & Franke, F. E. The interior structure of breast microcalcifications assessed with micro computed tomography. *Acta radiol.* **52**, 592–6 (2011).
  104. Wang, H., Kashyap, Y. & Sawhney, K. From synchrotron radiation to lab source: advanced speckle-based X-ray imaging using abrasive paper. *Sci. Rep.* **6**, 20476 (2016).
  105. Ghammraoui, B. & Popescu, L. M. Non-invasive classification of breast microcalcifications using x-ray coherent scatter computed tomography. *Phys. Med. Biol.* **62**, 1192 (2017).
  106. Martini, N. *et al.* Modeling of the Calcium/Phosphorus Mass ratio for Breast Imaging. *J. Phys. Conf. Ser.* **633**, 12094 (2015).
  107. Ghammraoui, B. & Glick, S. J. Investigating the feasibility of classifying breast microcalcifications using photon-counting spectral mammography: a simulation study. *Med. Phys.* **38**, 42–49 (2017).
  108. Haka, A. S. *et al.* Identifying microcalcifications in benign and malignant breast lesions by probing differences in their chemical composition using Raman spectroscopy. *Cancer Res.* **62**, 5375–80 (2002).
  109. Baker, R., Rogers, K. D., Shepherd, N. & Stone, N. New relationships between breast microcalcifications and cancer. *Br. J. Cancer* **103**, 1034–9 (2010).
  110. Baker, R. *et al.* Depth profiling of calcifications in breast tissue using picosecond Kerr-gated Raman spectroscopy. *Analyst* **132**, 48–53 (2007).
  111. Stone, N., Baker, R., Rogers, K., Parker, A. W. & Matousek, P. Subsurface probing of calcifications with spatially offset Raman spectroscopy (SORS): future possibilities for the diagnosis of breast cancer. *Analyst* **132**, 899–905 (2007).
  112. Robinson, M. & Kotre, C. J. Trends in compressed breast thickness and radiation dose in breast screening mammography. *Br. J. Radiol.* **81**, 214–8 (2008).
  113. Stone, N. & Matousek, P. Advanced transmission Raman spectroscopy: a promising tool for breast disease diagnosis. *Cancer Res.* **68**, 4424–30 (2008).
  114. Saha, A. *et al.* Raman spectroscopy: a real-time tool for identifying microcalcifications during stereotactic breast core needle biopsies. *Biomed. Opt. Express* **2**, 2792–803 (2011).
  115. Scott, R., Kendall, C., Stone, N. & Rogers, K. Locating microcalcifications in breast histopathology sections using micro CT and XRF mapping. *Anal. Methods* **6**, 3962 (2014).
  116. Dixon, A. D. & Howarth, P. A photographic method of graphic reconstruction. *J. Anat.* **92**, 162–6 (1958).

117. Clarke, G. E., Hamilton, P. W. & Montgomery, W. A. Aligning histological serial sections for three-dimensional reconstruction using an excimer laser beam. *Pathol. Res. Pract.* **189**, 563–566 (1993).
118. Deverell, M. H. & Whimster, W. F. A method of image registration for three-dimensional reconstruction of microscopic structures using an IBAS 2000 image analysis system. *Pathol. Res. Pract.* **185**, 602–5 (1989).
119. Shojaii, R. & Martel, A. L. Multi-modality fiducial marker for validation of registration of medical images with histology. in *Progress in Biomedical Optics and Imaging - Proceedings of SPIE* (eds. Dawant, B. M. & Haynor, D. R.) **7623**, 762331-762331–8 (2010).
120. Bird, B. *et al.* Detection of breast micro-metastases in axillary lymph nodes by infrared micro-spectral imaging. *Analyst* **134**, 1067–1076 (2009).
121. Schneider, C. A., Rasband, W. S. & Eliceiri, K. W. NIH Image to ImageJ: 25 years of image analysis. *Nat. Methods* **9**, 671–675 (2012).
122. Jones, A. S., Milthorpe, B. K. & Howlett, C. R. Measurement of microtomy-induced section distortion and its correction for 3-dimensional histological reconstructions. *Cytometry* **15**, 95–105 (1994).
123. Hubbell, J. H. & Seltzer, S. M. Tables of X-Ray Mass Attenuation Coefficients and Mass Energy-Absorption Coefficients (version 1.4). (2004). Available at: <http://physics.nist.gov/xaamdi>. (Accessed: 17th October 2013)
124. Cameron, J. R. & Sorenson, J. Measurement of Bone Mineral in vivo: An Improved Method. *Science* (80-. ). **142**, 230–232 (1963).
125. Thorson, L. M. & Wahner, H. W. Single- and dual-photon absorptiometry techniques for bone mineral analysis. *J Nucl. Med. Technol.* **14**, 163–171 (1986).
126. Kotzki, P. O., Mariano-Goulart, D. & Rossi, M. Theoretical and experimental limits of triple photon energy absorptiometry in the measurement of bone mineral. *Phys. Med. Biol.* **36**, 429–37 (1991).
127. Fountos, G., Yasumura, S. & Glaros, D. The skeletal calcium/phosphorus ratio: A new in vivo method of determination. *Med. Phys.* **24**, 1303 (1997).
128. Dromain, C. *et al.* Dual-energy contrast-enhanced digital mammography: Initial clinical results. *Eur. Radiol.* **21**, 565–574 (2011).
129. Taguchi, K. & Iwanczyk, J. S. Vision 2020: Single photon counting x-ray detectors in medical imaging. *Med. Phys.* **40**, 100901 (2013).
130. Kilburn-Toppin, F. & Barter, S. J. New horizons in breast imaging. *Clin. Oncol. (R. Coll. Radiol.)* **25**, 93–100 (2013).
131. Kappadath, S. C. & Shaw, C. C. Dual-energy digital mammography for calcification imaging: noise reduction techniques. *Phys. Med. Biol.* **53**, 5421–43 (2008).

132. Brettle, D. S. & Cowen, a R. Dual-energy digital mammography utilizing stimulated phosphor computed radiography. *Phys. Med. Biol.* **39**, 1989–2004 (1994).
133. Ding, H. & Molloy, S. Quantification of breast density with spectral mammography based on a scanned multi-slit photon-counting detector: a feasibility study. *Phys. Med. Biol.* **57**, 4719–38 (2012).
134. Boyd, N. F. *et al.* Mammographic density and the risk and detection of breast cancer. *N. Engl. J. Med.* **356**, 227–36 (2007).
135. Berry, E. E. The structure and composition of some calcium-deficient apatites—II. *J. Inorg. Nucl. Chem.* **29**, 1585–1590 (1967).
136. Joris, S. J. & Amberg, C. H. Nature of deficiency in nonstoichiometric hydroxyapatites. II. Spectroscopic studies of calcium and strontium hydroxyapatites. *J. Phys. Chem.* **75**, 3172–3178 (1971).
137. Blake, G. M., McKeeney, D. B., Chhaya, S. C., Ryan, P. J. & Fogelman, I. Dual energy x-ray absorptiometry: the effects of beam hardening on bone density measurements. *Med. Phys.* **19**, 459–65 (1992).
138. Kwang Hyun Kim. X-Ray Filter Design and Its Evaluation in Dual-Energy X-Ray Absorptiometry (DXA). *IEEE Trans. Nucl. Sci.* **57**, 2155–2158 (2010).
139. Siewerdsen, J. H. & Jaffray, D. a. A ghost story: spatio-temporal response characteristics of an indirect-detection flat-panel imager. *Med. Phys.* **26**, 1624–41 (1999).
140. Mail, N., O’Brien, P. & Pang, G. Lag correction model and ghosting analysis for an indirect-conversion flat-panel imager. *J. Appl. Clin. Med. Phys.* **8**, 2483 (2007).
141. Ducote, J. L. & Molloy, S. Scatter correction in digital mammography based on image deconvolution. *Phys. Med. Biol.* **55**, 1295–309 (2010).
142. Aslund, M., Cederström, B., Lundqvist, M. & Danielsson, M. Scatter rejection in multislit digital mammography. *Med. Phys.* **33**, 933–40 (2006).
143. Johnson, T. R. C. Dual-energy CT: general principles. *AJR. Am. J. Roentgenol.* **199**, S3-8 (2012).
144. Maidment, A. D. A. *et al.* in *Digital Mammography* 144–151 (Springer, 2006).
145. Scott, R., Kendall, C., Stone, N. & Rogers, K. Elemental vs. phase composition of breast calcifications. *Sci. Rep.* **7**, 136 (2017).
146. Winters, C., Davies, R. L., Morgan, a. J. & Gravelle, I. H. Human breast microcalcification: Comparative study involving contact microradiography and backscattered-electron-imaging plus x-ray microanalysis. *Micron Microsc. Acta* **17**, 11–23 (1986).
147. Goldstein, J. *et al.* *Scanning Electron Microscopy and X-ray Microanalysis:*



*Third Edition.* (Springer, 2003).

148. Abdelgawad, I. A., El-Mously, R. H., Saber, M. M., Mansour, O. A. & Shouman, S. A. Significance of serum levels of vitamin D and some related minerals in breast cancer patients. *Int. J. Clin. Exp. Pathol.* **8**, 4074–82 (2015).
149. Wolf, F. I. & Trapani, V. Magnesium and its transporters in cancer: a novel paradigm in tumour development. *Clin. Sci.* **123**, 417–27 (2012).
150. Bertran, O. *et al.* Synergistic approach to elucidate the incorporation of magnesium ions into hydroxyapatite. *Chemistry* **21**, 2537–2546 (2015).
151. Leidi, M., Wolf, F. I. & Maier, J. A. M. in *Magnesium in the Central Nervous System* (eds. Vink, R. & Nechifor, M.) 217–228 (University of Adelaide Press, 2011). doi:10.1017/UPO9780987073051.017
152. Castiglioni, S. & Maier, J. A. M. Magnesium and cancer: a dangerous liason. *Magnes. Res.* **24**, S92-100 (2011).
153. Rattenberger, J., Wagner, J., Schröttner, H., Mitsche, S. & Zankel, A. A method to measure the total scattering cross section and effective beam gas path length in a low-vacuum SEM. *Scanning* **31**, 107–13 (2009).
154. Drouin, D. *et al.* CASINO V2.42—A Fast and Easy-to-use Modeling Tool for Scanning Electron Microscopy and Microanalysis Users. *Scanning* **29**, 92–101 (2007).
155. Lakhdar, A. Ben *et al.* Underlining the complexity of the structural and chemical characteristics of ectopic calcifications in breast tissues through FE-SEM and  $\mu$ FTIR spectroscopy. *Comptes Rendus Chim.* **19**, 1610–1624 (2016).
156. Carpenter, J. & Bithell, J. Bootstrap confidence intervals: When, which, what? A practical guide for medical statisticians. *Stat. Med.* **19**, 1141–1164 (2000).
157. Canty, A. & Ripley, B. boot: Bootstrap R (S-Plus) Functions. R package. (2016).
158. Zaichick, V. Data for the Reference Man: skeleton content of chemical elements. *Radiat. Environ. Biophys.* **52**, 65–85 (2013).
159. Ouwerkerk, R. *et al.* Elevated tissue sodium concentration in malignant breast lesions detected with non-invasive  $^{23}\text{Na}$  MRI. *Breast Cancer Res. Treat.* **106**, 151–60 (2007).
160. Zaric, O. *et al.* Quantitative Sodium MR Imaging at 7 T: Initial Results and Comparison with Diffusion-weighted Imaging in Patients with Breast Tumors. *Radiology* **280**, 39–48 (2016).
161. Scott, R., Stone, N., Kendall, C., Geraki, K. & Rogers, K. Relationships between pathology and crystal structure in breast calcifications: an in situ X-ray diffraction study in histological sections. *npj Breast Cancer* **2**, 16029 (2016).
162. Fischer, D.-C. *et al.* Arterial microcalcification in atherosclerotic patients with and without chronic kidney disease: a comparative high-resolution scanning X-

- ray diffraction analysis. *Calcif. Tissue Int.* **90**, 465–72 (2012).
163. Schlieper, G. *et al.* Ultrastructural analysis of vascular calcifications in uremia. *J. Am. Soc. Nephrol.* **21**, 689–696 (2010).
  164. Basham, M. *et al.* *Data Analysis Workbench ( DAWN )*. *J. Synchrotron Radiat.* **22**, 853–858 (2015).
  165. R Core Team. R: A Language and Environment for Statistical Computing. (2015). Available at: <https://www.r-project.org/>.
  166. Liland, K. H. 4S Peak Filling – baseline estimation by iterative mean suppression. *MethodsX* **2**, 135–140 (2015).
  167. Boyce, B. L., Furnish, T. A., Padilla, H. A., Van Campen, D. & Mehta, A. Detecting rare, abnormally large grains by x-ray diffraction. *J. Mater. Sci.* **50**, 6719–6729 (2015).
  168. *ICDD PDF-2 2015 Database*. (International Centre for Diffraction Data, Newtown Square, PA, USA).
  169. Rodriguez-Carvajal, J. Study of Micro-Structural Effects by Powder Diffraction Using the Program FULLPROF. *Lab. Léon Brillouin (CEA-CNRS), CEA/Saclay* (2003).
  170. Mittemeijer, E. J. & Welzel, U. in *Modern Diffraction Methods* (eds. Mittemeijer, E. J. & Welzel, U.) 87–126 (Wiley-VCH Verlag GmbH & Co. KGaA, 2013). doi:10.1002/9783527649884.ch4
  171. Langford, J. I. in *Accuracy in Powder Diffraction II* (ed. E. O. Prince and J. K. Stalick) 110–126 (NIST, 1992).
  172. Langford, J. I., Boulton, A., Auffrédic, J. P. & Louër, D. The use of pattern decomposition to study the combined X-ray diffraction effects of crystallite size and stacking faults in ex-oxalate zinc oxide. *J. Appl. Crystallogr.* **26**, 22–33 (1993).
  173. Wheeler, E. J. & Lewis, D. An x-ray study of the paracrystalline nature of bone apatite. *Calcif. Tissue Res.* **24**, 243–8 (1977).
  174. Markovic, M., Fowler, B. B. O. & Tung, M. S. Preparation and Comprehensive Characterization of a Calcium Hydroxyapatite Reference Material. *J. Res. Natl. Inst. Stand. Technol.* **109**, 553–568 (2004).
  175. Dessombz, A., Méria, P., Bazin, D. & Daudon, M. Prostatic Stones: Evidence of a Specific Chemistry Related to Infection and Presence of Bacterial Imprints. *PLoS One* **7**, 1–5 (2012).
  176. Reid, J. D. & Andersen, M. E. Medial calcification (whitlockite) in the aorta. *Atherosclerosis* **101**, 213–24 (1993).
  177. Scotchford, C. A. & Ali, S. Y. Magnesium whitlockite deposition in articular cartilage: a study of 80 specimens from 70 patients. *Ann Rheum Dis* **54**, 339–344

- (1995).
178. Burnstein, L. S., Boskey, A. L., Tannenbaum, P. J., Posner, A. S. & Mandel, I. D. The crystal chemistry of submandibular and parotid salivary gland stones. *J. Oral Pathol.* **8**, 284–91 (1979).
  179. Kerssens, M. Study of calcification formation and disease diagnostics utilising advanced vibrational spectroscopy. (Cranfield University, 2012).
  180. Bertoni, E. *et al.* Nanocrystals of magnesium and fluoride substituted hydroxyapatite. *J. Inorg. Biochem.* **72**, 29–35 (1998).
  181. Bigi, A. *et al.* Magnesium influence on hydroxyapatite crystallization. *J. Inorg. Biochem.* **49**, 69–78 (1993).
  182. Eichert, D., Combes, C., Drouet, C. & Rey, C. Formation and Evolution of Hydrated Surface Layers of Apatites. *Key Eng. Mater.* **284–286**, 3–6 (2005).
  183. Rey, C. *et al.* Nanocrystalline apatites in biological systems: Characterisation, structure and properties. *Materwiss. Werksttech.* **38**, 996–1002 (2007).
  184. Boanini, E., Gazzano, M. & Bigi, A. Ionic substitutions in calcium phosphates synthesized at low temperature. *Acta Biomater.* **6**, 1882–1894 (2010).
  185. Vormann, J. Magnesium: nutrition and metabolism. *Mol. Aspects Med.* **24**, 27–37 (2003).
  186. Jahnen-Dechent, W. & Ketteler, M. Magnesium basics. *CKJ Clin. Kidney J.* **5**, (2012).
  187. Lagier, R. & Baud, C. a. Magnesium whitlockite, a calcium phosphate crystal of special interest in pathology. *Pathol. Res. Pract.* **199**, 329–335 (2003).
  188. Dorozhkin, S. V. Nanosized and nanocrystalline calcium orthophosphates. *Acta Biomater.* **6**, 715–34 (2010).
  189. LeGeros, R. Z., Sakae, T., Bautista, C., Retino, M. & LeGeros, J. P. Magnesium and carbonate in enamel and synthetic apatites. *Adv. Dent. Res.* **10**, 225–31 (1996).
  190. Johnsson, M. S. & Nancollas, G. H. The role of brushite and octacalcium phosphate in apatite formation. *Crit. Rev. Oral Biol. Med.* **3**, 61–82 (1992).
  191. Damaghi, M., Wojtkowiak, J. W. & Gillies, R. J. pH sensing and regulation in cancer. *Front. Physiol.* **4**, 370 (2013).
  192. Dalconi, M. C., Meneghini, C., Nuzzo, S., Wenk, R. & Mobilio, S. Structure of bioapatite in human foetal bones: An X-ray diffraction study. *Nucl. Instruments Methods Phys. Res. Sect. B Beam Interact. with Mater. Atoms* **200**, 406–410 (2003).
  193. Handschin, R. G. & Stern, W. B. X-ray diffraction studies on the lattice perfection of human bone apatite (Crista Iliaca). *Bone* **16**, S355–S363 (1995).

194. Astala, R. & Stott, M. J. First principles investigation of mineral component of bone: CO<sub>3</sub> substitutions in hydroxyapatite. *Chem. Mater.* **17**, 4125–4133 (2005).
195. Peroos, S., Du, Z. & de Leeuw, N. H. A computer modelling study of the uptake, structure and distribution of carbonate defects in hydroxy-apatite. *Biomaterials* **27**, 2150–61 (2006).
196. Legeros, R. Z., Trautz, O. R., Legeros, J. P., Klein, E. & Shirra, W. P. Apatite crystallites: effects of carbonate on morphology. *Science* **155**, 1409–11 (1967).
197. Fleet, M. E., Liu, X., King, P. L., Cap, A. & Ochap, C.-. Accommodation of the carbonate ion in apatite: An FTIR and X-ray structure study of crystals synthesized at 2–4 GPa. *Am. Mineral.* **89**, 1422–1432 (2004).
198. Zyman, Z. Z. & Tkachenko, M. V. Sodium-carbonate co-substituted hydroxyapatite ceramics. *Process. Appl. Ceram.* **7**, 153–157 (2013).
199. Fleet, M. E. & Liu, X. Coupled substitution of type A and B carbonate in sodium-bearing apatite. *Biomaterials* **28**, 916–26 (2007).
200. Fleet, M. E. Infrared spectra of carbonate apatites: Evidence for a connection between bone mineral and body fluids. *Am. Mineral.* **102**, 149–157 (2017).
201. Pasteris, J. D. *et al.* Lack of OH in nanocrystalline apatite as a function of degree of atomic order: Implications for bone and biomaterials. *Biomaterials* **25**, 229–238 (2004).
202. Kasem, M. A., Gonzalez, J. J., Russo, R. E. & Harith, M. A. LIBS analysis of artificial calcified tissues matrices. *Talanta* **108**, 53–58 (2013).
203. Samek, O. *et al.* Quantitative laser-induced breakdown spectroscopy analysis of calcified tissue samples. *Spectrochim. Acta - Part B At. Spectrosc.* **56**, 865–875 (2001).
204. Hamzaoui, S., Khleifia, R., Jaïdane, N. & Ben Lakhdar, Z. Quantitative analysis of pathological nails using laser-induced breakdown spectroscopy (LIBS) technique. *Lasers Med. Sci.* **26**, 79–83 (2011).
205. El-Hussein, A., Kassem, A. K., Ismail, H. & Harith, M. A. Exploiting LIBS as a spectrochemical analytical technique in diagnosis of some types of human malignancies. *Talanta* **82**, 495–501 (2010).
206. Ghasemi, F., Parvin, P., Hosseini Motlagh, N. S., Amjadi, A. & Abachi, S. Laser induced breakdown spectroscopy and acoustic response techniques to discriminate healthy and cancerous breast tissues. *Appl. Opt.* **55**, 8227 (2016).
207. Cuartero, M., Ruiz, A., Oliva, D. J. & Ortuño, J. A. Multianalyte detection using potentiometric ionophore-based ion-selective electrodes. *Sensors Actuators B Chem.* **243**, 144–151 (2017).
208. Hu, J., Stein, A. & Bühlmann, P. Rational design of all-solid-state ion-selective electrodes and reference electrodes. *TrAC - Trends Anal. Chem.* **76**, 102–114 (2016).

209. Ebrahim, L., Dissanayake, D., Metcalf, C. & Wylie, E. Screen-detected breast carcinoma with macroscopic dystrophic calcification: A pictorial essay with radiological pathological correlation. *J. Med. Imaging Radiat. Oncol.* **60**, 216–23 (2016).
210. Johns, P. C. & Yaffe, M. J. X-ray characterisation of normal and neoplastic breast tissues. *Phys. Med. Biol.* **32**, 675–95 (1987).



## Appendix A Processed Data

### A.1 XRD Summary aggregated by calcification

Spec.	Calc.	Diagnosis	Lattice parameters /Å		Whitlockite fraction	Coherently diffracting domain size / nm	
			c	a		H	D
X44	Calc 1	Benign	6.86843	9.46171	0.326%	15.91	10.26
X44	Calc 2	Benign	6.87077	9.45310	0.388%	16.34	10.22
X45	Calc 1	In-Situ	6.88030	9.43153	0.503%	18.28	11.91
X45	Calc 2	In-Situ	6.88621	9.43238	0.868%	21.68	13.92
X45	Calc 3	In-Situ	6.88854	9.44213	1.482%	16.49	15.10
X46	Calc 1a	Invasive	6.89079	9.42934	1.023%	22.77	16.07
X46	Calc 1b	Invasive	6.88482	9.43230	0.919%	21.67	15.15
X46	Calc 2	Invasive	6.89058	9.42360	1.048%	26.22	18.43
X46	Calc 3	Invasive	6.87955	9.43028	0.684%	19.59	13.39
X46	Calc 4	Invasive	6.89510	9.41955	1.268%	25.38	18.20
X46	Calc 5	Invasive	6.88761	9.42726	0.798%	20.82	13.42
X46	Calc 6	Invasive	6.89618	9.41662	0.814%	20.43	14.60
X47	Calc 1	Invasive	6.88802	9.43268	1.868%	19.09	13.68
X47	Calc 2	Invasive	6.88354	9.43206	2.191%	16.58	14.61
X47	Calc 3	Invasive	6.89206	9.43091	NA	NA	NA
X47	Calc 4	Invasive	6.89190	9.43160	1.473%	17.36	11.82
X48	Calc 1	Benign	6.87524	9.44294	0.284%	11.78	11.26
X48	Calc 2	Benign	6.86580	9.44020	0.854%	12.51	11.22
X49	Calc 1	In-Situ	6.88258	9.43016	1.349%	16.86	13.25
X49	Calc 2	In-Situ	6.87777	9.44495	0.374%	13.35	11.12
X49	Calc 3	In-Situ	6.87490	9.43103	0.279%	18.00	11.43
X49	Calc 4	In-Situ	6.88506	9.42698	2.102%	14.89	16.05
X49	Calc 5	In-Situ	6.87618	9.43282	0.656%	17.63	11.69
X49	Calc 6	In-Situ	6.87438	9.44731	0.459%	18.47	11.66
X49	Calc 7	In-Situ	6.88751	9.43151	3.151%	24.96	16.29
X50	Calc 1a	Invasive	6.88713	9.41062	0.868%	23.65	16.27
X50	Calc 1b	Invasive	6.89724	9.41638	1.545%	28.67	17.63
X50	Calc 2	Invasive	6.88962	9.41256	0.566%	19.89	14.32
X51	Calc 1	Benign	6.86702	9.44490	1.013%	18.83	10.40
X51	Calc 2	Benign	6.87056	9.45599	0.679%	15.46	9.28
X51	Calc 3	Benign	6.87129	9.45849	0.470%	14.67	9.26
X52	Calc 1	Invasive	6.87652	9.45117	1.151%	18.98	11.38
X52	Calc 2	Invasive	6.87698	9.43628	0.312%	18.78	11.89
X52	Calc 3	Invasive	6.87408	9.45148	0.367%	20.06	11.82
X52	Calc 4	Invasive	6.88021	9.43864	0.326%	18.62	11.73

X53	Calc 1	In-Situ	6.88600	9.42616	0.905%	19.96	13.83
X53	Calc 2	In-Situ	6.86963	9.43537	0.724%	16.72	11.57
X54	Calc 1	Invasive	6.88414	9.44075	1.054%	19.99	13.78
X54	Calc 2	Invasive	6.88531	9.44135	0.673%	20.85	15.65
X54	Calc 3	Invasive	NA	NA	3.096%	NA	NA
X55	Calc 1	Benign	6.89028	9.43335	0.815%	20.51	18.11
X55	Calc 2	Benign	6.89042	9.41657	0.723%	22.64	16.26
X55	Calc 3	Benign	6.87286	9.42678	0.468%	18.44	12.27
X55	Calc 4	Benign	6.89343	9.42128	0.671%	27.94	15.07
X55	Calc 5	Benign	6.88754	9.43390	0.286%	16.85	10.55
X55	Calc 6	Benign	6.88198	9.43320	0.406%	22.07	12.80
X56	Calc 2	Invasive	6.88217	9.43308	0.382%	20.19	12.62
X56	Calc 3	Invasive	6.88541	9.43002	0.856%	23.58	15.78
X57	Calc 1	In-Situ	6.88628	9.42603	0.779%	22.10	13.67
X57	Calc 2	In-Situ	6.88961	9.42303	1.413%	24.15	15.52
X57	Calc 3	In-Situ	6.89103	9.42153	1.068%	23.53	15.13
X57	Calc 4	In-Situ	6.89444	9.41933	0.904%	26.02	16.82
X58	Calc 1	Benign	6.87215	9.44768	0.332%	15.86	10.60
X58	Calc 2	Benign	6.86941	9.44911	0.266%	16.33	10.94
X58	Calc 3	Benign	6.87855	9.43849	0.077%	15.02	10.41
X58	Calc 4	Benign	6.87888	9.43288	0.177%	16.05	10.99



## A.2 EDS summary aggregated by calcification

Specimen	Calc	Diagnosis	Spectra	Mg:Ca			Ca:P			Na:Ca		
				Median	L 95% CI	U 95% CI	Median	L 95% CI	U 95% CI	Median	L 95% CI	U 95% CI
S43	Calc1	In-Situ	43	0.018072	0.015690	0.019278	1.7671	1.7350	1.7869	0.028797	0.026308	0.030023
S44	Calc1	Benign	28	0.022179	0.018344	0.026424	1.7108	1.6597	1.7770	0.025773	0.020558	0.030847
S44	Calc2	Benign	30	0.024192	0.021852	0.026755	1.6621	1.6145	1.7229	0.029700	0.024645	0.035815
S45	Calc1	In-Situ	42	0.025125	0.023139	0.026893	1.6726	1.6345	1.7313	0.046824	0.036360	0.057301
S45	Calc2	In-Situ	31	0.022076	0.018919	0.023830	1.6046	1.5682	1.6170	0.064742	0.058031	0.074476
S45	Calc3	In-Situ	20	0.023854	0.017232	0.025984	1.6281	1.5832	1.7223	0.058439	0.041921	0.067050
S45	Calc4	In-Situ	26	0.023362	0.021884	0.024826	1.5855	1.5543	1.6240	0.059910	0.051642	0.068704
S46	Calc1	Invasive	60	0.014720	0.012875	0.015898	1.6808	1.6526	1.7274	0.057379	0.053764	0.061062
S46	Calc2	Invasive	55	0.013913	0.012464	0.014577	1.6971	1.6653	1.7295	0.054727	0.045680	0.061547
S46	Calc3	Invasive	63	0.018528	0.014787	0.019299	1.7316	1.6839	1.7676	0.050751	0.042707	0.055360
S47	Calc1	Invasive	105	0.011137	0.009431	0.012904	1.8962	1.7894	1.9889	0.034632	0.029636	0.038570
S47	Calc2	Invasive	128	0.014238	0.013167	0.015228	1.7812	1.7540	1.8241	0.042943	0.037820	0.047975
S47	Calc3	Invasive	114	0.010835	0.009853	0.011940	1.8356	1.8028	1.8730	0.043555	0.040781	0.048584
S47	Calc4	Invasive	178	0.013425	0.012607	0.014682	1.8037	1.7732	1.8319	0.033999	0.030153	0.036462
S48	Calc1to2	Benign	50	0.025824	0.023921	0.026942	1.7389	1.7152	1.7811	0.035955	0.030481	0.039366
S49	Calc1	In-Situ	21	0.013404	0.008750	0.014833	1.8412	1.6817	1.8540	0.035686	0.026284	0.048148
S49	Calc2	In-Situ	20	0.015509	0.012105	0.017333	1.7068	1.6490	1.8689	0.044727	0.035252	0.053576
S49	Calc3	In-Situ	17	0.013767	0.004355	0.017528	1.6139	1.5409	1.7221	0.062445	0.036419	0.083936
S49	Calc4	In-Situ	11	0.012243	0.002538	0.018398	1.6597	1.5293	1.7934	0.046423	0.028352	0.061004
S49	Calc7	In-Situ	22	0.009096	0.006435	0.012014	1.7996	1.7463	1.8324	0.034747	0.029750	0.038355

S50	Calc1	Invasive	22	0.017678	0.013027	0.023586	1.7239	1.6620	1.7755	0.066746	0.057056	0.081865
S51	Calc1	Benign	39	0.026299	0.022958	0.028864	1.6926	1.6249	1.7436	0.025812	0.020898	0.029769
S51	Calc2	Benign	23	0.025421	0.021581	0.027280	1.7247	1.6717	1.7416	0.029683	0.023705	0.034279
S51	Calc3	Benign	23	0.023047	0.020647	0.025920	1.7783	1.6673	1.9254	0.026335	0.019588	0.031696
S52	Calc1	Invasive	163	0.028205	0.023193	0.030091	1.7171	1.6865	1.7707	0.033993	0.030131	0.037122
S52	Calc2	Invasive	97	0.052332	0.043490	0.057960	1.6242	1.5889	1.6560	0.045580	0.040852	0.050097
S52	Calc3	Invasive	86	0.030092	0.027095	0.033724	1.6094	1.5829	1.6397	0.058323	0.052459	0.065676
S52	Calc4	Invasive	112	0.031866	0.028791	0.035211	1.6344	1.5920	1.7024	0.062783	0.053424	0.070151
S53	Calc3	In-Situ	44	0.023398	0.020439	0.024669	1.6662	1.6380	1.7105	0.051580	0.046026	0.054607
S54	Calc1	Invasive	43	0.018174	0.016160	0.019359	1.6417	1.6127	1.6822	0.061773	0.057173	0.065231
S54	Calc2	Invasive	23	0.025242	0.019011	0.025817	1.5424	1.5122	1.5707	0.069862	0.055822	0.086196
S55	Calc1to4	Benign	29	0.013181	0.011625	0.014923	1.6517	1.6107	1.6921	0.031930	0.025968	0.033801
S55	Calc5	Benign	63	0.007952	0.006620	0.009241	1.5782	1.5315	1.6240	0.060646	0.056169	0.067791
S55	Calc6	Benign	15	0.021717	0.018381	0.023938	1.5918	1.4324	1.6437	0.044012	0.033802	0.075313
S56	CalcCluster	Invasive	45	0.018210	0.015894	0.019154	1.6126	1.5715	1.6446	0.061122	0.057712	0.067301
S57	Calc1	In-Situ	43	0.012308	0.011238	0.013285	1.8234	1.7647	1.8728	0.028773	0.026304	0.032594
S57	Calc2	In-Situ	54	0.012955	0.011336	0.013710	1.7740	1.7299	1.7939	0.034479	0.028417	0.037515
S57	Calc3	In-Situ	27	0.012931	0.009802	0.014714	1.7197	1.6551	1.7918	0.030621	0.024171	0.040122
S57	Calc4	In-Situ	40	0.009862	0.007968	0.011737	1.8100	1.7285	1.8525	0.031270	0.026005	0.038055
S58	Calc1	Benign	34	0.016949	0.012806	0.019169	1.8598	1.8073	1.9996	0.026724	0.018006	0.027476
S58	Calc2	Benign	31	0.024244	0.019454	0.028538	1.7501	1.6885	1.8266	0.033525	0.023031	0.036034
S58	Calc3	Benign	25	0.023602	0.015065	0.026267	1.7363	1.6840	1.9645	0.027124	0.021235	0.034897
S58	Calc4	Benign	19	0.022873	0.017718	0.023965	1.7664	1.6834	1.8381	0.036701	0.028948	0.040956
S59	Calc1	Invasive	16	0.011549	0.009147	0.014186	1.9234	1.8112	1.9772	0.049192	0.042616	0.059591
S59	Calc2	Invasive	24	0.014976	0.012676	0.018416	1.8087	1.6992	1.9109	0.062612	0.044163	0.070866
S62	Site 10	Invasive	31	0.015593	0.009936	0.017166	1.6821	1.6429	1.7408	0.051725	0.037091	0.053657
S63	Cluster1	Invasive	16	0.018538	0.015995	0.020678	1.7313	1.6849	1.7546	0.041347	0.037737	0.051396

S63	Cluster2	Invasive	44	0.017827	0.015902	0.018493	1.7397	1.7089	1.7621	0.045183	0.042135	0.048485
S64	Calc1	Benign	16	0.006468	0.003994	0.008578	1.7124	1.6382	1.8074	0.035750	0.025339	0.040191
S65	Calc1	In-Situ	14	0.011649	0.008264	0.013125	1.5695	1.5590	1.5791	0.067346	0.060663	0.072398
S65	Cluster1	In-Situ	16	0.016180	0.012411	0.019230	1.6556	1.5720	1.6838	0.055667	0.046366	0.060618
S66	Calc1	Invasive	26	0.021120	0.018641	0.022844	1.6739	1.6419	1.7065	0.063487	0.057581	0.069405
S66	Calc2	Invasive	27	0.010543	0.006970	0.019693	41.6275	1.7952	66.1976	0.013337	0.007336	0.042081
S66	Calc3	Invasive	12	0.020055	0.015381	0.022201	1.7784	1.7258	1.8414	0.046552	0.035066	0.049002
S67	Calc1b	Benign	23	0.005093	0.004257	0.006856	1.7067	1.6816	1.7842	0.056148	0.052876	0.062978
S68	Calc1	Invasive	20	0.019962	0.018992	0.023316	1.6304	1.5937	1.6897	0.048641	0.041544	0.054559
S68	Calc2	Invasive	11	0.008885	0.005561	0.011302	1.6257	1.4541	1.7559	0.060348	0.036638	0.074534
S69	Calc1	In-Situ	25	0.013427	0.009809	0.016379	1.7110	1.5478	1.7864	0.061348	0.049767	0.081015
S70	Calc1	Invasive	36	0.039323	0.030072	0.045177	1.6599	1.5592	1.7462	0.042178	0.034069	0.050083
S70	Calc2	Invasive	17	0.035154	0.029737	0.042557	1.5978	1.5374	1.6819	0.046457	0.030143	0.050493
S70	Calc2b	Invasive	35	0.034891	0.028944	0.037422	1.6936	1.5836	1.7355	0.040004	0.028362	0.043495
S71	Calc1	Benign	26	0.011585	0.009723	0.013298	1.7423	1.6915	1.8021	0.049278	0.040164	0.056581
S72	Calc1	Invasive	42	0.014758	0.012284	0.016057	1.8917	1.8265	1.9604	0.028787	0.025797	0.029969
S73	Calc1	In-Situ	72	0.019238	0.018298	0.020347	1.6842	1.6703	1.6943	0.042693	0.038281	0.045348
S74	Calc1	Benign	32	0.028901	0.023048	0.031089	1.6526	1.6160	1.6892	0.032627	0.026906	0.034143
S75	Calc1	Invasive	44	0.020341	0.016418	0.021840	1.6326	1.6012	1.6925	0.062747	0.055546	0.073652



## Appendix B Pathology summaries

Note: Specimens for the EDS study were mounted on an SEM stub, and are prefixed with “S”. The adjacent slices for the x-ray diffraction study were mounted on polyolefin film and prefixed “X”.

Specimen	Histological Opinion	Micro. Report: Summary extract
S43	B5a	All three cores contain intermediate and high nuclear grade solid-type ductal carcinoma in-situ (DCIS) associated with some comedo necrosis and malignant microcalcification. There is cancerisation of lobules also present. There are some areas concerning for invasive malignancy but a definitive diagnosis cannot be made at this time. Immunohistochemistry will be carried out to see if this can be taken any further. At this time, the most appropriate categorisation is one of B5a. Immunohistochemistry has been carried out and the areas of DCIS show rimming by myoepithelial cells. There is no definitive diagnosis of invasion and therefore the categorisation of B5a stands. Oestrogen receptor shows the DCIS to be strongly oestrogen receptor positive giving a quick score, if appropriate, of 8/8.
S44	B2	Fibroadipose breast tissue including a fibroadenoma. Dystrophic calcification is noted within the fibroadenoma. There is no cytological atypia.
S45	B5a	Intermediate and high nuclear grade DCIS associated with malignant microcalcification. DCIS shows solid cribriform and papillary growth patterns. There is no evidence of invasive malignancy.

S46	B5b	High nuclear grade DCIS associated with malignant microcalcification and invasive ductal carcinoma which appears to be moderately differentiated. Immunohistochemistry for oestrogen receptors demonstrates that more than 67% of neoplastic cells of this tumour show strong nuclear positivity, giving a Quick score of 8/8.
S47	B5b	These fragments of breast tissue bear infiltrating carcinoma, on this evidence moderately differentiated ductal carcinoma comprising cohesive nests and cords of cells infiltrating hyalinised fibroelastotic stroma. The tumour does show some lobular features. In addition there is high nuclear grade DCIS of solid and cribriform types with comedo necrosis and associated malignant calcification. Immunostaining for oestrogen receptors shows the tumour to be strongly ER positive (quick score 8/8). The tumour is E-Cadherin positive supporting the diagnosis of ductal carcinoma.
S48	B2	These biopsies are of breast tissue showing dense stromal sclerosis associated with coarse calcification which appears dystrophic. The epithelial elements show columnar cell change and mild usual type hyperplasia. There is no evidence of atypia or of in-situ or invasive malignancy in these biopsies.
S49	B5a	These breast core biopsies show intermediate nuclear grade ductal carcinoma in-situ of cribriform type with apocrine features. There is associated malignant microcalcification. There is no evidence of invasion in these biopsies.
S50	B5b	Cores of sclerotic and elastotic stroma which are infiltrated by a ductal carcinoma. The tumour appears well differentiated with well formed ducts lined by bland epithelial cells. There is much micro-calcification associated with the lesion and a small in-situ component is also present. Immunohistochemistry shows strong nuclear positivity in almost all tumour cells for oestrogen receptor giving a Quick score of 8/8.

S51	B2	The specimen comprises rather fragmented cores of benign breast tissue exhibiting a normal tubulo-lobular architecture with quite marked hyaline fibrosis of the stroma. There is some evidence of fibrosis of the intra-lobular stroma suggesting some fibrocystic change but some of the fragments show fibroadenomatoid features comprising expanded hyaline hypocellular stroma within which, there are some curvilinear compressed ducts. This fibroadenomatoid tissue is associated with large foci of micro-calcification. Although appearances may represent fibroadenomatoid change, part of a fibroadenoma is also a possibility. There is no evidence of malignancy.
S52	B5b	These core biopsies are infiltrated by a well differentiated ductal carcinoma (T1 P2 M2). There is associated microcalcification and focal DCIS. Immunohistochemistry for oestrogen receptors demonstrates that more than 67% of neoplastic cells of this tumour show strong nuclear positivity, giving a Quick score of 8/8.
S53	B5a	Histological assessment reveals that both specimens consist of cores of breast tissue within which there is high nuclear grade ductal carcinoma in-situ with a solid growth pattern associated with comedo necrosis and malignant micro-calcification. In areas, this has the features more in keeping with pleomorphic lobular carcinoma in-situ (LCIS) but, from a management point of view, should be regarded as DCIS. There is a some scarring and inflammation associated with some of the ducts but there is no definite evidence of invasive malignancy, although, in specimen 2, is this more concerning and immunohistochemistry will be carried out and a supplementary report will be issued. SUPPLEMENTARY: Immunohistochemistry has been carried out. There is no evidence of invasive malignancy. The in-situ component is negative for E-cadherin. This is considered to pleomorphic lobular carcinoma in-situ (LCIS). From a management point of view, it should be treated as for DCIS. The categorisation of B5a remains.

S54	B5b	A core of desmoplastic fibro-elastotic stroma bearing infiltrating adenocarcinoma, on this evidence moderate to poorly differentiated ductal carcinoma. Some probable high nuclear grade DCIS showing comedo necrosis is seen and there is malignant calcification. Immunostaining for oestrogen receptors has been performed (1) revealing the tumour to be strongly ER positive (quick score 8/8).
S55	B2	Stereo-cores right breast, representative calcs seen: This specimen comprises benign breast tissue exhibiting a normal tubulo-lobular architecture. There are well established fibrocystic changes with areas of fibrosis of the inter and intra-lobular stroma with dilatation and separation of acini. Apocrine and lactational type change is seen and in some areas, there is columnar cell change associated with benign micro-calcification. There is some cross cutting of the ducts. The specimen has been examined on multiple levels and neither in-situ nor infiltrating neoplasia is seen.
S56	B5b	This core biopsy shows a grade 1 infiltrating ductal carcinoma, not otherwise specified (tubules 1, pleomorphism 2, mitosis 1). Malignant microcalcifications are seen. There is no convincing DCIS. ER Quick score is 7/8 (5 + 2).
S57	B5a	1 and 2: Biopsies from both sites consist of breast tissue showing similar features with intermediate nuclear grade ductal carcinoma in-situ showing apocrine features. There is associated comedo necrosis with malignant microcalcification. There is no evidence of invasive malignancy in either specimen.
S58	B2	These core biopsies show features of fibrocystic change with many areas of sclerosing adenosis and focal benign microcalcification. There is no evidence of epithelial hyperplasia, in situ or invasive malignancy.
S59	B5b	Contains infiltrating ductal carcinoma, poorly differentiated, Grade 3 (tubules 3, pleomorphism 3, mitoses 2). There is no definite in-situ component but there is both necrosis and malignant calcification present. ER quick score of 7/8.



S62	B5b	Comprises cores of breast tissue bearing infiltrating carcinoma, on this evidence moderately differentiated ductal carcinoma. The parenchyma bears a chronic inflammatory infiltrate and there is an intra-ductal flat and largely columnar cell proliferation showing variable atypia that in areas is considered to represent flat intermediate to high grade DCIS. Stromal micro-calcification is also seen. Immunostaining for oestrogen receptors shows the tumour to be ER positive (Quick score 7/8).
S63	B5b	A core of fibroadipose breast tissue. There is marked stromal sclerosis within which there are breast structures that show some cystic change. Microcalcification is seen. One of the ducts is markedly dilated and another one shows columnar cell change. Within the sclerotic stroma there are two or three epithelial profiles with nuclear enlargement. This develops into a small focus of invasive ductal carcinoma on the deeper levels. Approximately half of the tumour cell nuclei are strongly positive for oestrogen receptors. Quick score 7/8.
S64	B2	Cores of breast tissue showing fibrocystic change with some cystically dilated ducts, others that show columnar cell change and a stroma that shows hyalinosis in places. Benign microcalcification is seen in some of the dilated ducts.
S65	B5a	These breast core biopsies show high nuclear grade ductal carcinoma in-situ of solid type with comedo necrosis and malignant microcalcification. There is no evidence of invasive malignancy.
S66	B5b	These are cores of fibro-adipose connective tissue which show widespread infiltration by a poorly differentiated carcinoma with ductal morphology. In this material the tumour appears to be grade 3 (T3 P3 M2). No conspicuous in-situ component is noted. Oestrogen receptor status is very weakly positive with only a small proportion of cells showing weak staining (Quick score 2/8).

S67	B2	Tissue fragments comprising haemorrhagic adipose tissue together with breast tissue showing sclerotic stroma within which are benign ducts and lobules. Calcified material is seen associated with sclerotic stroma. A small amount of epidermis is also present. No other lesion is identified. Some dilated ducts are present on deeper levels and the appearances raise the possibility of sampling from an area of fibrocystic change. There is some calcification associated with these cystically dilated ducts. The appearances in this biopsy can be regarded as benign.
S68	B5b	Cores of breast parenchyma bearing focally necrotic infiltrating carcinoma, on this evidence poorly differentiated ductal carcinoma. There is high nuclear grade DCIS of micropapillary type with comedo necrosis. Immuno staining for oestrogen receptors shows the tumour to be strongly ER positive (Quick score 8/8).
S69	B5a	Intermediate nuclear grade ductal carcinoma in-situ showing apocrine features. There is associated comedo necrosis with malignant microcalcification. There is no evidence of invasive malignancy.
S70	B5b	These core biopsies are infiltrated by a tumour composed of angulated tubules set in a desmoplastic stroma. This tumour is likely to be a grade 1 tubular carcinoma (tubules 1, pleomorphism 2, mitosis 1). Malignant micro-calcifications are seen. There is no DCIS. Oestrogen receptor immunohistochemistry shows strong nuclear staining in all tumour cells. ER Quick score is 8/8 (5+3).
S71	B2	Fragmented pieces of fibrofatty breast tissue plus some clot. There is evidence of fibrocystic change and columnar cell change and in one area, an aggregate of slightly ectatic separated acini are associated with benign calcification. Although one duct, in the most superficial levels shows some architectural complexity, this is considered an artefact due to cross cutting. The stromal collagen appears slightly fibrillary in areas but established elastosis is not seen. Neither in-situ nor infiltrating neoplasia is identified and a B2 diagnosis is considered appropriate.

S72	B5b	These core biopsies are widely infiltrated by a moderately differentiated ductal carcinoma exhibiting modified Bloom Richardson grade 2 features (T2 P2 M2). The tumour is associated with malignant microcalcification. There is no in-situ component identified in these biopsies. Immunohistochemistry shows strong nuclear positivity in almost all tumour cells for oestrogen receptor, giving a Quick score of 8/8.
S73	B5a	These core biopsies show foci of ductal carcinoma-in-situ exhibiting central comedo necrosis and malignant microcalcification. DCIS shows intermediate nuclear grade features. No evidence of invasive malignancy is seen in these core biopsies.
S74	B2	These breast core biopsies show dense stromal sclerosis with benign microcalcification and some features on deeper levels of previous fat necrosis. The deepest level includes a cluster of cells within the fat which may be macrophages in association with the fat necrosis. Immunohistochemistry has been performed and overall histological appearances are regarded as those of fibrocystic change with possible minimal focal fat necrosis and no atypical or neoplastic features.
S75	B5b	Cores contain infiltrating carcinoma which, on this evidence, is a classical lobular carcinoma which is moderately differentiated equating to a modified Bloom and Richardson grade of grade 2 (tubules 3, pleomorphism 2, mitoses 1) and is associated with lobular carcinoma in situ (LCIS) and malignant microcalcification. Immunohistochemistry for oestrogen receptor shows moderate and focally strong staining in the vast majority of infiltrating carcinoma cells giving a Quick score of 7/8.



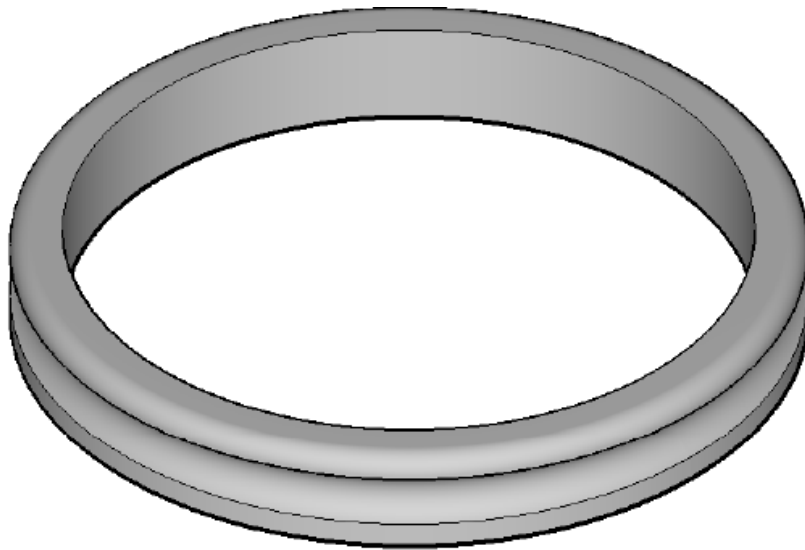
## Appendix C Hydroxyapatite X-ray diffraction lines

Relative intensity and d spacings are from the certificate of analysis for NIST Standard Reference Material 2910b Hydroxyapatite.  $\Phi$  = Angle between lattice plane normal and 'c' axis, based on lattice parameters for NIST 2910b.

hkℓ	I (relative)	d (nm)	2 $\theta$ (Cu K $\alpha$ )	2 $\theta$ (10 keV)	$\phi$
100	10	0.8160	10.83	8.71	90.00
101	3	0.5264	16.83	13.53	40.16
110	2	0.4711	18.82	15.12	90.00
200	6	0.4080	21.77	17.48	90.00
111	5	0.3889	22.85	18.34	55.62
201	2	0.3511	25.35	20.34	59.35
002	34	0.3444	25.85	20.74	0.00
102	8	0.3173	28.10	22.53	22.87
210	15	0.3084	28.93	23.19	90.00
211	100	0.2815	31.76	25.44	65.87
112	48	0.2780	32.17	25.77	36.16
300	60	0.2720	32.90	26.35	90.00
202	21	0.2632	34.04	27.25	40.16
301	4	0.2530	35.45	28.37	68.44
212	6	0.2298	39.18	31.30	48.14
310	22	0.2263	39.80	31.80	90.00
221	2	0.2229	40.44	32.29	71.11
311	6	0.2150	41.99	33.52	71.80
302	1	0.2135	42.31	33.76	51.69
113	5	0.2064	43.83	34.96	25.97
400	1	0.2040	44.37	35.38	90.00
203	4	0.2001	45.28	36.09	29.36
222	28	0.1944	46.68	37.19	55.62
312	20	0.1891	48.07	38.27	56.68
320	4	0.1872	48.59	38.68	90.00
213	30	0.1842	49.45	39.33	36.65
321	15	0.1807	50.48	40.13	74.79
410	11	0.1781	51.26	40.74	90.00
402	12	0.1755	52.06	41.37	59.35
004	13	0.1722	53.14	42.20	0.00
104	1	0.1685	54.41	43.17	11.91
322	6	0.1645	55.85	44.28	61.46
313	4	0.1612	57.10	45.23	45.40
501	2	0.1588	58.03	45.95	76.66
412	1	0.1582	58.28	46.14	62.65
330	1	0.1570	58.75	46.51	90.00
420	4	0.1542	59.93	47.41	90.00

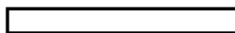


## Appendix D XRD Fixture drawings



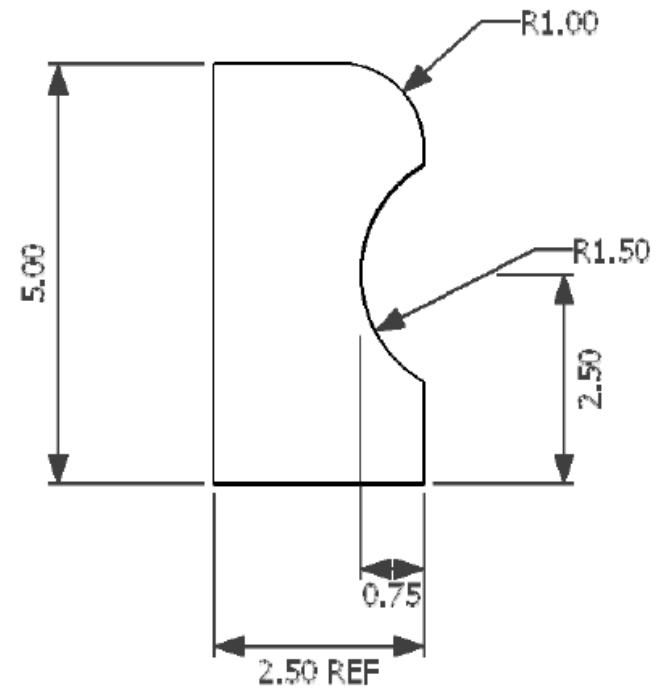
### Polyethylene film carrier rings

Robert Scott  
PhD Student



robert.scott@cranfield.ac.uk

Material: Aluminium alloy tubing  
OD 38mm or 1.5", Wall 2.5mm to 1/8"  
Dimensions in mm  
All dims  $\pm 0.2$ mm UOS  
Finish: machined UOS  
Quantity: 30



For use with 3mm Section 34mm Bore  
VITON Rubber O-Rings



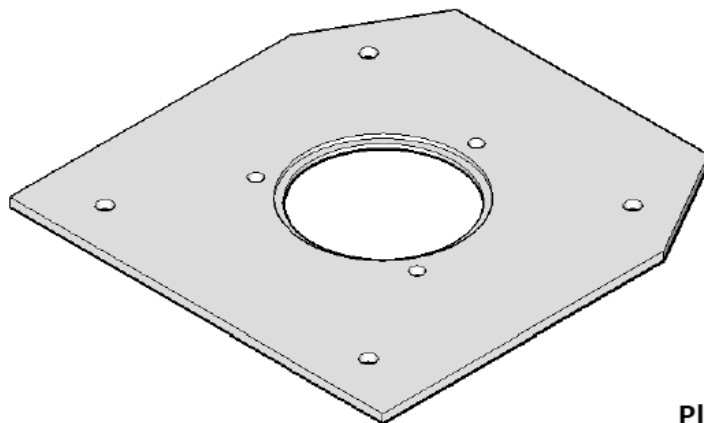
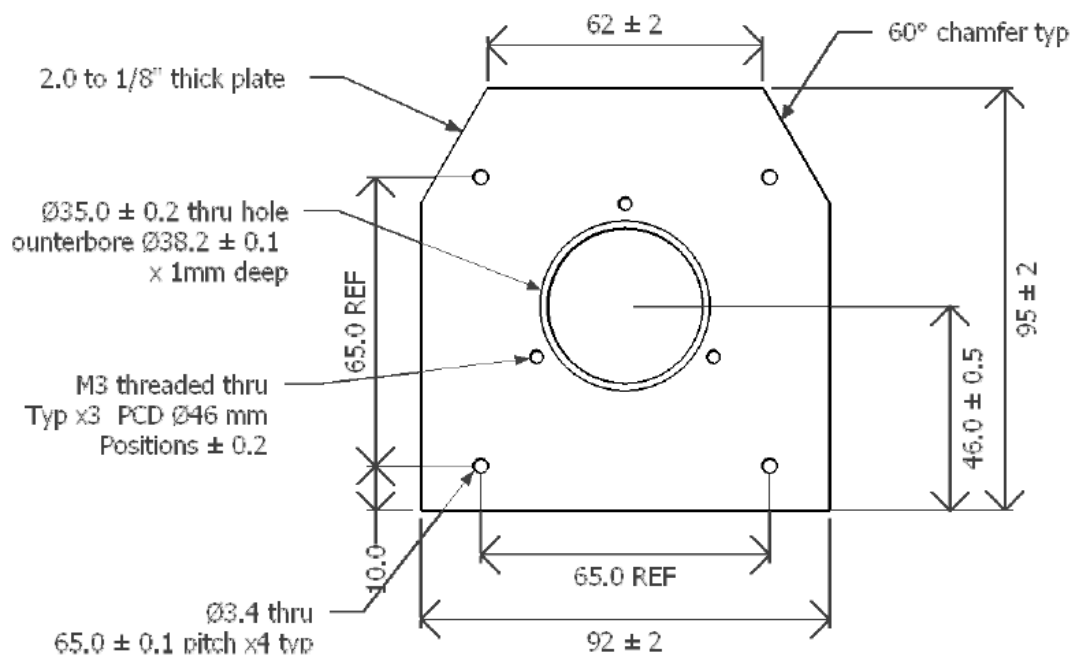


### Plate for film carrier rings

Robert Scott  
PhD Student

robert.scott@cranfield.ac.uk

Material: Aluminium alloy sheet  
Dimensions in mm  
All dims ±0.5mm UOS  
Finish: machined  
Quantity: 1

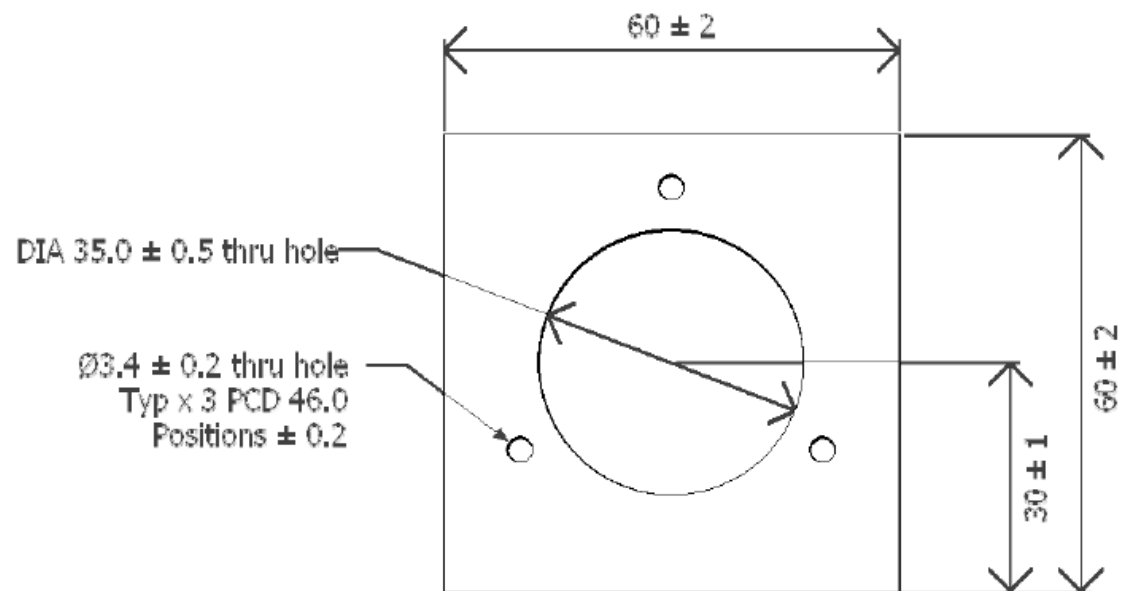


Plate for film carrier rings - Part 2 of 2

Robert Scott  
PhD student

robert.scott@cranfield.ac.uk

Material: Aluminium alloy sheet, approx 2 mm  
thick  
Dimensions in mm  
Finish: Machined

## Appendix E ImageJ Programs

This program processes CT scan output files from the CT Pro application (Nikon Metrology) of FFPE blocks with calcifications, and outputs six files:

File name (* = specimen ID)	Description
Reslice *.tif	Rotates and crops the volume so that slices are parallel to the surface of the wax blocks
Preprocessed *.tif	Brightness, contrast, and gamma adjusted. Reduced from 32 to 8 bit.
*-Slice x.tif	First complete slice selected at depth x.
*-Slice x markers.tif	Thresholded calcifications highlighted in red
Montage slices x to x+6 *.tif	Montage of first 6 complete slices
*.txt	Position coordinates of calcifications in first complete slice.

- //Input: .vol file and .vgi file from CT reconstruction
- //Pre-processing of vol file
- //Select file
- volFile = File.openDialog("Select .vol file");
- PreOrPost = getString("CT scan Post sectioning?", "n");
- if(PreOrPost=="y")
- PreOrPost="Post";
- else
- PreOrPost="Pre";
  
- //Read VGI file and extract voxel size
- vgiFile=replace(volFile, ".vol", ".vgi");
- filestring=File.openAsString(vgiFile);

```

➤ lines=split(filestring, "\n");
➤ for(i=1; i<lines.length; i++){
➤ if (lines[i-1]=="[representation]") {
➤     columns=split(lines[i], " ");
➤     sx=parseFloat(columns[2]);
➤     sy=parseFloat(columns[3]);
➤     sz=parseFloat(columns[4]);
➤ }
➤ if (lines[i-1]=="[resolution]") {
➤     columns=split(lines[i], "=");
➤     voxmm=parseFloat(columns[1]);
➤ }
➤ }

➤ //Import file
➤ run("Raw...", "open=volFile image=[32-bit Real] width=&sx
height=&sy offset=0 number=&sz gap=0 little-endian");
➤ //Set voxel size
➤ voxum=voxmm*1000;
➤ run("Properties...", "unit=um pixel_width=&voxum
pixel_height=&voxum voxel_depth=&voxum");

➤ volTitle=getTitle();
➤ volPath=File.directory;

➤ //Initial crop (unnecessary if CT reconstruction is of
limited volume)
➤ //setTool("rectangle");
➤ //waitForUser("Select rectangular region for rough crop");
➤ //run("Crop");

➤ //Straighten image

```

```

➤ setTool("line");
➤ setSlice(round(nSlices*0.25));
➤ waitForUser("Draw line along bottom of face");
➤ getSelectionCoordinates(xb, yb);
➤ x1=xb[0];
➤ y1=yb[0];
➤ x2=xb[1];
➤ y2=yb[1];
➤ xmb=(x1+x2)/2;
➤ ymb=(y1+y2)/2;
➤ z1=getSliceNumber();

➤ setSlice(round(nSlices*0.75));
➤ waitForUser("Draw line along top of face");
➤ getSelectionCoordinates(xt, yt);
➤ x3=xt[0];
➤ y3=yt[0];
➤ x4=xt[1];
➤ y4=yt[1];
➤ z3=getSliceNumber();
➤ angZb=-atan((y2-y1)/(x2-x1))*180/PI;
➤ angZt=-atan((y4-y3)/(x4-x3))*180/PI;
➤ angZ=(angZb+angZt)/2;
➤ xmt=xmb;
➤ ymt=y3+((xmt-x3)/(x4-x3))*(y4-y3);
➤ angX=atan((ymt-ymb)/(z3-z1))*180/PI;
➤ run("Select None");
➤ run("TransformJ Rotate", "z-angle=&angZ y-angle=0.0 x-
  angle=&angX interpolation=[cubic B-spline] background=0.0
  adjust");
➤ rotTitle=getTitle();

```

```

➤ //Reslice and recrop
➤ setSlice(round(nSlices*0.5));
➤ setTool("rectangle");
➤ waitForUser("Select rectangular region for recrop");
➤ dirChoice = getNumber("Reslice Direction: 1 for Top, 2 for
  Bottom", 2);
➤ if (dirChoice==1)
➤   direction="Top";
➤   else
➤   direction="Bottom";
➤ run("Crop");
➤ run("Reslice [/]...", "output=1.000 start=&direction
  avoid");
➤ setTool("rectangle");
➤ setSlice(round(nSlices*0.1));
➤ waitForUser("Select rectangular region to crop");
➤ run("Crop");
➤ resliceTitle=getTitle();
➤ run("Flip Horizontally", "stack");
➤ saveAs("Tiff",volPath+resliceTitle+PreOrPost+".tif");
➤ selectWindow(volTitle);
➤ close();
➤ selectWindow(rotTitle);
➤ close();

➤ //Adjust grey levels and reduce bit depth
➤ run("Gamma...", "value=0.50 stack"); // 0.5 is arbitrary,
  but visually appears the best
➤ numSlices=nSlices;

➤ // Find maximum intensity

```

```

➤ run("Z Project...", "start=1 stop=&numSlices
  projection=[Max Intensity]");

➤ // Get grey value of 10th from most intense pixel (avoids
  outliers)
➤ w = getWidth;
➤ h = getHeight;
➤ numpix=w*h;
➤ a = newArray(numpix);
➤ i = 0;
➤ for (y=0; y<h; y++)
➤   for (x=0; x<w; x++)
➤     a[i++] = getPixel(x,y);
➤ Array.sort(a);
➤ maxlim=a[numpix-11]
➤ close();

➤ //Find minimum intensity
➤ run("Z Project...", "start=1 stop=&numSlices
  projection=[Min Intensity]");
➤ b = newArray(numpix);
➤ i = 0;
➤ for (y=0; y<h; y++)
➤   for (x=0; x<w; x++)
➤     b[i++] = getPixel(x,y);
➤ Array.sort(b);
➤ minlim=b[9];
➤ close();
➤ min=minlim;
➤ max=maxlim;
➤ setMinAndMax(min, max);

```

```

➤ run("8-bit");
➤ resliceTitle=getTitle();
➤ reslicePath=File.directory;

➤ binTitle=replace(resliceTitle,"Reslice of ","Preprocessed
");
➤ binFile=reslicePath+binTitle;
➤ saveAs("Tiff",binFile);

➤ //Output positions of marker holes and calcifications
➤ inputPath=getDirectory("image");
➤ inputTitle=getTitle;
➤ waitForUser("Select top slice");
➤ slice=getSliceNumber();
➤ toslice=slice+5;
➤ run("Make Montage...", "columns=2 rows=3 scale=1
first=&slice last=&toslice increment=1 border=1 font=14
label");
➤ montageTitle=replace(inputTitle,"Preprocessed ","Montage
slices "+slice+" to "+toslice);
➤ montageFile=inputPath+montageTitle;
➤ saveAs("Tiff",montageFile);
➤ close();
➤ selectWindow(inputTitle);
➤ run("Make Montage...", "columns=1 rows=1 scale=1
first=&slice last=&slice increment=1 border=0 font=12");
➤ //Marker holes
➤ //setAutoThreshold("Default");
➤ //run("Set Measurements...", "area centroid fit shape
redirect=None decimal=1");
➤ //do{

```



```

➤ //run("Analyze Particles...", "size=100000-250000
  circularity=0.8-1.00 show=Nothing display clear slice");
➤ //NB min size assumes measurement in microns
➤ //holesFound = getString("All holes found?: y for Yes,
  other for No", "y");
➤ //if (holesFound != "y")
➤ //  waitForUser("Please adjust threshold");
➤ //} while (holesFound != "y");
➤ //resetThreshold();

➤ //waitForUser("Select calc positions slice");
➤ //calcslice=getSliceNumber();
➤ //calcifications
➤ setThreshold(180, 255); //180 is arbitrary
➤ run("Threshold...");
➤ waitForUser("If necessary, adjust threshold");

➤ run("Analyze Particles...", "size=100-1E6
  circularity=0.00-1.00 show=[Overlay Outlines] display
  slice");
➤ particlesTitle=getTitle;

➤ //Create results file name
➤ sliceTitle=replace(inputTitle,"Preprocessed ","");
➤ sliceTitle=replace(sliceTitle,".tif","-Slice "+slice);
➤ sliceFile=inputPath+sliceTitle;

➤ //Save results file
➤ saveAs("Results","C:\\Temp\\Tempresults.txt");
➤ File.rename("C:\\Temp\\Tempresults.txt", sliceFile +
  ".txt")

```

```
➤ //Save slice image
➤ selectWindow(particlesTitle);
➤ saveAs("Tiff",sliceFile+".tif");
➤ resetThreshold();
➤ run("Flatten"); //makes overlay permanent
➤ saveAs("Tiff",sliceFile+" markers.tif");
➤ selectWindow("Results");
➤ run("Close");
➤ selectWindow("Log");
➤ run("Close");
➤ selectWindow("Threshold");
➤ run("Close");
➤ close();
➤ close();
➤ close();
➤ //End of program
```

## Appendix F Publications

Scott, R., Kendall, C., Stone, N. & Rogers, K.

Locating microcalcifications in breast histopathology sections using micro CT and XRF mapping.

Anal. Methods 6, 3962 (2014).

Scott, R., Stone, N., Kendall, C., Geraki, K. & Rogers, K.

Relationships between pathology and crystal structure in breast calcifications: an in situ X-ray diffraction study in histological sections.

npj Breast Cancer 2, 16029 (2016).

Scott, R., Kendall, C., Stone, N. & Rogers, K.

Elemental vs. phase composition of breast calcifications.

Sci. Rep. 7, 136 (2017).